

SPECTROSCOPIC OBSERVATIONS OF MERCURY'S SODIUM EXOSPHERE

A thesis presented to

The Faculty of Natural & Applied Sciences - NDU

the Notre Dame University

In partial fulfillment

of the requirements for the degree

Master of Science in Astrophysics

Fatima A. Kahil

September 2014

*This work is dedicated to my inspiring parents.*

# Acknowledgments

First, I would like to express my gratitude to my advisor, Dr. Nelly Mouawad for her help and patience during the period of my thesis work. Her knowledge and motivation made this work possible.

I would like to thank Dr. Bassem Sabra and Dr. Roger Hajjar for their academic help and guidance throughout my graduate studies. I am grateful to the opportunity of being a part of the graduate program at NDU.

Many thanks to my professors at Notre Dame University and Saint Joseph University, Dr. Cyrine Nehme, Dr. Marwan Jebran, Dr. Jamal Bittar and Dr. Jihanne Moulakka.

I want to express my deep thanks to my lovely family, mom, dad, brothers and sister, thank you for the love and care you bless me with everyday, I am here today because of you.

# Abstract

## Spectroscopic Observations of Mercury's Sodium Exosphere

by Fatima Kahil, September 2014

The MErcury Surface, Space ENvironment, GEochemistry, and Ranging NASA's spacecraft, known as MESSENGER, flew by Mercury on September 29, 2009. It was the spacecraft's third and final flyby of the planet. The Ultraviolet and Visible Spectrometer (UVVS) onboard MESSENGER determines the composition and structure of Mercury's exosphere, the extremely low density atmosphere, and studies its neutral gas emission (especially that of Sodium Na and Calcium Ca) in the tail (anti-sunward) of the exosphere. My current project is to study the variability and asymmetries seen in the Sodium distribution, using very high spectral resolution ground-based data obtained at the McDonald 2.7 m telescope over 4 days before and after the MESSENGER's third flyby by Mercury (Sep 28 till Oct 2, 2009). I present my work on the data reduction and analysis of these ground-based observations, where I developed multiple scripts to do the photometric analysis in order to study the emission, morphology, and variability of the Na exosphere. In addition, I compare ground-based data with space data making this study unique in this field of research. I discuss how further modelling of the combined data-sets can enable us to answer questions on the formation and morphology of Mercury's exosphere, many of which are still unanswered.

**key words:** Solar system – Planets – Mercury – Exospheres – Spectroscopy.

# Résumé

## Les Observations Spectroscopiques de l'Exosphère de Sodium de Mercure

par Fatima Kahil, Septembre 2014

La sonde de la NASA, MErcury Surface, Space ENvironment, Geochemistry, and Ranging, connu sous le nom MESSENGER, a survolé Mercure le 29 Septembre 2009. Il s'agissait du troisième et dernier survol de la sonde de la planète Mercure. Le Ultraviolet and Visible Spectrometer (UVVS) à bord de MESSENGER détermine la composition et la structure de l'exosphère de Mercure, l'atmosphère d'extrêmement faible densité, et étudie ses émissions de gaz neutre (en particulier celui du sodium Na et calcium Ca) dans la queue (anti-vers le soleil) de l'exosphère. Mon projet est d'étudier la variabilité et les asymétries vues dans la distribution de l'exosphère de sodium, en utilisant des données de très haute résolution spectrale obtenues au McDonald par le télescope de 2.7 m, du 28 Sep au 2 Oct, 2009, en même temps que le troisième survol de Mercure par MESSENGER le 29 Sep, 2009. Je vais travailler sur la réduction des données et l'analyse de ces observations au sol , et le développement de certaines routines pour faire l'analyse spectrale et photométrique afin d'étudier l'émission, la morphologie et la variabilité de l'exosphère de Na. En outre, la comparaison des données au sol avec les données de l'espace rend cette étude unique dans ce domaine de recherche, ce qui nous permet de répondre à des questions sur la formation et la morphologie de l'exosphère de Mercure, dont beaucoup sont encore sans réponse.

**Mots-clefs:** Système solaire – Planètes – Mercure – Exosphère – Spectroscopie.

# Table of Contents

	Page
Acknowledgments . . . . .	iii
Abstract . . . . .	iv
Résumé . . . . .	v
List of Figures . . . . .	3
List of Tables . . . . .	7
1 Mercury Overview . . . . .	8
1.1 Orbital Characteristics . . . . .	8
1.2 Internal composition and Geology . . . . .	8
1.3 Magnetic Field and Mercury Sodium tail . . . . .	9
1.4 Exosphere . . . . .	11
1.5 Space Missions . . . . .	12
1.5.1 Mariner10 . . . . .	13
1.5.2 The MESSENGER Mission to Mercury . . . . .	14
1.5.3 Future mission: BepiColombo . . . . .	16
2 Mercury's Exosphere . . . . .	17
2.1 Discovery . . . . .	17
2.2 Source Processes . . . . .	19
2.3 Loss Processes . . . . .	22
2.4 Sodium Exosphere and Mercury observations . . . . .	23
2.4.1 Discovery . . . . .	23
2.4.2 The Physics of Sodium Emission Lines . . . . .	24
2.4.3 Dynamics and Spatial Distribution of Sodium . . . . .	26
3 Observations and Data Reduction . . . . .	33
3.1 Data and Facility . . . . .	33
3.2 Longslit Spectroscopy . . . . .	39
3.3 Data reduction . . . . .	41
3.3.1 Geometric Correction: Registration . . . . .	41
3.3.2 Cleaning up the Data . . . . .	45
3.4 Improving the Flatfielding . . . . .	52
3.5 Sodium line Extraction . . . . .	56
3.6 Flux Calibration . . . . .	58
3.6.1 Estimating the seeing . . . . .	59

3.6.2	Calibration in Rayleigh . . . . .	67
4	Scripting . . . . .	70
4.1	Motivation . . . . .	70
4.2	IRAF scripting . . . . .	71
4.2.1	The basic reductions . . . . .	72
4.2.2	Extraction of Sodium lines . . . . .	73
4.2.3	SCRIPTS . . . . .	78
5	Results and Analysis . . . . .	82
5.1	Sodium Emission Maps . . . . .	82
5.2	Asymmetries in Emission intensities . . . . .	85
5.3	Discussion . . . . .	89
5.4	From ground-based to space observations . . . . .	95
5.4.1	MESSENGER observations . . . . .	95
5.4.2	MESSENGER & ground-based observations . . . . .	98
6	Conclusions . . . . .	102
	Bibliography . . . . .	105
A	Array correction . . . . .	110
B	CL scripts . . . . .	117
B.1	reduction.cl . . . . .	117

# List of Figures

1.1	Mercurys space environment and surface features (Image ESA/Bepi-Colombo).	10
1.2	Anti-sunward tail of Mercury.	11
1.3	Mariner10.	13
1.4	MESSENGER.	14
1.5	Messenger's orbit at Mercury, MESSENGER website.	15
2.1	Sources, sinks and interactions with the magnetic field, (Domingue et al. 2007).	19
2.2	Surface-Exosphere interaction at Mercury, (Smyth & Marconi 1995).	20
2.3	Source and loss processes.	23
2.4	Sodium discovery spectrum.	24
2.5	Contributions to an observed planetary spectrum.	25
2.6	Energy level schematic for atomic sodium, Brown & Yung (1976).	26
2.7	True anomalous Angle and Solar line Doppler shift (Smyth & Marconi 1995).	27
2.8	Solar radiation acceleration ((Smyth & Marconi 1995))	28
2.9	Sodium tail modelling, (Smyth & Marconi 1995)	30
2.10	Doppler shifted emission lines.	31
2.11	The relevant parameters for the three flybys of MESSENGER (McClintock et.al 2009).	32
2.12	Na tail during M1, M2 and M3.	32
3.1	Observatory & telescope.	34
3.2	Slit positions on the planet.	34
3.3	Cross-dispersed Echelle Spectrograph	40
3.4	Data image with slit directions.	40

3.5	Before and after column registration.	44
3.6	Before and after line registration.	44
3.7	The spatial and spectral profiles before cosmic ray removal.	46
3.8	The spatial and spectral profiles after cosmic ray removal.	46
3.9	Trimming data images using <i>imcopy</i> .	47
3.10	Spectral features of the planetary spectrum.	49
3.11	The sky part of the slit.	50
3.12	Making the sky template.	51
3.13	Mercury+sky spectra.	52
3.14	After sky subtraction.	52
3.15	Averaged spectrum.	53
3.16	Spectrum 23 after correction.	54
3.17	Spectrum 24 after correction	54
3.18	Spectrum 25 after correction.	55
3.19	Spectrum 29 after correction.	55
3.20	Spectrum 30 after correction.	56
3.21	Spectrum 31 after correction.	56
3.22	The averaged spectrum along columns after sky subtraction.	57
3.23	Hapke reflectance model and convolved Hapke.	60
3.24	The guider image.	60
3.25	Cuts on the Hapke and guider images.	62
3.26	Equatorial cuts.	62
3.27	Northern cuts.	63
3.28	Southern cuts.	64
3.29	Slit and continuum profiles.	66
4.1	Sodium Line Extraction (weak solar reflection).	75
4.2	Sodium Line Extraction (strong solar reflection).	76

4.3	Cursor coordinates calculation.	78
4.4	Extracting the continuum.	81
5.1	Sodium emission map output of the code.	82
5.2	Sodium Emission Maps, September 29, 2009, the slit $30'' \times 1.2''$ was used.	83
5.3	Sodium Emission Maps, September 30, 2009 (North-South slit orientation), the slit $30'' \times 0.2''$ was used.	84
5.4	Sodium Emission Maps, September 30, 2009 (terminator-limb slit orientation), the slit $30'' \times 0.2''$ was used.	85
5.5	North-South Na profile, Sep 29 (slit on terminator).	86
5.6	North-South Na profile, Sep 29 (slit on terminator).	87
5.7	North-South Na profile, Sep 30 (slit on terminator).	87
5.8	North-South Na profile, Sep 30 (slit on terminator).	88
5.9	Terminator-Limb Na profile, Sep 30.	88
5.10	Na emission profiles,Potter et al. (2006).	90
5.11	North-to-South ratios(Potter et al. 2006).	92
5.12	Terminator-to-Limb ratios (Potter et al. 2006).	92
5.13	North-South & Terminator-Limb ratios for our ground-based data.	94
5.14	Sodium tail emission during M1 and M2.	96
5.15	Altitude profiles of Na emission by MESSENGER.	97
5.16	Ground-based data altitude profiles.	98
5.17	MESSENGER and ground-based data altitude profiles.	99
5.18	MESSENGER and ground-based data altitude profiles.	99
5.19	The geometry of MESSENGER's observations.	100
A.1	Spatial profiles of images 23 and 24.	110
A.2	Spatial profiles of images 25 and 29.	110
A.3	Spatial profiles of images 30 and 31.	111
A.4	The gradient in the sky spectrum.	112

A.5 The spatial profile of the normalized Flatfield. . . . .	113
A.6 The corrected mercury image . . . . .	114
A.7 Image 23 spatial profile before and after correction . . . . .	115
A.8 Image 24 spatial profile before and after correction . . . . .	115
A.9 Image 25 spatial profile before and after correction . . . . .	115
A.10 Image 29 spatial profile before and after correction . . . . .	116
A.11 Image 30 spatial profile before and after correction . . . . .	116
A.12 Image 31 spatial profile before and after correction . . . . .	116

# List of Tables

3.1	Data of September 28, 2009 . . . . .	36
3.2	Data of September 29, 2009 . . . . .	37
3.3	Data of September 30, 2009 . . . . .	38
3.4	The input file for column registration, input1. . . . .	42
3.5	The input file for line registration, input2 . . . . .	43
3.6	Estimation of the seeing parameters of September 29 data. . . . .	66
3.7	Estimation of the seeing parameters for September 30 data. . . . .	67
3.8	Calibration factors for the data of September 29, 2009. . . . .	69
3.9	Calibration factors for the data of September 30, 2009. . . . .	69
4.1	The sodium line extraction cursor file . . . . .	77
5.1	N/S and T/L ratios for data of September 29 & 30 2009. . . . .	94

# CHAPTER 1

## Mercury Overview

### 1.1 Orbital Characteristics

Mercury is the smallest terrestrial planet in the solar system, and the closest orbiting planet to our Sun showing the highest orbital eccentricity of 0.21, bringing Mercury to  $0.307 \text{ AU}$  ( $70 \times 10^6 \text{ km}$ ) from the Sun at perihelion and to  $0.467 \text{ AU}$  ( $46 \times 10^6 \text{ km}$ ) at aphelion. As a result, the solar flux received by the planet and therefore its surface temperature will be variable throughout one Mercurian year (100 K to 700 K), for instance the subsolar point reaches about 700 K during perihelion, but only 550 K at aphelion (Lewis et.al 2004).

Due to its proximity to the Sun and its elliptical orbit, Mercury can only be seen from Earth in the morning when the Sun has not yet risen or in the evening shortly after sunset. Mercury has a very slow rotation period, it spins on its axis every 59 Earth days and rotates around the Sun every 88 Earth days, which means that Mercury spins on its axis only 3 times during the course of 2 Mercurian years, creating a 3:2 spin-orbit resonance. As seen from the Sun, it appears to rotate only once every two Mercurian years, so an observer on Mercury would see only one day every two years. From Earth, it displays a complete range of phases along its orbit, like Venus and the Moon.

### 1.2 Internal composition and Geology

Mercury is the smallest planet in our solar system ( $3.30 \times 10^{23} \text{ kg}$ ) yet the second highest in density ( $5.43 \text{ g cm}^{-3}$ ) slightly less than Earth's ( $5.51 \text{ g cm}^{-3}$ ). It has a

radius of 2440 *km* much smaller than Earth's 6378 *km*. It consists of mostly metallic (70%) and silicate (30%) materials. Internal structure models indicate that Mercury has a solid silicate crust and mantle surrounding an iron-rich liquid middle core and a solid inner core, the total core radius is approximately 75% of the planetary radius and the fractional core mass is at least 60%, which is twice that for Earth. Mercury is a rocky planet like Earth, its surface is heavily cratered indicating that it has been geologically inactive for billions of years, and similar in appearance to the Moon by its size, the lack of satellites and the absence of a substantial atmosphere.

### 1.3 Magnetic Field and Mercury Sodium tail

Mercury has a magnetic field that resembles that of the Earth's in its magnetic dipole structure. The first discovery of Mercury's intrinsic magnetic field was made by Mariner 10 during its first flyby in 1974 (Ness et al. 1974), the spacecraft measured the field's strength as 1.1% that of the Earth's magnetic field (400 nT at the equator), it's strong enough to deflect solar wind particles, the interaction of Mercury's magnetic field with the solar wind produce the so called **magnetosphere** of Mercury, which is a dynamic structure. The **magnetopause** which is the boundary between the magnetosphere and the surrounding plasma extends to  $1.4 R_M$ . Figure 1.1 shows the components of Mercury's magnetosphere and its geological features:

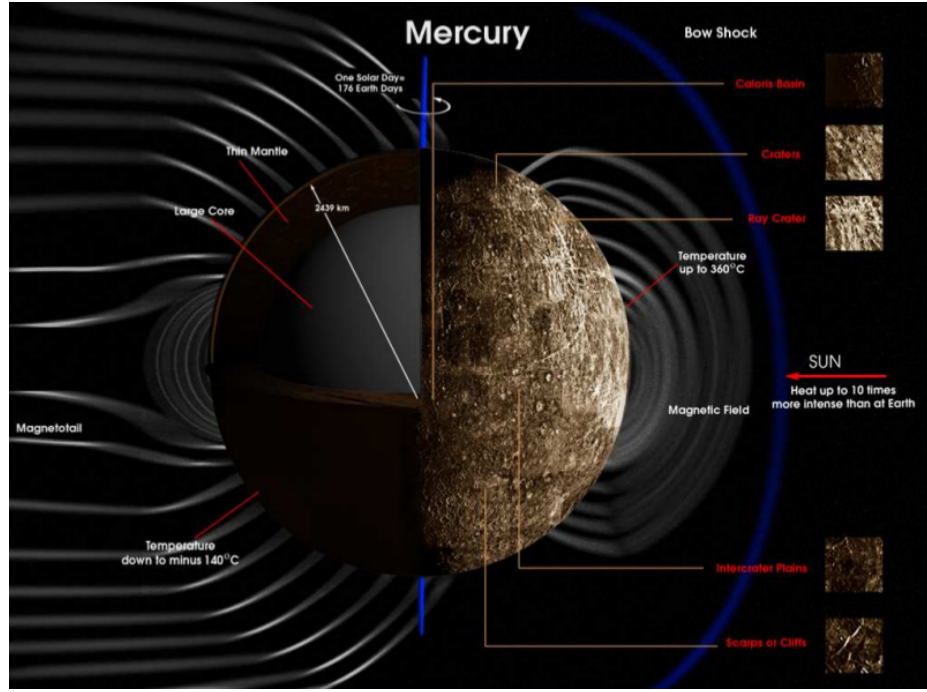


Figure 1.1: Mercurys space environment and surface features (Image ESA/BepiColombo).

In addition to having a magnetic field, Mercury has an anti-sunward sodium tail. Potter et al. (2002) detected for the first time Mercury's sodium tail that extended to 16 Mercury radii. Everytime a sodium atom scatters a solar photon, it recoils in the anti-sunward direction moving away from the Sun, and hence experiences increasing solar flux and therefore an ever increasing acceleration, creating a comet-like tail behind the planet (fig. 1.2). The shape and intensity of sodium in this tail depends on the position of the planet with respect to the Sun, since the solar radiation pressure is the main factor affecting its shape (more details about solar radiation pressure in section 2.4.3). Smyth & Marconi (1995) modelled the effect of solar radiation pressure on trajectories of sodium atoms emitted from the surface at various velocities, and they concluded that for minimum solar radiation pressure, the shape of sodium exosphere is normal symmetric spherical atmosphere, however for maximum values of solar radiation pressure, atoms leaving the surface with velocities

less than the escape velocity of the planet ( $4.25 \text{ km s}^{-1}$ ) can escape the latter to form a long comet-like neutral sodium tail.

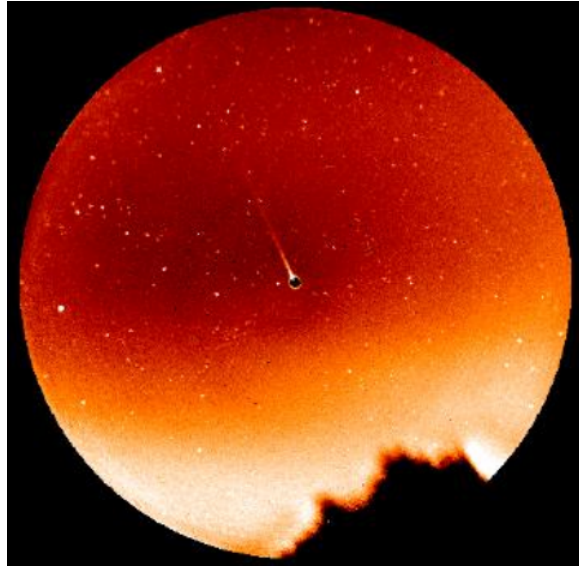


Figure 1.2: The anti-sunward sodium tail of Mercury as viewed from Earth in 2007. The image is taken from (Baumgardner 2008), where they imaged Mercury's sodium tail by coronagraphy.

## 1.4 Exosphere

Mercury has a small mass and therefore not enough gravity ( $0.38 g$ ) to have a thick atmosphere but it does have a *surface-bounded exosphere*. The term *exosphere* relates to a thin gaseous medium where the mean distance before an atmospheric particle hits another one is comparable to or larger than the atmospheric thickness, which means that its density is so low that atoms and molecules rarely collide, and since its exobase coincides with the surface, its composition and behaviour are controlled by interactions with the magnetosphere and the surface (Killen 2007). The exosphere of Mercury is mainly composed of:

- Light species such as Hydrogen (H and H<sub>2</sub>).

- Noble gases such as Helium (He).
- Alkali species such as Sodium (Na), Potassium (K), Calcium (Ca) and Magnesium (Mg).
- Heavy species like Oxygen (O).
- Possibly other ionic species such as ionized water vapor ( $\text{H}_2\text{O}^+$ ), ionized Hydrogen sulfide ( $\text{H}_2\text{S}^+$ ) (McClintock et.al 2009).

These species have different sources, they originate either from the solar wind or from the surface of the planet. Hydrogen, Helium and Oxygen were discovered by the Ultraviolet photometer of Mariner 10 spacecraft in 1974. Hydrogen and Helium come from the solar wind, but they are released in the exosphere from the surface by **Thermal Desorption** (LeBlanc et al. 2007). Magnesium was observed by the Ultraviolet and Visible Spectrometer (UVVS) channel of the Mercury Atmospheric and Surface Composition Spectrometer (MASCS) on board the MESSENGER spacecraft in 2009. Sodium, Potassium and Calcium discovered by ground-based observations are ejected from the surface through different source processes (Mouawad et al. 2011) as explained in the next chapter.

## 1.5 Space Missions

Sending space missions to explore the planet Mercury is different with planets beyond Earth's orbit due to the following reasons:

- The great gravitational pull of the Sun makes it difficult to obtain a satellite orbit around the planet, so it will require great amounts of energy to reach and observe the planet. In addition, it is difficult for probes to land on the surface of the planet due to the lack of the atmosphere that help in the process of aerobraking or using a parachute type design (like the probe Curiosity that landed on Mars).

- The proximity of the planet to the Sun and the harm that could affect the instruments on the spacecraft due to the solar radiation and heat, the spacecraft has to be equipped with a sunshield or other technology to protect the instruments.

So far, only two space missions have succeeded in reaching Mercury and making observations: Mariner 10 and MESSENGER.

### 1.5.1 Mariner10

Mariner 10 was a NASA probe aiming to observe the atmosphere, surface and physical characteristics of Mercury. It was accelerated with the gravity field of Venus to reach its destination, passing close Mercury on March, 1974 as it flew around the Sun. It encountered Mercury two times on September, 1974 and March 1975. And since the same side of Mercury was illuminated during these encounters, Mariner 10 was able to photograph parts of the surface of Mercury (45%). The main discoveries of Mariner 10 were the detection of Mercury's magnetic field (Ness et al. 1974), and collection of 2800 photos revealing the nature of the surface with a Moon-like appearance, and finally the discovery of the tenuous surface-bounded exosphere.



Figure 1.3: Mariner10.

### 1.5.2 The MESSENGER Mission to Mercury

The MESSENGER mission was launched around 30 years after the Mariner 10 mission by the National Aeronautics and Space Administration (NASA) from Cape Canaveral on August 3, 2004. The MESSENGER spacecraft relied on the gravitational pull of the Earth, Venus and Mercury to enter in orbit around Mercury. It relied on one flyby of Earth in February 2005, two flybys of Venus in October 2006 and June 2007, and finally three flybys of Mercury, one in January 2008, one in October 2008 and one in September 2009 before entering in orbit in March 2011.

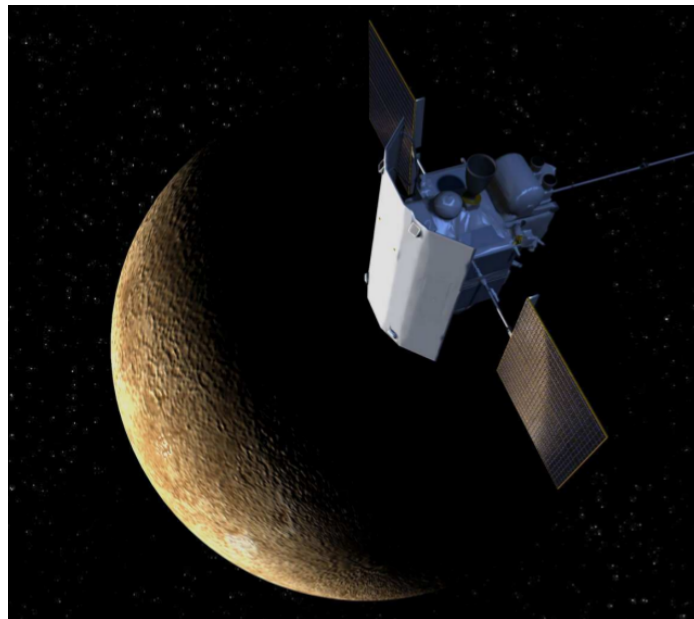


Figure 1.4: MESSENGER.

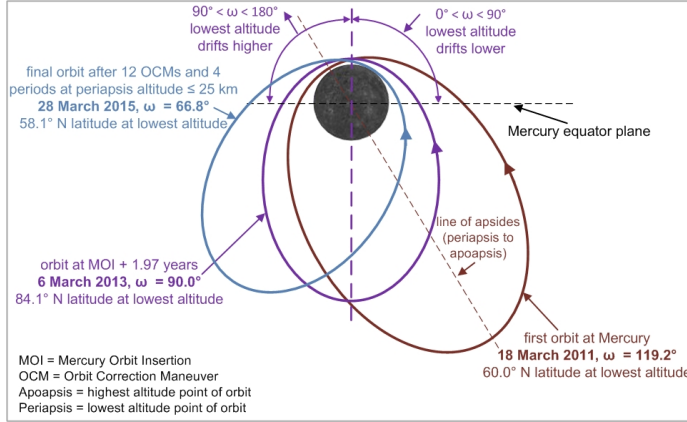


Figure 1.5: MESSENGER's orbit at Mercury, MESSENGER website.

During these flybys, MESSENGER was able to collect significant data, taking around 100000 images and achieving 100% mapping of Mercury on March 6, 2013. The scientific instruments onboard MESSENGER aim to answer puzzling questions related to Mercury's high density, crustal composition and structure, volcanic history, core structure, magnetic field generation, polar deposits, atmosphere and magnetosphere. The six key questions that these space instruments are addressing (Solomon 2001), are:

- What planetary formational processes led to the high metal/silicate ratio in Mercury?
- What is the geological history of Mercury?
- What are the nature and origin of Mercury's magnetic field?
- What are the structure and state of Mercury's core?
- What are the radar-reflective materials at Mercury's poles?
- What are the important volatile species and their sources and sinks on and near Mercury?

### 1.5.3 Future mission: BepiColombo

BepiColombo is Europe's first mission to Mercury, it is a joint mission between ESA and the Japan Aerospace Exploration Agency (JAXA), executed under the European Space Agency ESA leadership.<sup>1</sup> The mission will include two satellites, the Mercury Magnetospheric Orbiter (MMO) developed by JAXA and the Mercury Planetary Orbiter (MPO) developed by ESA. Like Mariner 10 and MESSENGER, BepiColombo will use gravity slingshots from Venus and Earth, it will also use solar electric propulsion to slow the orbiters as they get closer to the Sun to minimize the influence of the Sun's gravity (Munsell 2006).

---

<sup>1</sup><http://sci.esa.int/bepicolombo/>

# CHAPTER 2

## Mercury's Exosphere

The atmosphere is the gaseous outer portion of a planet. Atmospheres are discovered around all planets in the solar system and around several satellites, each one having a unique profile. Some atmospheres are dense, and gradually blend into fluid envelopes that constitute the whole planet (gaseous giants) or lie at direct contact with the surface (Venus), others are extremely tenuous having density billions of times smaller than the one at Earth, there are called *exospheres*. The composition of a planetary atmosphere varies from solar-like H/He atmospheres for the giant planets to atmospheres dominated by nitrogen, carbon dioxide or sulfur dioxide for terrestrial planets. Being unique for each planet, all atmospheres are governed by the same processes: clouds in the atmospheres, winds due to gradients in temperature and pressure, photochemistry and solar radiation affect the upper layer of the atmosphere (Imke & Lissauer 2001).

### 2.1 Discovery

The first discovery of an exosphere around Mercury was made through the ultraviolet airglow and occultation experiments on Mariner 10 during its flybys of the planet in 1974 and 1975. These experiments set an upper limit of the atmospheric

pressure of about  $10^{-12}$  bar. This low pressure defines the atmosphere of Mercury as a *surface-bounded exosphere* with its exobase coincident with Mercury's surface. As mentioned in section 1.4, Hydrogen(H), Helium(He) and Oxygen(O) were discovered by the ultraviolet spectrometer onboard Mariner 10 (Broadfoot et al. 1974, 1976). Since Mariner 10 discovery for Mercury's exosphere, ground-based observations were carried to further investigate the components of this exosphere; as a result, three additional elements, sodium (Na) (Potter & Morgan 1985), potassium (K)(Potter & Morgan 1986) and calcium (Ca) (Bida et al. 2000) were discovered through their resonance scattering emission lines, and magnesium (Mg) was discovered by the MESSENGER spacecraft during its second flyby in 2009 (McClintock et.al 2009).

As mentioned earlier, Mercury has a tenuous collisionless exosphere with the exobase coincident with the surface, and therefore Mercury has several distinct exospheres, each corresponding to its constituents and whose behaviour depends on the interactions with the magnetosphere and the surface. And since this exosphere is very dynamic (variable in time and space), so there must be variable processes responsible for the distribution of these elements. Mercury's exosphere is a result of a complex interplay between planetary surface material, solar wind ions, cosmic rays, solar energetic particles, solar radiation and interplanetary dust particles that have impacted Mercury's surface over time, so Mercury is the only rocky planet in the solar system where the distribution of atoms is controlled by the surface/exosphere/-magnetosphere/solar wind interactions as will be described later.

The life cycle of the exospheric material is shown in Figure 2.1 and can be described as follows: Atoms are delivered to the surface by **Delivery processes**, to be released from the surface of Mercury through different emission processes, **Sources**, and are lost from the exosphere by different loss processes, **Sinks**.

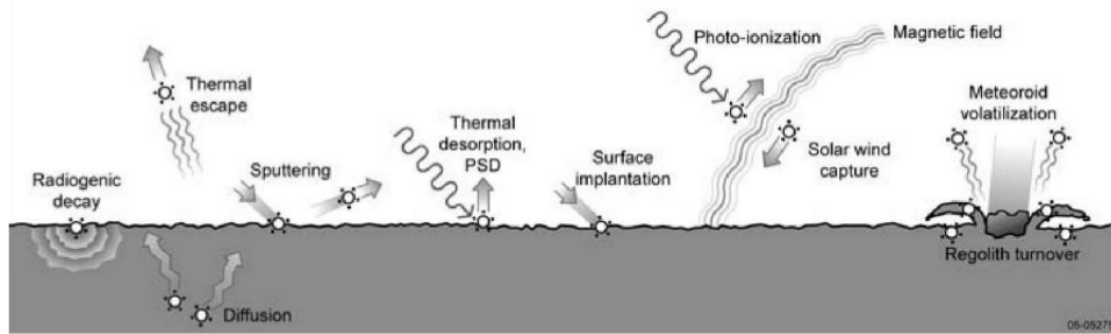


Figure 2.1: Sources, sinks and interactions with the magnetic field, (Domingue et al. 2007).

## 2.2 Source Processes

Atoms that are liberated from the surface by various source mechanisms are called **source atoms** and may be thermal or nonthermal in nature. Source atoms that encounter the surface and have one or more ballistic hops are called **ambient atoms** and form the bound component of the exosphere. The main forces acting on these atoms are the gravity of Mercury and the solar radiation pressure— the push by solar photons in the anti-sunward direction—, these along the different loss processes available at Mercury control the trajectories of the atoms and their interactions with the surface, and therefore the exosphere as shown in Figure 2.2.

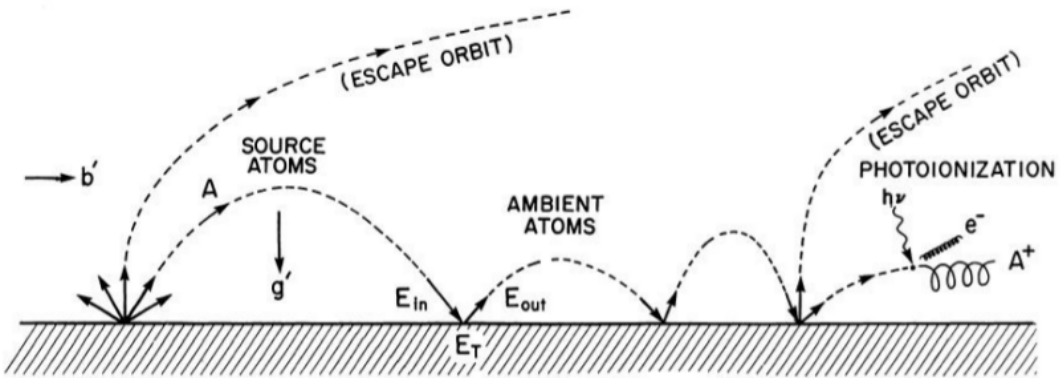


Figure 2.2: Surface-Exosphere interaction at Mercury: the source atoms liberated from the surface, the ambient atoms and their ballistic hops, the effective local gravity ( $g'$ ), the solar radiation acceleration ( $b'$ ), and photoionisation as a loss process, image taken from (Smyth & Marconi 1995).

### Thermal Desorption

Thermal desorption or thermal 'evaporation' is a low-energy process that results from solar photons hitting Mercury's surface. These photons (whose thermal energy exceeds the binding energy) heat the surface and the heat releases the atoms. The energy distribution for the TD ejecta is a Maxwellian (LeBlanc & Johnson 2003):

$$f(E, \theta) = 2 \cos \theta \frac{E}{(k_B T_S)^2} \exp\left(-\frac{E}{k_B T_S}\right) \quad (2.1)$$

Where  $E$  is the energy of the ejecta,  $\theta$  is the angle between the velocity vector ejecta and the normal to the surface and  $T_S$  is the surface temperature. Thermal desorption produces atoms at 0.03 to 0.05 eV (Yakshinskiy & Madey 2000), and since the escape energy at Mercury's surface is 2.07 eV, desorbed atoms remain close to the surface without significant contribution to planetary loss. The rate of ejection of sodium atoms depends on the concentration of sodium atoms on the surface, the binding energy and the surface temperature. This process is only effective on the dayside of the planet, mostly near the subsolar point.

## Photon-Stimulated Desorption

Photon-Stimulated Desorption (PSD) is also a low-energy process and results from solar photons with energies  $< 4\text{eV}$  hitting the surface and inducing bond-breaking of atoms to be desorbed as a result of electronic excitation. This process does not act by thermal processes or moment transfer, it acts through electronic transitions. The flux of desorbed atoms depends strongly on the photon flux at Mercury's orbit which depends on the square of Mercury heliocentric distance, it also depends on surface temperature and the availability of sodium atoms at the upper layer of the surface. As a result, the largest PSD fluxes of Na ejecta occur near equatorial latitude at perihelion, since at these regions the solar flux will be at maximum. Like thermal desorption, this process is only active on the dayside of the planet.

## Solar Wind Sputtering

Since the Magnetosphere of the planet is at certain time intervals and under certain circumstances (when the solar wind activity is high, or when the Interplanetary Magnetic Field IMF has a southern or northern directions) open to the solar wind over significant areas, the solar wind ions can penetrate the surface through the cusp regions carried by the open magnetic field lines, releasing neutral sodium via momentum transfer and reproducing local concentration of released atoms. Ion sputtering causes a major variations in Mercury's exosphere, since the solar wind activity is highly variable temporally and spatially, and it has been suggested to be the cause of short-term enhancements to Mercury's exosphere, particularly at high latitude regions (Potter & Morgan 1990; Mouawad et al. 2011). The flux of released particles depend on the solar wind flux and velocity, and on the binding energy of ejected elements in the regolith minerals, thus it depends on composition of the surface (Lammer et al. 2003). The solar wind is mostly protons  $H^+$  and alpha particles  $He^{2+}$  with mean

energies in the 1-2 keV range, and the neutral atoms released by this process have energy in the 0.001-1 eV range or  $0.3\text{-}3 \text{ km s}^{-1}$  for sodium atoms (Cassidy et al. 2005).

### Micrometeoroid Impact Vaporization

Micrometeorite impacts may generate low-volatile species to the exosphere. It may be the only source process acting over the whole planetary surface when no energetic ions from the magnetosphere or the solar wind hit the surface.

## 2.3 Loss Processes

Once the atoms are liberated from the surface to form the surface-bounded exosphere, their trajectories are controlled by two main forces: the gravitational pull of the surface, and radiation pressure. The acceleration due to radiation pressure results from the resonant scattering of sunlight: the change in photon momentum between the incident sunlight and the emitted scattered light. Radiation acceleration affects different atoms to different degrees (sodium strongly, calcium weakly, magnesium insignificantly), so some atoms will return to the surface, other atoms will escape far from the planet forming the comet-like tale (**Thermal Escape**). Solar photons can also ionize neutral atoms by **Photoionization**, these photoions can be captured by the magnetic field lines of Mercury and returned to the surface to be neutralized, or picked up by the solar wind and whisked away from the planet.

## Processes at Work in Mercury's Exosphere

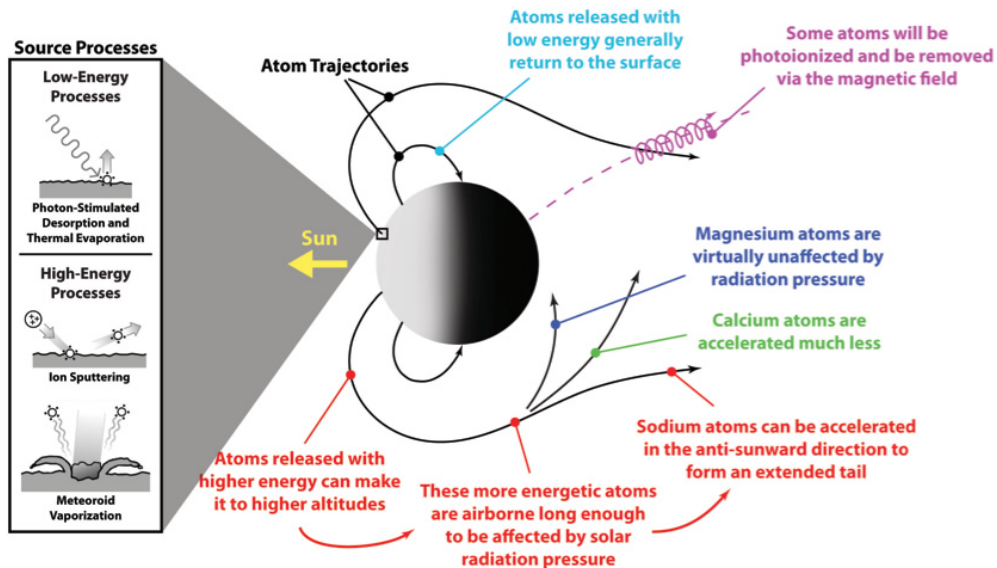


Figure 2.3: Schematic illustration of the processes that generate and maintain Mercury's exosphere, and the loss processes responsible for the depletion of elements from the exosphere, MESSENGER website.

## 2.4 Sodium Exosphere and Mercury observations

### 2.4.1 Discovery

The fourth species after the space discovery of H, He and O, was discovered by (Potter & Morgan 1985), after they were able to observe its Fraunhofer emission lines at 589.0 and 589.6 nm that are attributed to resonant scattering of sunlight from sodium vapor in the exosphere of the planet.

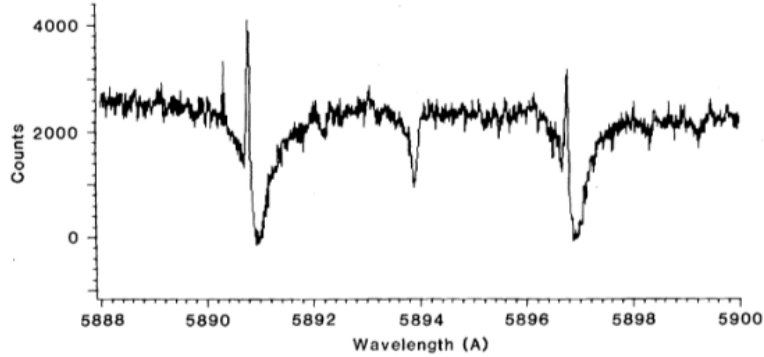


Figure 2.4: Sodium discovery spectrum showing D1 and D2 sodium emission lines within the solar Fraunhofer absorption lines reflected from Mercury's surface (Potter & Morgan 1985).

### 2.4.2 The Physics of Sodium Emission Lines

Planets, moons, asteroids and comets are visible because sunlight is reflected off their surface, cloud layers or atmospheric gases. Sunlight itself displays a large number of absorption lines, the *Fraunhofer absorption spectrum*, since atoms in the outer layers of the Sun's atmosphere (photosphere) absorb part of the sunlight coming from the deeper, warmer layers.

Atoms and molecules in a planet's atmosphere or surface may absorb some of the Sun's light and re-emits it at the same wavelength. This is called *solar resonance scattering* which excites the sodium atoms in the exosphere producing emission lines. The lines are Doppler shifted with respect to the sodium solar Fraunhofer lines due to the radial velocity of Mercury with respect to the Sun. The atmosphere of the Earth also introduces additional absorption lines: water lines and other telluric lines. Figure 2.5 helps visualize the various contributions to an observed planetary spectrum: Sunlight with its absorption spectrum ( $S$ ) is reflected off a planet, where the planet's

atmosphere may produce additional absorption/emission lines, ( $P$ ), and additional absorption due to the Earth's atmosphere, indicated by lines ( $E$ ).

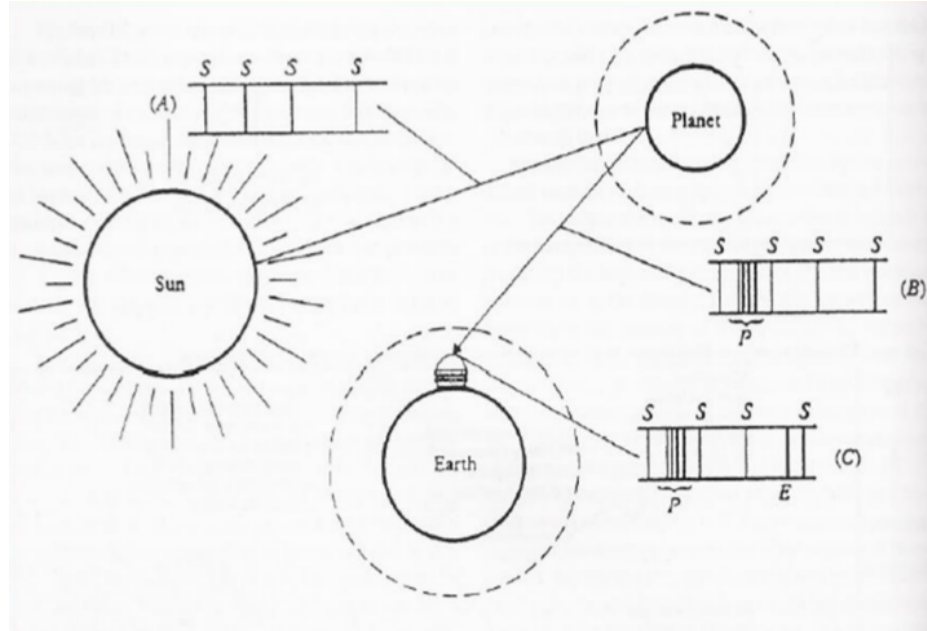


Figure 2.5: Contributions to an observed planetary spectrum. [Figure taken from Planetary Sciences, de Pater & Lissauer, 2001].

Even though Sodium is a trace species in the Solar system compared to Hydrogen or Helium, we are still able to detect it because of its strong emission lines in the visible part of the spectrum at  $5889.95\text{ \AA}$  (the D2-line) and  $5895.92\text{ \AA}$  (D1-line). Sodium has 11 electrons, with one valence electron in the  $3s$  shell. The  $1s$ ,  $2s$  and  $2p$  shells are filled. The Exospheric observations consist of detecting solar radiation that has been resonantly scattered from exospheric species. For sodium this consists of incident solar radiation exciting sodium atoms from the ground state  $3s^2S_{1/2}$ , to the first excited state which is split by spin-orbit coupling into 2 fine structure components,  $3p^2P_{1/2}$  and  $3p^2P_{3/2}$ , which are further split into 4 and 6 hyper-fine components, respectively, by coupling between the nuclear spin and total electronic angular momentum, see figure 2.6 taken from Brown & Yung (1976).

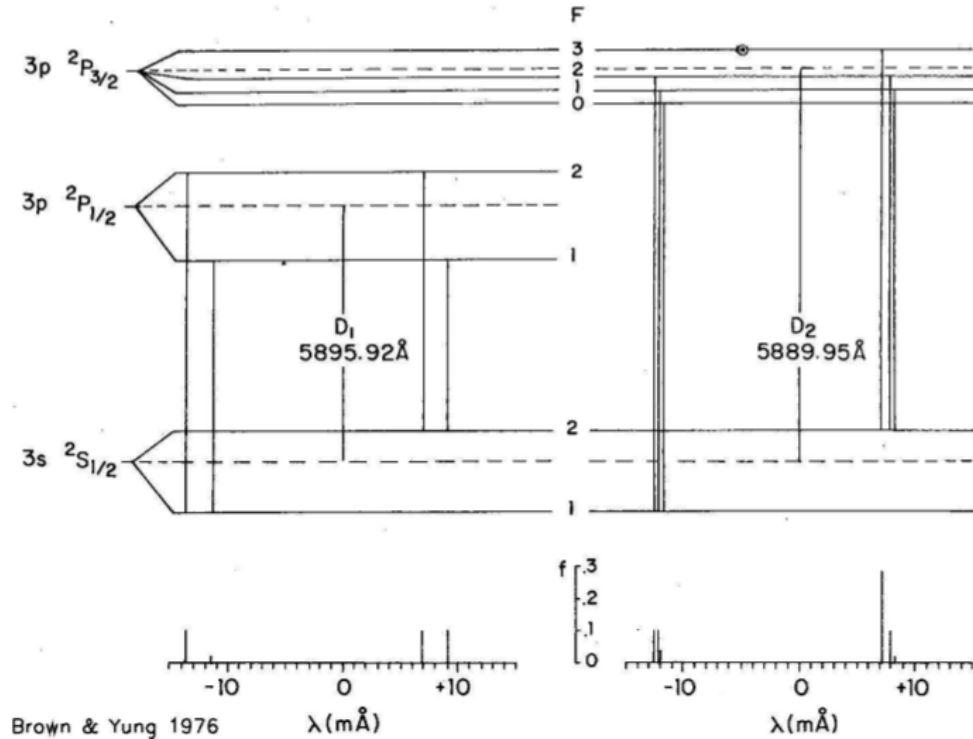


Figure 2.6: Energy level schematic for atomic sodium, Brown & Yung (1976).

### 2.4.3 Dynamics and Spatial Distribution of Sodium

#### Transport Dynamics of Sodium

The dynamics of sodium atoms in the exosphere of Mercury are controlled by the acceleration of gravity and solar radiation pressure produced by the resonant scattering of sodium atoms in their  $D_1$  and  $D_2$  emission lines. The latter affects the trajectory of sodium atoms to a large degree; it can cause the escape of atoms from the planet or carry them to the night side. The solar radiation acceleration is also variable because of the following reasons:

- As Mercury moves from perihelion (true anomaly angle TAA=0°) to aphelion (TAA=180°), the heliocentric distance (Sun-Mercury distance) changes by a

factor of 1.52, see Figure 2.7. The solar flux and thus the solar radiation pressure vary by the square of this distance.

- The Mercury-Sun radial velocity also varies from  $0 \text{ km s}^{-1}$  ( $\text{TAA}=0^\circ$ ) to  $10 \text{ km s}^{-1}$  ( $\text{TAA}=90^\circ$ ) to  $0 \text{ km s}^{-1}$  ( $\text{TAA}=180^\circ$ ). This change in radial velocity affects the solar spectrum 'seen' by the atoms on the planet, which shifts between  $\pm 200 \text{ m}\text{\AA}$  from the center of the sodium Fraunhofer line (Figure 2.7). At the bottom of the Fraunhofer line, the seen solar flux is an order of magnitude smaller than at maximum radial velocity.

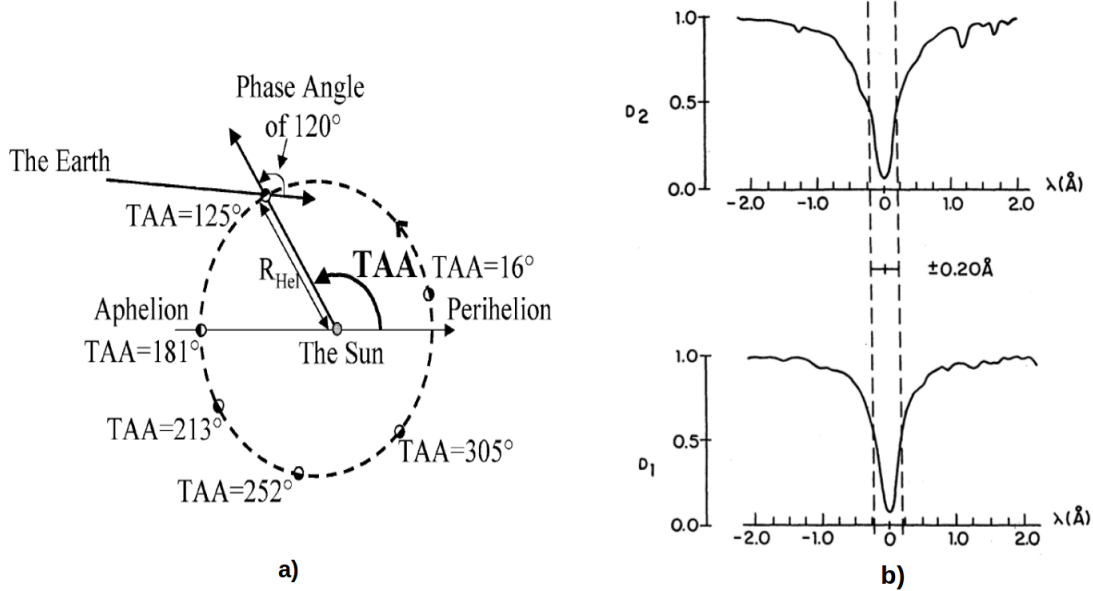


Figure 2.7: a) Mercury position around the Sun at different True Anomaly Angles (Smyth & Marconi 1995a), b)The solar Fraunhofer absorption line for D<sub>2</sub> and D<sub>1</sub> sodium emission lines, the zero is the rest wavelength of the line corresponding to zero radial velocity, the dashed vertical lines indicate the maximum shifts from the rest wavelength achieved by radial velocities of  $\pm 10 \text{ km/s}$  of Mercury with respect to the Sun occurring at  $\text{TAA} = \pm 90^\circ$  (Smyth & Marconi 1995).

Both combined effects will lead to more than one order of magnitude change of solar intensity seen by a sodium atom, and therefore the solar radiation acceleration

experienced by sodium atoms. As a result, the radiation acceleration varies from a maximum value of  $200 \text{ cm s}^{-2}$  (54% of surface gravity) at TAA near  $64^\circ$  and  $300^\circ$ , to a minimum value of  $12.5 \text{ cm s}^{-2}$  (3.4% of surface gravity) at TAA=180° (Figure 2.8).

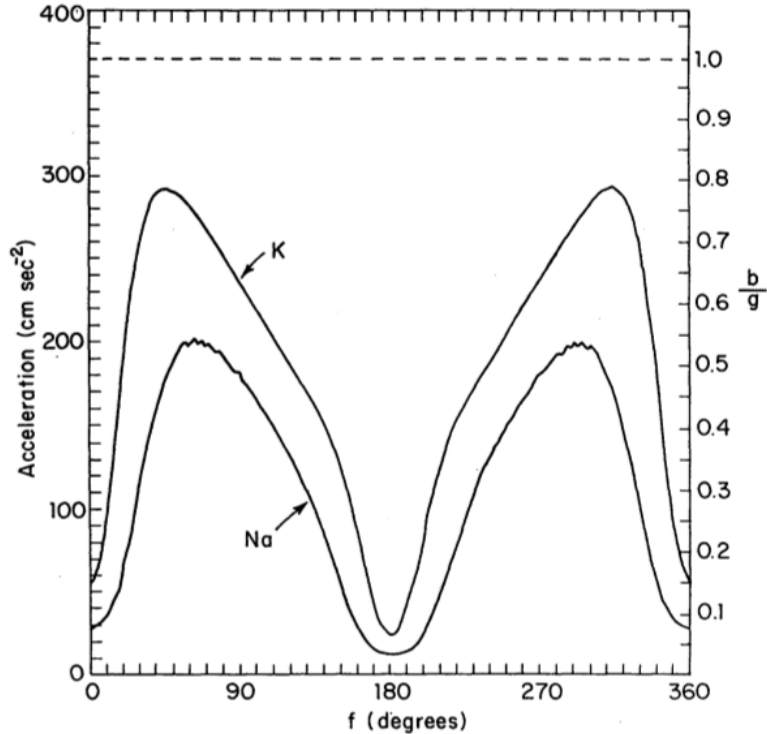


Figure 2.8: Solar radiation acceleration experienced by Sodium and Potassium atoms in their resonant emission lines, shown in absolute and surface gravity units as a function of true anomalous angle ( $f$ ) for the planet, (Smyth & Marconi 1995).

### Spatial Distribution of Sodium

Sodium is not uniformly distributed in the planet like the case of a classical atmosphere, this distribution is highly variable temporally and spatially as a natural result of the different mechanisms by which the source and loss processes act on the planet. These variations are seen to depend on local time, space weathering, solar wind activity and heliocentric distance.

The Mercury sodium tail is an example for such uneven distribution; it is affected by variations in the solar radiation pressure. Smyth & Marconi (1995) modelled the effect of solar radiation pressure on trajectories of sodium atoms emitted from the surface at various velocities (fig.2.9) and showed that the spatial configuration of the tail and density of sodium exosphere and tail changes with the position of Mercury along its orbit as a consequence of the change in solar radiation pressure. The tail configuration is expected to differ between the "out leg" of the orbit ( $TAA < 180^\circ$ ) and "in leg" of the orbit ( $TAA > 180^\circ$ ). When the planet is at  $TAA < 180^\circ$  (moving away from the Sun), the atoms in the exosphere see the solar line shifted redwards due to the anti-sunward velocity of the planet, and therefore it scatters sunlight from the blue side of the Fraunhofer line (Figure 2.10, left panel), as a result of the scattering, the sodium atom will recoil in the anti-sunward direction, the velocity of the atom increases and the intensity of sunlight it sees increases, so does the intensity of scattered sunlight.

On the other hand, when the planet is at  $TAA > 180^\circ$  (moving towards the Sun), the solar lines seen by sodium atoms are shifted bluewards, and sodium atoms scatter light from the red side of the Fraunhofer line (Figure 2.10, right panel) and when radiation acceleration pushes atoms with an anti-sunward velocity, the spectrum seen by the atom will shift redward and the intensity of scattered sunlight decreases.

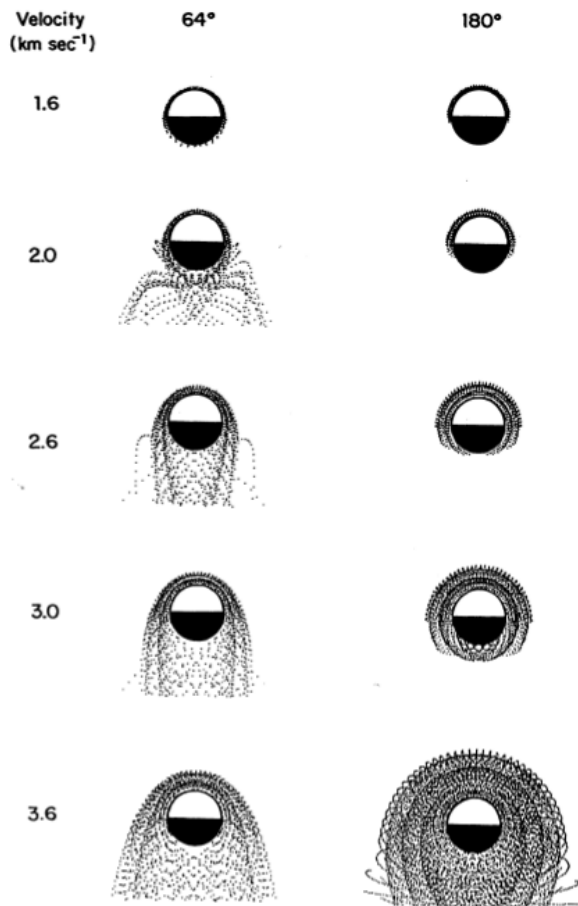


Figure 2.9: Modelling of the sodium tail configuration at minimum (TAA = 180°) and maximum (TAA = 64°) solar radiation acceleration for different ejection speeds. For the maximum value of solar radiation acceleration, sodium atoms begin to escape at speeds  $2 \text{ km s}^{-1}$ , while at minimum value sodium escapes for speeds in excess of  $3 \text{ km s}^{-1}$  which is closer to the escape velocity of  $4.25 \text{ km s}^{-1}$ , (Smyth & Marconi 1995).

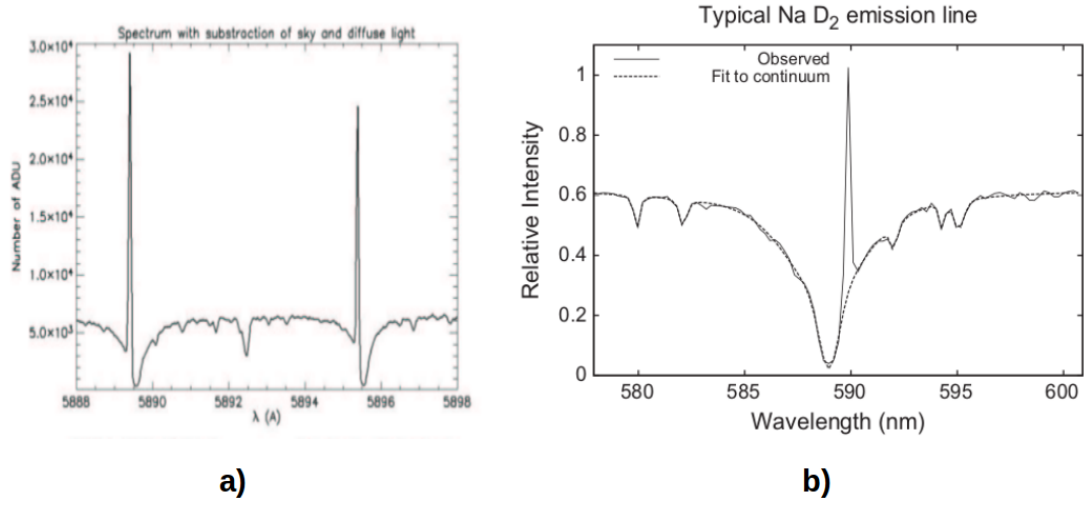


Figure 2.10: a) Spectrum showing the two Fraunhofer absorption lines and their corresponding Na emission lines, the latter is shifted bluewards because the planet was moving away from the Sun,Mongano et al. (2007), b) The D2 sodium line doppler shifted (to the red) from the core of the solar Fraunhofer line because the planet was moving toward the Sun,Mouawad et al. (2011).

These models developed to simulate the shape and distribution of Mercury's Na tail were further proved by the observations of MESSENGER's Ultraviolet and Visible Spectrometer UVVS of the tail region that extends anti-sunward from the planet during the probe's three flybys (M1, M2 and M3). The seasonal conditions during these flybys were different in each one, see table 2.11 from (McClintock et.al 2009), for instance the TAA during M1 ( $285^\circ$ ) and M2 ( $293^\circ$ ) were pretty much close so it is expected that the variations in the Na tail are not significant compared to M3 ( $331^\circ$ ). Figure 2.12 illustrates the Na intensity distributions during the three flybys, and showing the effect of solar radiation pressure which was minimum during M3 leading to a very weak Na tail, and maximum during both M1 and M2 where the tail was more populated with Na atoms.

		Flyby		
		M1	M2	M3
True anomaly angle (degrees)		285	293	331
Heliocentric distance $r$ (AU)		0.35	0.34	0.31
Heliocentric radial velocity $dr/dt$ (km/s)		-9.7	-9.2	-4.9
Radiation acceleration* (cm s <sup>-2</sup> )	Na	176.4	179.2	89.1
	Ca	52.4	53.6	38.0
	Mg	1.8	1.8	2.0
$g$ value† (photons s <sup>-1</sup> atom <sup>-1</sup> )	Na (589.8 nm)	22.89	23.30	12.64
	Na (589.2 nm)	37.44	38.04	17.71
	Mg (285.3 nm)	0.315	0.318	0.339
( $\lambda$ in vacuum)	Ca (422.8 nm)	21.54	22.07	16.19
	Ca <sup>+</sup> (393.5 nm)	2.85	2.95	2.87

\*Radiation acceleration for atoms at rest with respect to Mercury. † $g$  values, or emission probabilities, for atoms at rest with respect to Mercury (16).

Figure 2.11: The relevant parameters for the three flybys of MESSENGER (McClintock et.al. 2009).

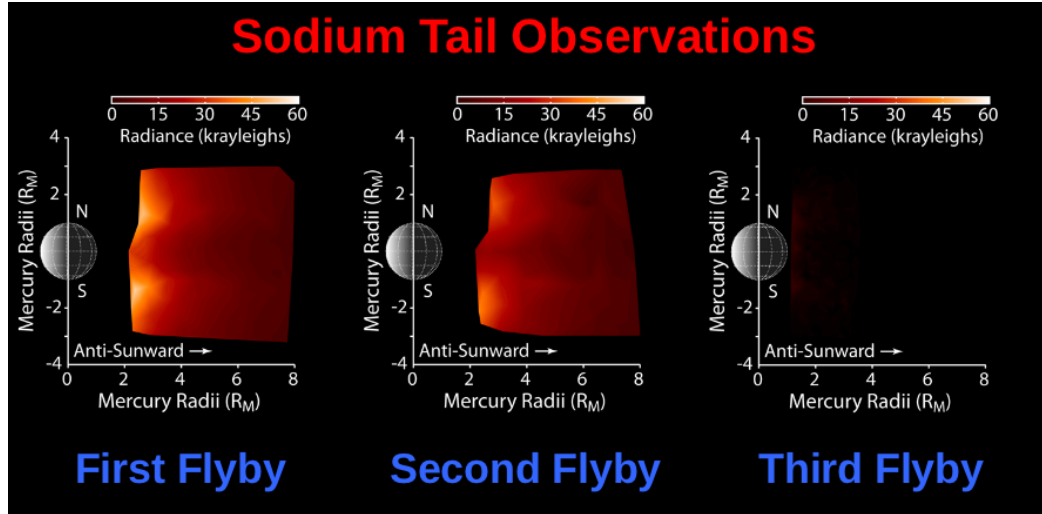


Figure 2.12: Comparison of observations from the first, second and third MESSENGER flybys illustrating the almost vanishing sodium tail during M3 compared to M1 and M2 where radiation pressure effects on Na were stronger, producing a more populated tail with emission 20 times more intense.

# CHAPTER 3

## Observations and Data Reduction

### 3.1 Data and Facility

Mercury’s sodium exosphere was observed at the McDonald Observatory located in Texas, using the 2.7 m Harlan J.Smith Telescope (Figure 3.1) and a Cross-Dispersed Echelle Spectrograph (TS2) which was installed on the coude focus of the 2.7 m telescope. The data were taken on September 28, 29 and 30 in 2009 around the MESSENGER third flyby of the planet Mercury. The resolving power of the spectrograph ( $\lambda/\delta\lambda$ ) is 400,000 which enables the distinction of the sodium emissions from the surface reflection of Mercury and the sunlight scattered by Earth’s atmosphere. A  $2048 \times 2048$  ( $24 \mu\text{m}$ ) pixels Tektronix CCD was used, it is cooled to very low temperatures with N2, data with a bandwidth of  $\sim 1.5 \text{ \AA}$  were collected at  $R \sim 400,000$ . Using a combination of the telescope, a spectrograph and a CCD camera, a plate scale of  $0.056''/\text{pixel}$  and  $0.057''/\text{pixel}$  was achieved on September 29 and September 30 respectively.

Mercury was observed after sunrise during daylight hours using two long slits (7 and 9)<sup>1</sup>, A  $30'' \times 1.2''$  spectropgraph slit (slit 9) was used in collecting data during September 28 and 29, and another  $30'' \times 0.2''$  slit (slit 7) was used during September 30 obtaining this way higher resolution data, the planet disk was about  $8.6''$  in diameter.

The spectrograph slit was aligned in different directions along the planet’s surface using an image rotator to measure the North-South (along the Terminator or limb

---

<sup>1</sup>[http://nexus.as.utexas.edu:8081/obs\\_sup/man/manuals/2dcoude/slitletinfo.html](http://nexus.as.utexas.edu:8081/obs_sup/man/manuals/2dcoude/slitletinfo.html)

direction), and East-West (along the equator) distributions of Na D2 line (see fig.3.2).



Figure 3.1: McDonald Observatory and the 2.7 m Harlan J.Smith Telescope

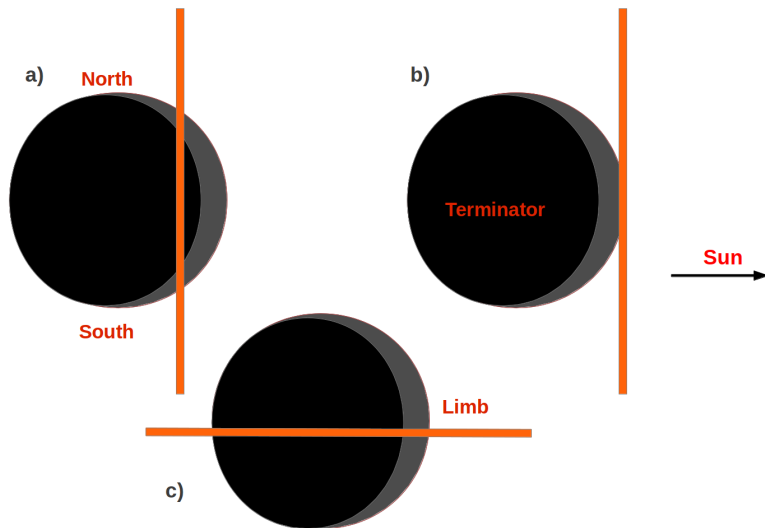


Figure 3.2: The slit orientation on the planet; a) The slit is placed at the Terminator of the planet, scanning the North-South distribution, b) The slit at the Limb of the planet scanning the North-South distribution, c) The slit along the equatorial direction of the planet scanning the East-West or Terminator-Limb distribution.

Tables 3.1, 3.2 and 3.3 show both the celestial and observational conditions prevailing on Mercury during the three sets of observation, the parameters were taken from

the database of **JPL's HORIZONS system**<sup>2</sup> which generates the ephemerides for solar-system bodies.

---

<sup>2</sup><http://ssd.jpl.nasa.gov/horizons.cgi>

Table 3.1. Data of September 28, 2009

Image	Time(UT)	TAA <sup>a</sup>	Phase angle <sup>b</sup>	$V_{M/S}$ <sup>c</sup>	$V_{M/E}$ <sup>d</sup>	Ang-diam <sup>e</sup>	Illum <sup>f</sup>	Exp <sup>g</sup>	slit position <sup>h</sup>
Image23	14:50	320.3	133.7	-6.4	37.8	8.9	15.4	720	N-S
Image24	15:04	320.4	133.6	-6.4	37.8	8.9	15.5	720	N-S

<sup>a</sup>TAA: the True Anomaly Angle of Mercury's heliocentric orbit position; the angle in Mercury's orbit plane from the orbital periape direction to Mercury, measured positively in the direction of Motion (degrees).

<sup>b</sup>Phase Angle: it's the Sun-Mercury-observer angle; the interior vertex angle at Mercury's center formed by a vector to the apparent center of the Sun and the apparent vector to the observer (degrees).

<sup>c</sup> $V_{M/S}$ : The radial velocity of Mercury with respect to the Sun (km/s).

<sup>d</sup> $V_{M/E}$ : The radial velocity of Mercury with respect to the observer on Earth (km/s)

<sup>e</sup>Ang-diam: The equatorial angular width of Mercury's full disk, if it were fully visible to the observer (arcseconds).

<sup>f</sup>Illum: Fraction of Mercury's circular disk illuminated by the Sun (%).

<sup>g</sup>Exp: Exposure time (seconds).

<sup>h</sup>slit position: the slit orientation across Mercury; N-S for slit oriented across the terminator-limb direction, E-W if it's along the equator . For N-S orientation, /T if the slit was positioned at the Terminator of the planet and /L if it's at the Limb.

Table 3.2. Data of September 29, 2009

Image	Time(UT)	TAA (°)	Phase angle(°)	$V_{M/S}$ (km/s)	$V_{M/E}$ (km/s)	Ang-diam('')	Illum(%)	Exp(s)	slit position
Image23	15:41	326.5	127.5	-5.5	40.8	8.6	19.5	720	N-S/T
Image24	15:54	326.5	127.4	-5.5	40.7	8.6	19.6	720	N-S/T
Image25	16:11	326.6	127.3	-5.5	40.7	8.6	19.6	720	N-S/T
Image29	17:33	326.9	127.0	-5.4	40.7	8.6	19.8	720	N-S/L
Image30	17:45	327.0	126.9	-5.4	40.7	8.6	19.9	720	N-S/L
Image31	18:03	327.1	126.8	-5.4	40.7	8.6	19.9	720	N-S/L

Table 3.3. Data of September 30, 2009

Image	Time(UT)	TAA (°)	Phase angle(°)	$V_{M/S}$ (km/s)	$V_{M/E}$ (km/s)	Ang-diam('')	Illum(%)	Exp(s)	slit position
Image11	13:13	331.923	122.111	-4.7	43.1	8.422	23.417	900	N-S/T
Image12	13:29	331.973	122.062	-4.7	43.1	8.420	23.454	900	N-S/T
Image13	13:44	332.075	121.962	-4.7	43.1	8.415	23.528	900	N-S/T
Image14	14:00	332.126	121.913	-4.7	43.1	8.413	23.564	900	N-S/T
Image15	14:16	332.177	121.863	-4.6	43.1	8.411	23.601	900	N-S/T
Image28	16:20	332.736	121.318	-4.6	43.2	8.387	24.006	720	E-W
Image29	16:32	332.787	121.268	-4.5	43.2	8.385	24.043	720	E-W

## 3.2 Longslit Spectroscopy

In spectroscopy, for unresolved point sources , like stars, spatial details do not contribute in studying the physical properties of the target, we only need to record light at many wavelengths. But for studying extended sources, like galaxies, nebulae and planets, we need both spatial and spectral details because it is expected that physical properties will vary as a function of position in these objects. Longslit spectroscopy is one of the technique used by astronomers to record both spatial and wavelength information.

Figure 3.3a) is a simple long-slit spectrograph taken from (Pogge 1992), the light from the target is focused onto the slit, the rays passing through the slit are collimated and sent to the dispersion element (grating or prism), and finally the dispersed light is imaged using a CCD camera.

Figure 3.3b) presents the optics of a cross-dispersed echelle spectrograph, this instrument is used to obtain high resolution spectra using an echelle grating to produce the high spectral resolution and a cross disperser to separate the orders and project them onto the CCD detector.

In the following, we will be using terms like **columns** and **lines**, this is to distinguish between the spatial and spectral directions of the data frames reduced by IRAF. In our data, the spectral direction is along **lines** (y-direction of Figure 3.4), and the spatial direction is along **columns** or slit direction (x-direction of Figure 3.4)

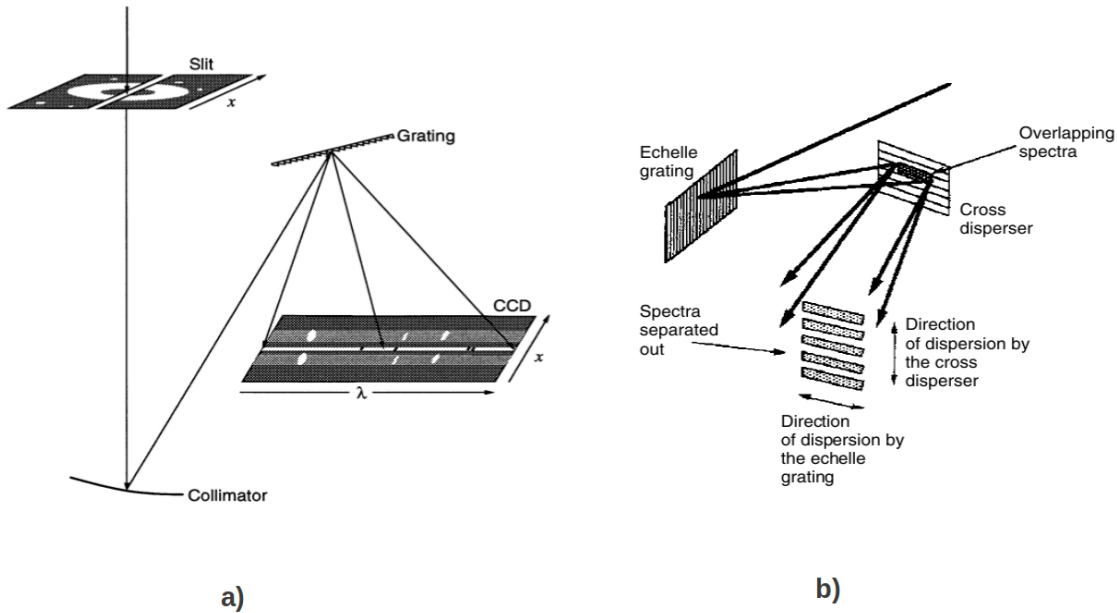


Figure 3.3: a) Simple long-slit spectrograph, b) General illustration of a cross-dispersed echelle spectrograph.

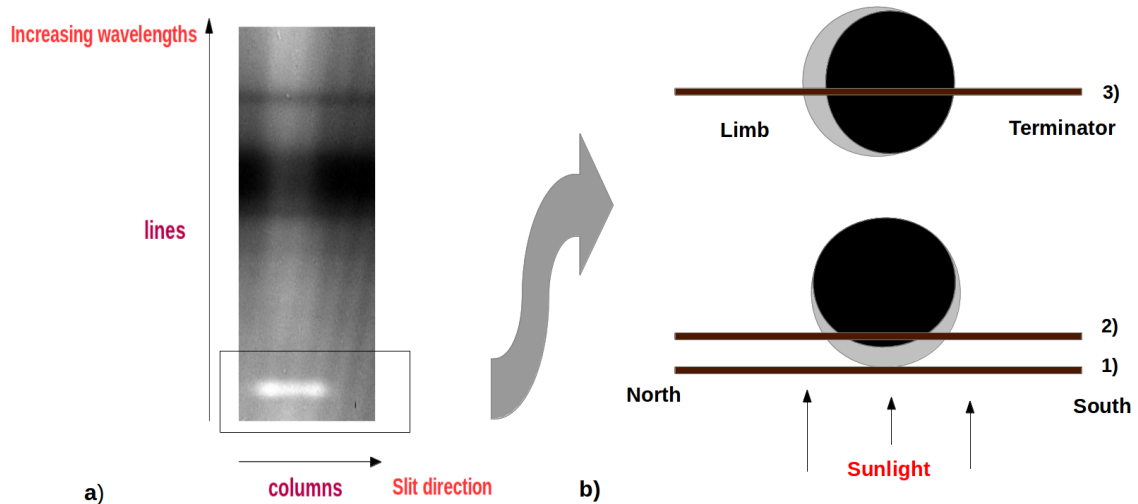


Figure 3.4: a) The frame of data images with the spectral and spatial axis shown, b) A visualization of the slit and planet directions in the data images: 1) slit on the limb yielding the north-south distribution of sodium emission, 2) slit on the terminator yielding the north-soth distribution, 3) slit on the equator yielding the east-west(terminator-limb) distribution.

### 3.3 Data reduction

My data reduction steps begin with the standard ones necessary for all longslit spectra: registration of the images, bias removal, flatfielding, trimming the sky, making a sky template, sky-subtraction. Additional necessary reduction were also incorporated and explained in details in the following sections.

#### 3.3.1 Geometric Correction: Registration

This step corrects the images for misalignments in either, or both, lines and columns. We start by using the task **noao.plot.implot** and plotting the spectrum from end of the image (by typing ”:c” in interactive mode), expand it around an absorption line (by typing ”e” at the two corners of the desired position ) and overlay (by typing ”o” for overplotting) the spectrum from the other end. If the spectrum does not line up (Figure 3.5, left panel), the IRAF<sup>3</sup> registration programs must be applied. Also the alignment of the lines can be checked by the same procedure, by plotting lines (”:l”) instead of columns(”:c”) as shown in figure 3.6. As it turns out, the emission lines shift by several pixels from one end of the line to the other. There are two routines that will allow such corrections and can be found in **images.immatch**, which are **geomap** and **geotran**. The program **geomap** is run first, it calculates the coordinate transformation necessary to register the images, next, **geotran** is run to apply such transformations on the data images.

The **geomap** program requires input tables which indicate how the image should be transformed. The first step in producing such tables is to plot the spectrum at a column at the low end of the spectrum, because the data is noisy, we plotted average of columns, here we plotted the average of columns ”:c 300 450” that are centered on column 375. Then, the spectrum is expanded around a sharp absorption line as

---

<sup>3</sup>IRAF is distributed by the National Optical Astronomy Observatories, which are operated by the Association of Universities for Research in Astronomy, Inc., under cooperative agreement with the National Science Foundation.

noted above (the Fraunhofer absorption line), and the line number at its minimum is recorded, the line number at column 375 is 556.802 . We repeat the procedure at the other end of the line. In this case column 625 (:c 600-650) has the same absorption line minimum at line 556.855. The column half way between them is 500. Then we make an assumption that the spectral line will fall halfway in between the two (at column 500) and its value is the average of both extremes, 556.8285 . Hence, everything is registered to the middle column 500 . All this yields the first three lines for the first input file(table 3.4). Going to a different spectral feature a couple of hundred lines away (the telluric absorption line) will yield another three lines. For instance, column 375 with absorption line minimum located at line 712.653, then column 625 with the same line placed at 702.976 will result in the middle column location (column 500) of 707.8145.

An input file with all this information should be created. The first pair of numbers in the table are the output (desired position) and the second pair are for input (actual position of the lines before registration). Note that the second numbers in the output pairs are the same in each set of three.

Table 3.4: The input file for column registration, input1.

375	556.8285	375	556.802
500	556.8285	500	556.8285
625	556.8285	625	556.855
375	707.8145	375	712.653
500	707.8415	500	707.8145
625	707.8145	625	702.976

The same step is repeated in order to register the lines. The markers used in this case are the minimums between lines, table 3.5 is an example of the input file for line registration.

Figure 3.6 shows the misalignments along the lines.

Table 3.5: The input file for line registration, `input2`

302.96	125	294.927	125
302.96	400	302.96	400
302.96	675	310.993	675
858.434	125	850.040	125
858.434	400	858.434	400
858.434	675	866.828	675

So we have two input files, `input1` to register the columns, and `input2` to register the lines. We run the program **geomap** that takes as input the table `input1`, it then requires the name of the output data file `database1` that will contain the necessary coordinate transformation, and thirdly, the dimensions of the image. The command **imheader** indicates the dimensions of the image, which are in this case [1056, 1024]. When we run **geomap**, we will get a plot projected to the computer screen. If everything is OK, there will be words to that effect on the plot, we close the plot hitting the key 'q'. The output from geomap is the database file, which contains all the numbers needed to make the coordinate transformation in the program **geotran**. After obtaining the file `database1`, we apply **geotran** on the data with input `input1` and `database1` files obtained above. We obtain the `column` registered images. We run geomap again, this time taking as input `input2` generating the database file for line registration `database2`. The task **geotran** is run again, this time on the column registered data, taking as input `input2` and `database2`, the result is the registered data images.

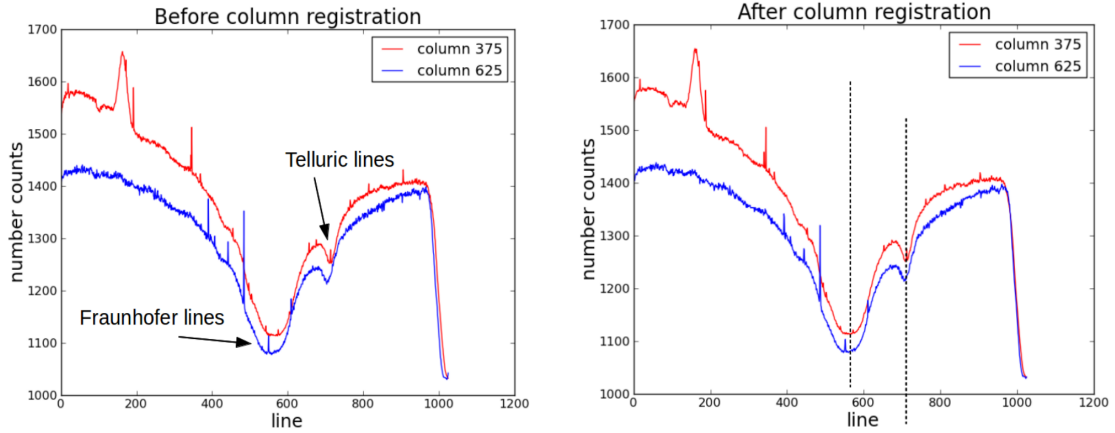


Figure 3.5: Before and after column registration, the dashed lines shows the alignment of the columns after registration.

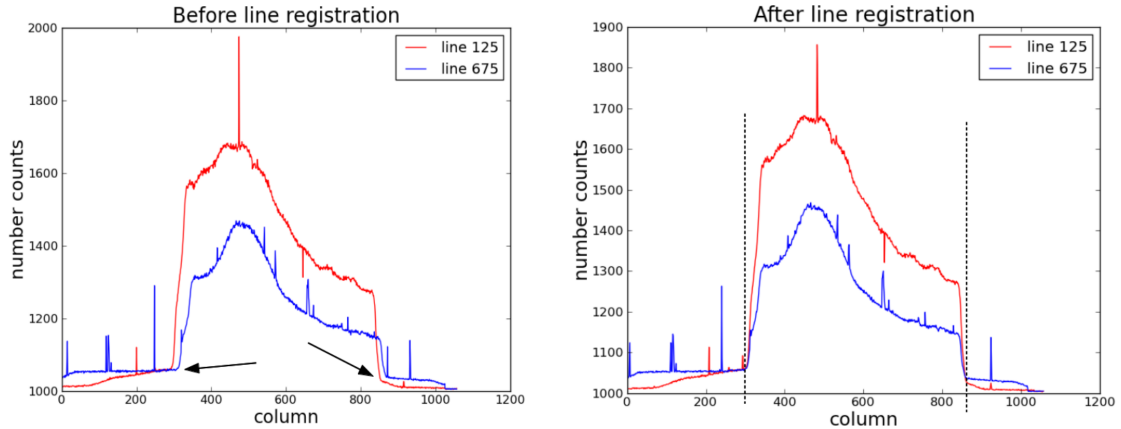


Figure 3.6: Before and after line registration, the dashed lines shows the alignment of the lines after registration.

### 3.3.2 Cleaning up the Data

In this section, I will be presenting a detailed description of every step in my data reduction, along with the methods I developed to solve some of the problems I encountered during the reduction, showing the complete methods and results.

#### **ZeroCombine**

Bias frames , which are zero second integration exposures, are necessary because they provide information on the underlying signal level (bias level) and the readout noise within each frame. Bias frames amount to taking observations without exposure to light (shutter closed), for a total integration time of 0.000 seconds, it will be subtracted from the image of the object in the sky, which results in an image with count levels that designate the light received from the observed object. To combine all the bias-images into a Master bias frame, I use the task **zerocombine**:

```
> zerocombine @zero.lis ccdtype="" output="Zero.fits"
```

#### **Cosmic Ray Removal**

The cosmic ray removal was performed by the IRAF task L.A.Cosmic which was created by Piter van Dokkum <sup>4</sup>. This task removes cosmic rays from astronomical images via Laplacian algorithm. To do this, first, I downloaded the program from the official L.A.Cosmic webpage, there are two versions, one for imaging and the other for spectroscopy. From the download section in the webpage, I copied the text that makes up the program, and saved it as a CL script: *lacos\_spec.cl* in the IRAF directory. The task is registered in the package **stsda**s<sup>5</sup> in IRAF:

```
> stsda
> task lacos_spec= Iraf directory/lacos_spec.cl
```

This task takes as input the data images we wish to clean, the output is the name of

---

<sup>4</sup><http://www.astro.yale.edu/dokkum/lacosmic/>

<sup>5</sup>The Space Telescope Science Data Analysis System

the cleaned image, and the bad pixel map which is the file that contains information about where the 'bad' pixels (cosmic rays) are located on the image:

```
> lacos_spec input output mask
```

Here are the spatial and spectral profiles before the removal of cosmic rays:

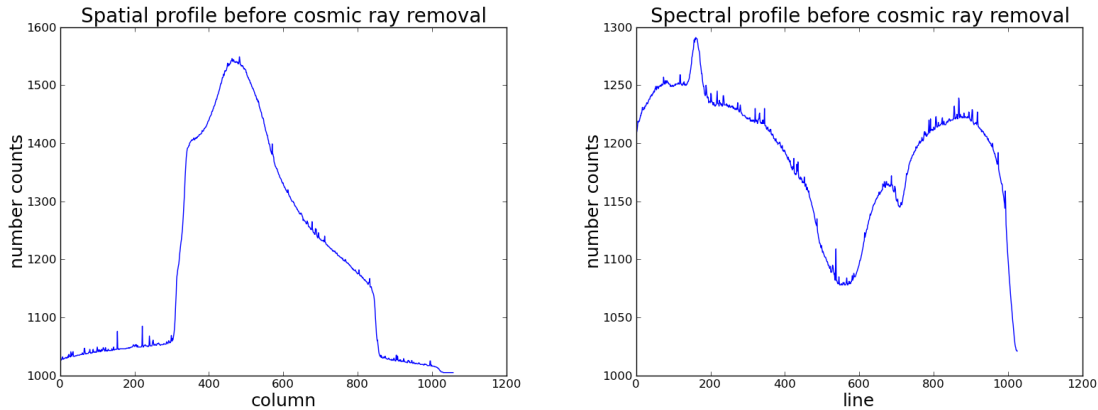


Figure 3.7: The spatial and spectral profiles before cosmic ray removal.

And after the correction:

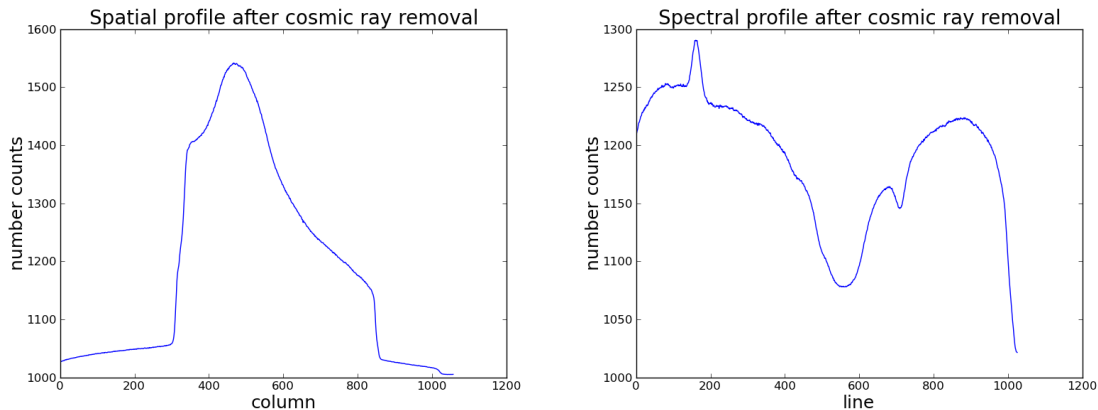


Figure 3.8: The spatial and spectral profiles after cosmic ray removal.

## Trimming data images

The data are trimmed to remove the overscan region of the CCD camera, this is done by examining the image using **ds9** image viewer, and then using the task **images.imutil.imcopy** to trim only the part containing the slit and planet.

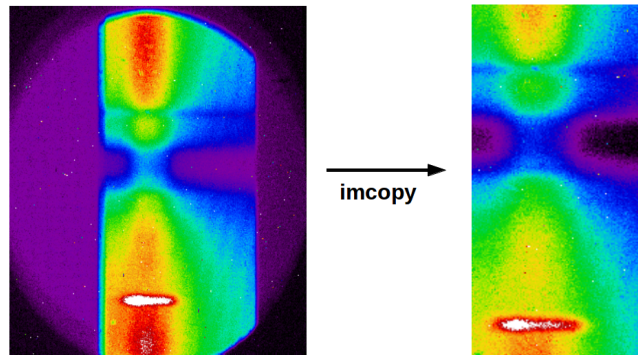


Figure 3.9: Trimming data images using *imcopy*.

## Flatfielding

Within the CCD, each pixel has a slightly different gain or QE value when compared with its neighbors. In order to flatten the relative response for each pixel to the incoming radiation, a flat field image is obtained and used to perform this calibration. So a flat field image would consist of uniform illumination of every pixel by a light source of identical spectral response to that of our object frames. For spectroscopic applications, flat fields are obtained via illumination of the spectrograph slit with a quartz or other high intensity projector lamp.

The task **flatcombine** is used to make the master flat.

```
>flatcombine @flats.lis ccdtype="" output="Flat.fits"
```

The task **imstat** is used to give the mean value of the counts in the Master Flat, the latter is divided by the mean value in order to obtain the normalized Master Flatfield:

```
>imarith Flat.fits / mean Flatnorm.fits
```

The object data are flat fielded, for that I use **imarith** to divide all mercury images by the normalized Master flat:

```
>imarith @mercury.lis / Flatnorm.fits @ffmercury.lis
```

Where **mercury.lis** represents the list of debiased, corrected for cosmic rays mercury images, and **ffmercury.lis** that of the flatfielded ones.

### Making a sky template

Because the slit extended well beyond the planet, the image will comprise the following spectral features:

1. The diffuse sky light (sky background).
2. The reflectance spectrum from the planet (the Mercury Fraunhofer absorption line).
3. The exospheric emission of the Sodium lines.

Figure 3.10 illustrates the main spectral features seen in the flatfiled mercury image.

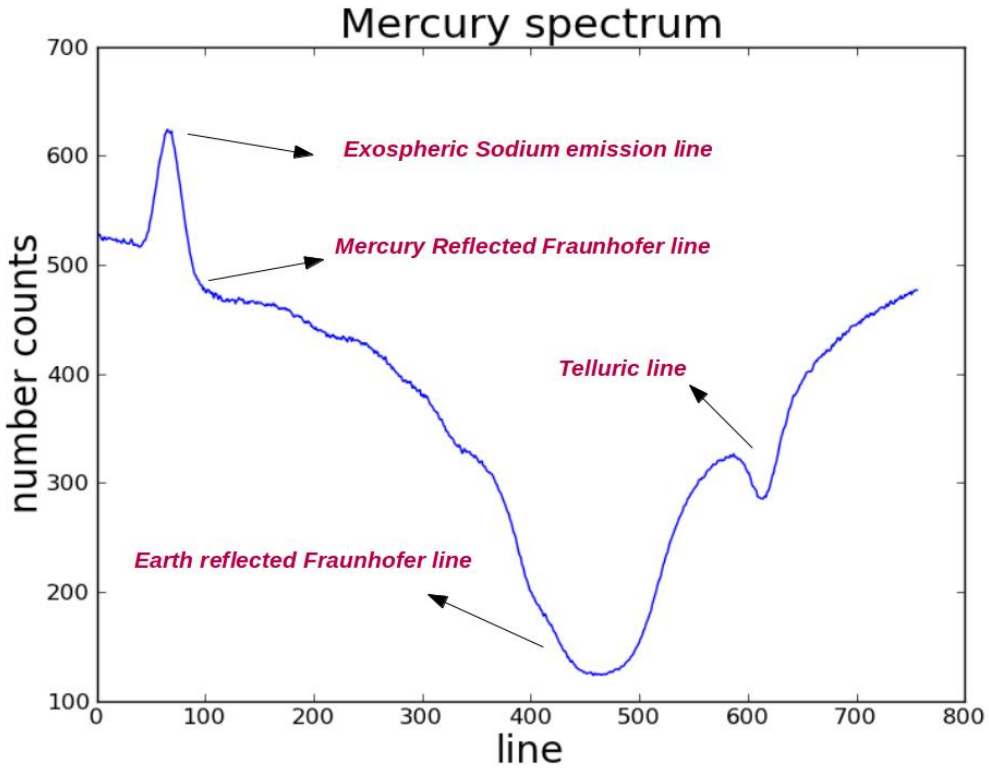


Figure 3.10: The different spectral features of the data images: left to right, the Na D<sub>2</sub> emission line, the reflected Fraunhofer line from the surface of the planet which was weak as the planet was a crescent and not very bright, the sky background which contains the Earth reflected Fraunhofer line plus the telluric line from Earth's atmosphere.

The next step of the data reduction is making a template sky spectrum and then subtract it from the flatfielded mercury image above.

The removal was done using the sky regions at the end of the slit. After the flatfielding, we examine the images to see where the sky regions lie, the sky spectrum contains a Fraunhofer absorption line plus a telluric line from the Earth's atmosphere, the regions where the spectrum does not contain any sodium line, and where the sky spectrum is at the same intensity scale in all pixels, is the sky region.

I use the task **images.imutil.imcopy** to trim the sky part from the end of the slit as shown in the figure 3.11, then used the task **blkavg** to obtain the averaged sum along columns of the sky (1D vertical cut), after that, I used the task **blkrep** to replicate the block-averaged sky to the dimension of the initial image. Figure 3.12 shows the steps for making the sky image.

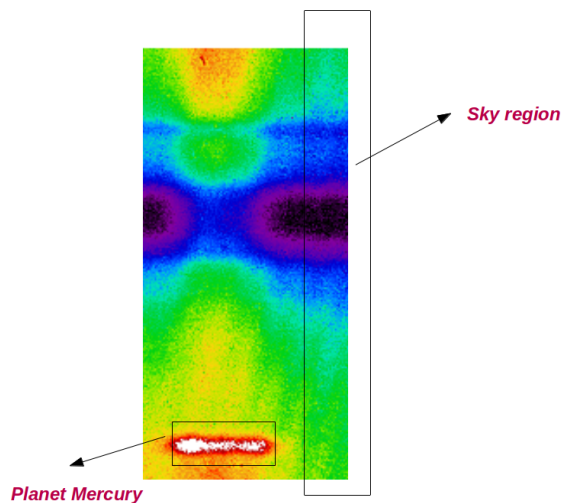


Figure 3.11: The right side of the slit is the sky region.

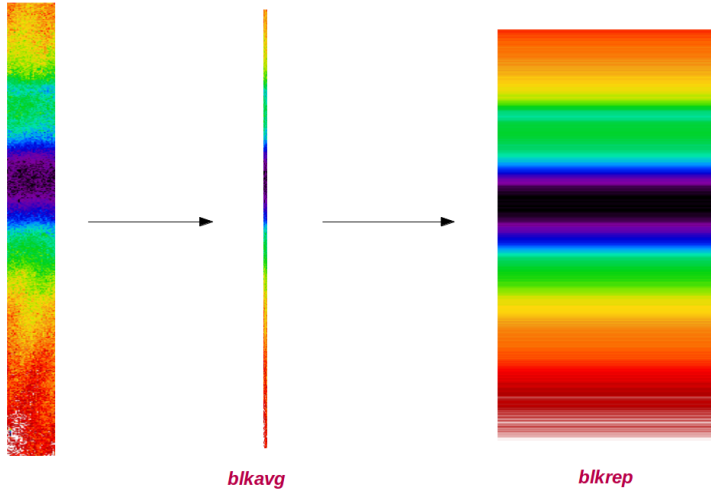


Figure 3.12: The process of making the sky image, from left: the sky region is trimmed from the initial image, then **blkavg** is used to form a 1D cut, and finally **blkrep** is used to replicate this cut to the initial dimensions.

### Sky Subtraction

After I make the sky template (Figure 3.13 right panel), I use **images.imutil.imarith** to subtract it from the original mercury (sodium+sky) spectrum (Figure 3.13 left panel). Now I am left only with the exospheric sodium emission and the reflectance from the surface of the planet (reflected Fraunhofer line) as shown in Figure 3.14.

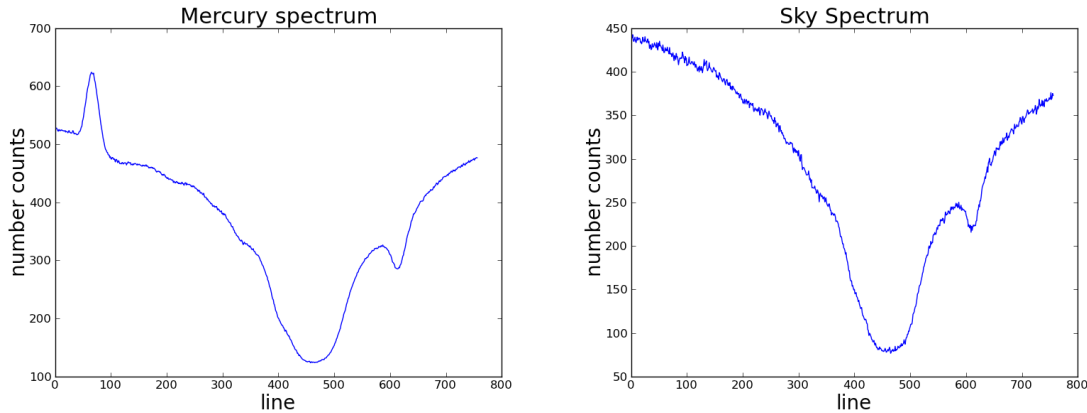


Figure 3.13: Left: the sodium emission with the sky lines, right: the sky spectrum.

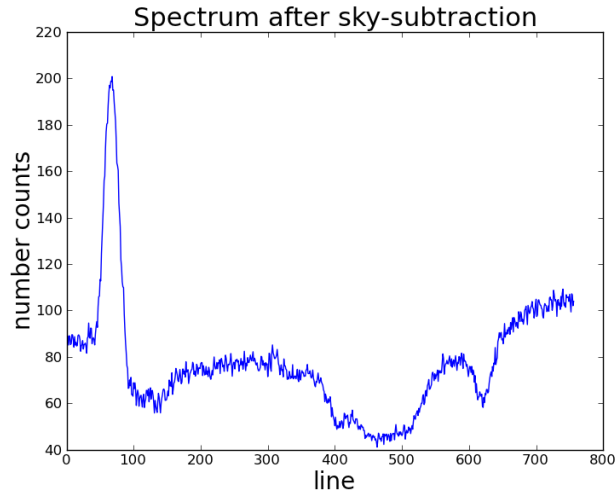


Figure 3.14: The spectrum after sky-subtraction.

### 3.4 Improving the Flatfielding

As we can see in figure 3.14 above, we still have some residuals after the sky subtraction, which means that the sky spectra extracted from parts of the slit (the solar Fraunhofer and atmospheric telluric lines) far from Mercury is not on the same intensity scale as the sky spectra at the Mercury regions of the slit, and apparently the

shape of the sky lines is changing from pixel to pixel along the slit. For this reason, we thought of different ways to scale the sky to make it at the same intensity level in all regions of the slit, and therefore to minimize the residuals seen in the spectrum after the sky removal.

The method to correct for the non-uniform illumination is explained in details in **AppendixA**. After applying the corrections, I trimmed the sky part from the corrected images, and made a sky template following the same procedures as stated in section 3.3.2.

The sky spectrum is scaled to the mercury spectrum after correction as can be seen in Figure 3.15:

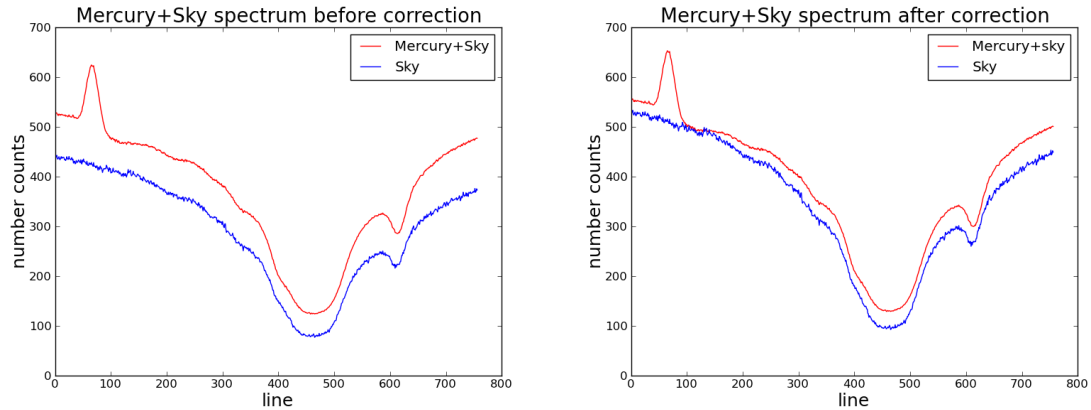


Figure 3.15: The averaged mercury spectrum before sky subtraction overplotted with the sky spectrum before and after correction.

After making the corrected sky template, I subtract it from the corrected flat-fielded mercury images to see how this correction affects the residuals in the spectrum after the sky subtraction, the next images show the sky-subtracted spectra of some of the mercury images before and after the correction:

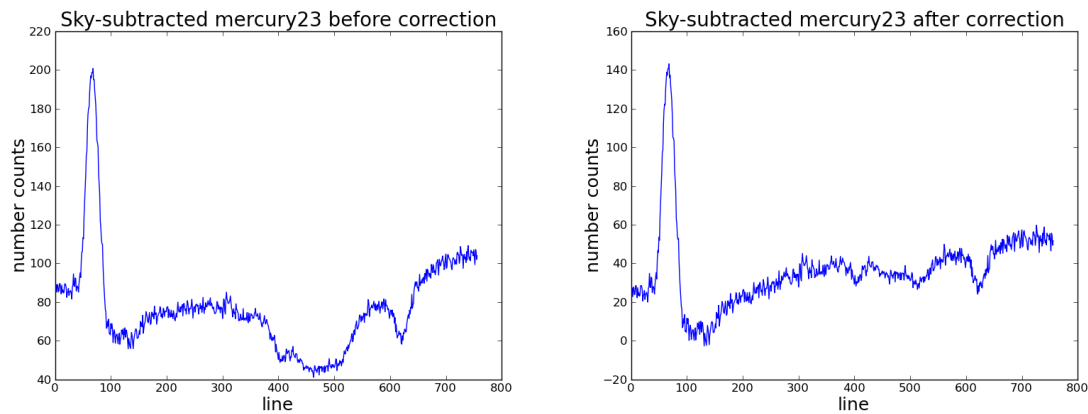


Figure 3.16: The sky-subtracted spectrum of image 23 before and after the correction.

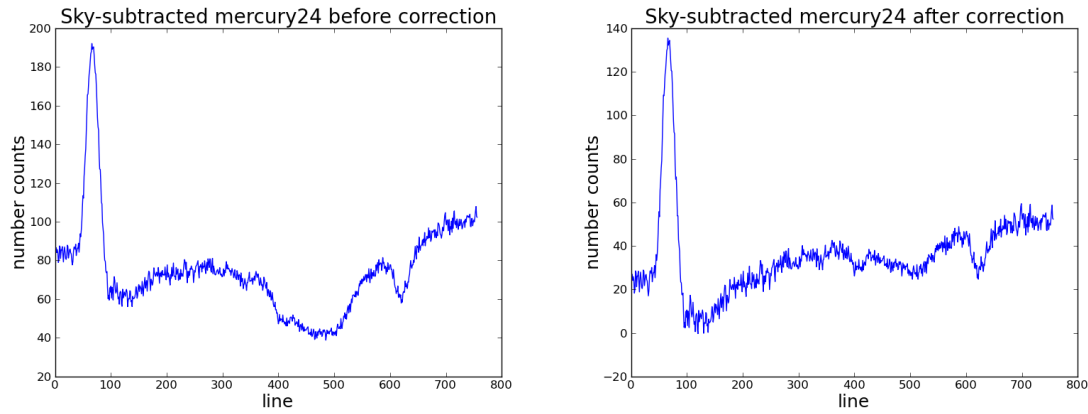


Figure 3.17: .  
The sky-subtracted spectrum of image 24 before and after the correction.

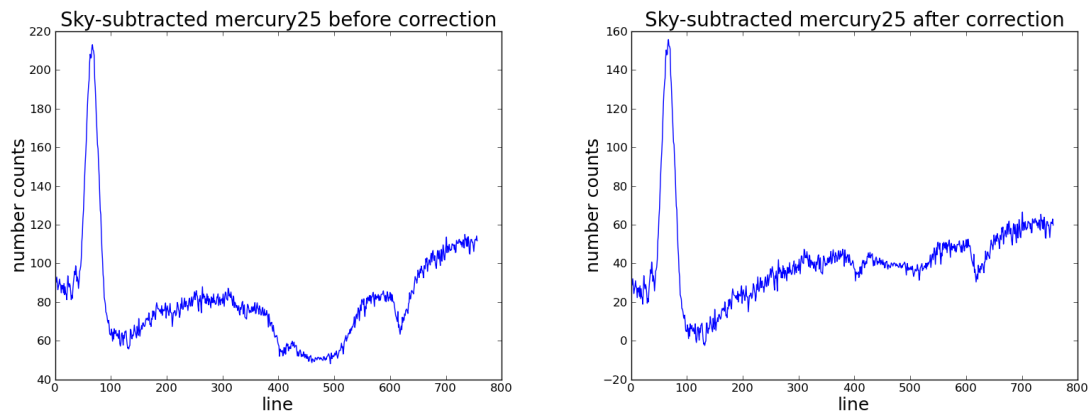


Figure 3.18: The sky-subtracted spectrum of image 25 before and after the correction.

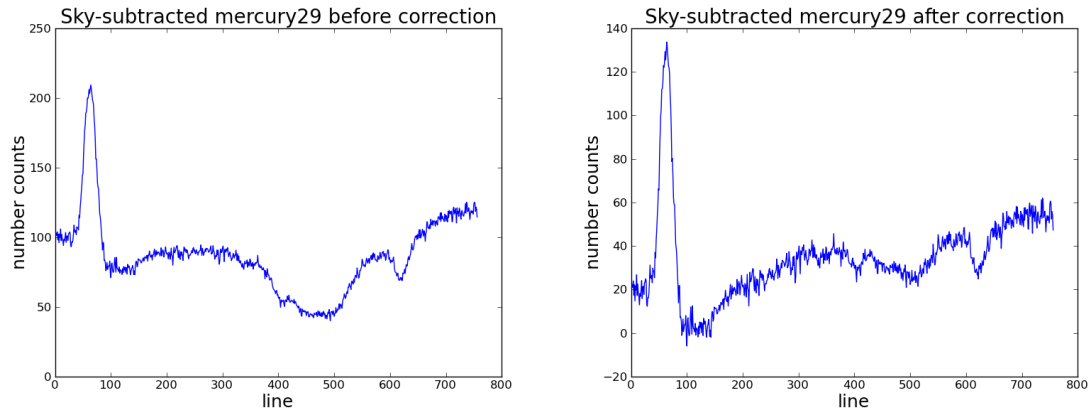


Figure 3.19: The sky-subtracted spectrum of image 29 before and after the correction.

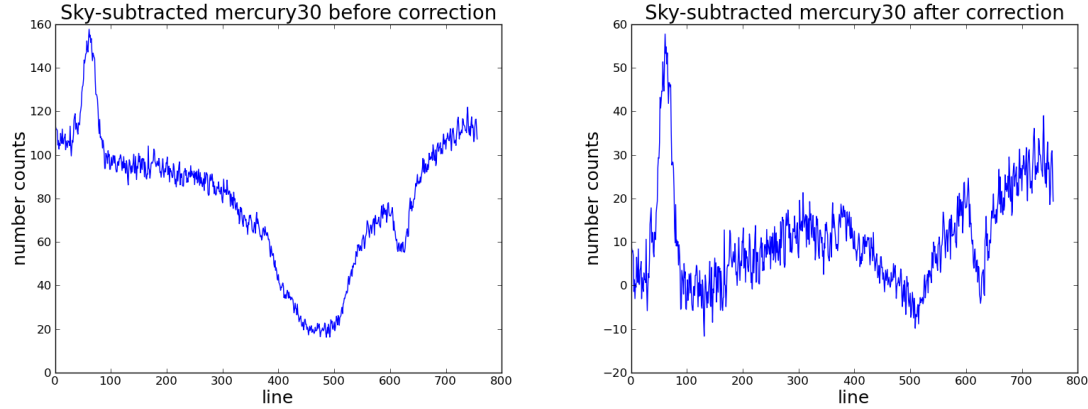


Figure 3.20: The sky-subtracted spectrum of image 30 before and after the correction.

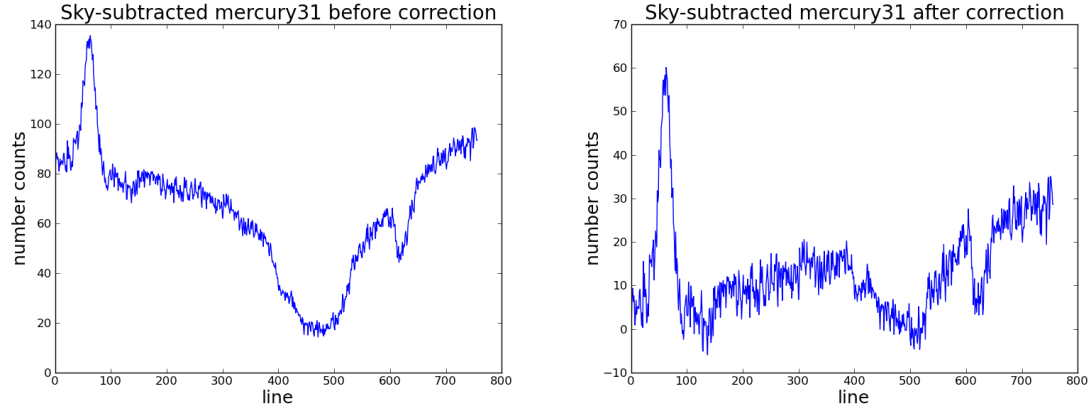


Figure 3.21: The sky-subtracted spectrum of image 31 before and after the correction.

We can see that our corrections have considerably reduced the residuals after the sky subtraction.

## 3.5 Sodium line Extraction

After correcting the images for the non-uniform illumination, the sky-subtracted images are used now to extract the sodium line emission and study their spatial

distributions. The sky-subtracted spectra as seen in images 3.16 to 3.21 contain the sodium line emission plus the solar Fraunhofer absorption line reflected off the surface of the planet, the reason why they are doppler shifted is explained earlier in section 2.4.3.

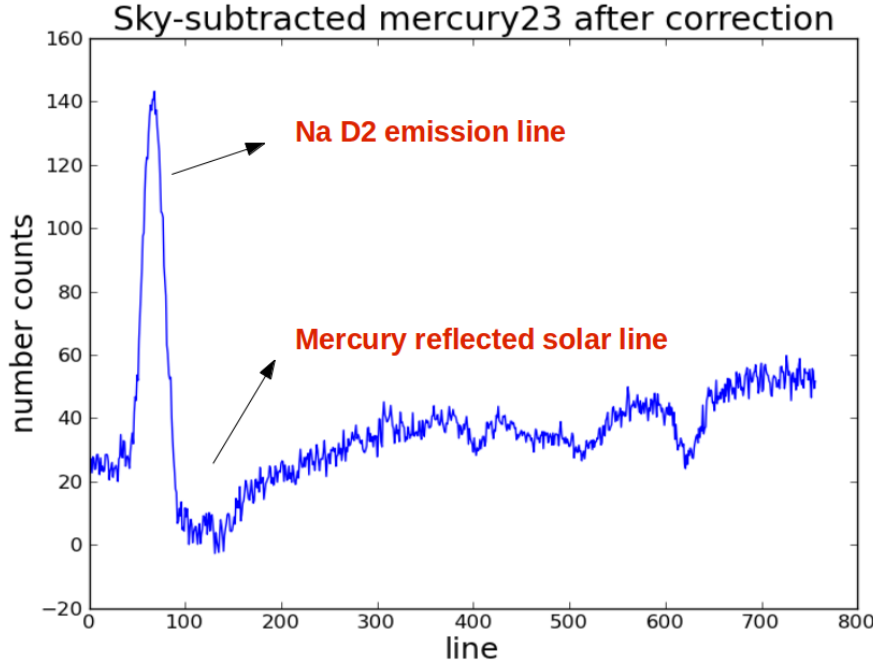


Figure 3.22: The averaged spectrum along columns after sky subtraction.

The next step is to extract the sodium line emission from each pixel along the slit and only in pixels where the sodium emission is there, since the slit extends well beyond the surface of the planet, and there are regions where the sodium emission is very weak, or not apparent at all. So first thing to do is use the task **implot** in IRAF to check the pixels where the sodium emission is present, for instance for some images in the data of September 29 of dimension  $362 \times 756$  (the dimension along the slit is 362), the sodium emission begins to appear at pixel 30 and ends at pixel 260, and hence, this region of the slit is where we want to extract the sodium emission from.

Extracting the sodium line can be done by fitting a **voigt** profile to the solar Fraun-

hofer reflected line, and subtracting it from the spectrum and the resultant is the sodium D2 emission line (Mongano et al. 2007). But in my thesis, I came up with another method taking advantage of the different tools and tasks available in IRAF and Python, and developed my own routines thanks to the CL scripting language in **IRAF**, the detailed description of these routines is presented in chapter 4, but for a general description, the script will extract the sodium emission lines averaging every 2 pixels along the slit in the region we specified before where the sodium emission is apparent. Then, the sodium line in every pixel is fitted using the appropriate tasks of IRAF, then subtracted from the spectrum to be left with the Fraunhofer solar reflected line, the latter will be subtracted from the original spectrum, and the result is the fitted sodium emission line.

After extracting the sodium emission lines from all the pixels along the slit, another script is run on the resultant profiles in order to read and save their integrated line fluxes in ADU units. These fluxes are used later to be calibrated as will be explained in the next section. Finally, intensity maps of sodium emission are generated to study their distribution for the different slit-planet orientation.

## 3.6 Flux Calibration

The next step in the data reduction is converting the intensities of the extracted sodium emission from ADU's to a standard unit used for emissions from atmospheres, the Rayleigh (Chamberlain & Hunten 1987), which is the CGS unit of flux and represents the number of photons emitted in all directions per square centimeter of receiver per second:

$$1 \text{ Rayleigh} = 10^6 \text{ photons cm}^{-2} \text{ s}^{-1} \quad (3.1)$$

Usually, a comparison non-variable star near the target of known flux is taken at the time of observations in order to be used for calibrating the flux of the target, but in the case of planetary atmospheres, and if no calibration source is observed along

with Mercury, then the surface of the planet itself can be used as a standard candle to calibrate both the continuum and exospheric emissions.

For this we have to use the **Hapke** method (Hapke 1993), it is based on the following: a theoretical model of Mercury's reflectance is generated according to the observational parameters: the phase angle, the apparent diameter of the planet, the fraction of the illuminated part of the planet, the heliocentric distance, then the maximum bidirectional reflectance value from the theoretical reflectance model at the slit position is used to find the peak of radiance from Mercury in Rayleigh, and then compared with the maximum value of the observed continuum in the slit (ADU unit), hence, a calibration factor is obtained and multiplied by the integrated flux in ADU units to convert the measured emission to Rayleigh unit.

### 3.6.1 Estimating the seeing

Knowing the seeing is crucial at this point to correctly calibrate using Hapke reflectance model (LeBlanc et al. 2008). In our observations, the seeing is not estimated, in this case the Hapke reflectance model is used to derive an estimated value of the seeing.

After generating the theoretical Mercury reflectance image for perfect seeing, this image is then convolved with Gaussians of different widths (to account for different values of the seeing), a blurred image is obtained and compared to the observed one (with the slit), the seeing (FWHM of the Gaussian) is changed until the blurred reflectance model matches the observed image, which in our observations is the guider image, and the seeing is then determined. This is detailed in what follows.

The following is the generated model of Mercury reflectance, the blurred image, and the guider image taken of the planet and the slit during the observations:

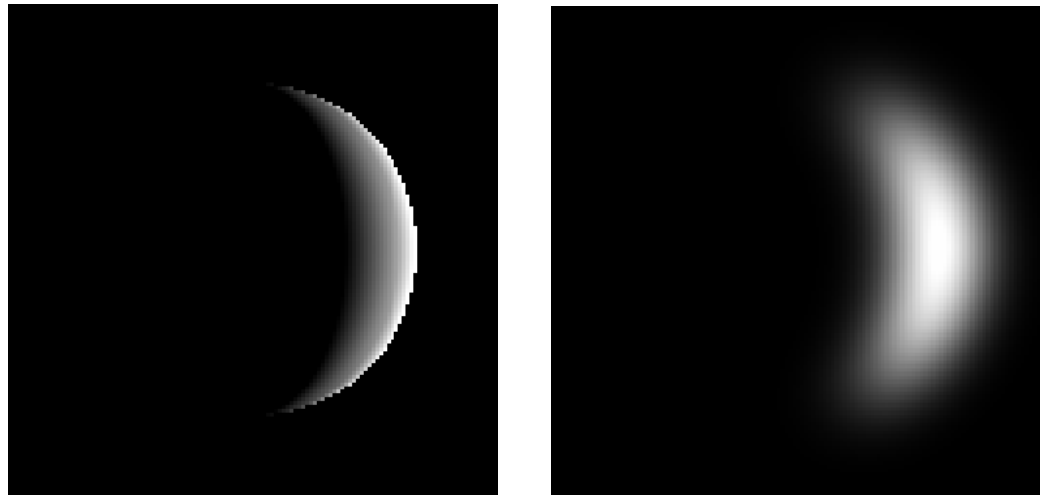


Figure 3.23: The theoretical images of suface reflection from Mercury, for perfect seeing (left) and convolved Hapke (right).

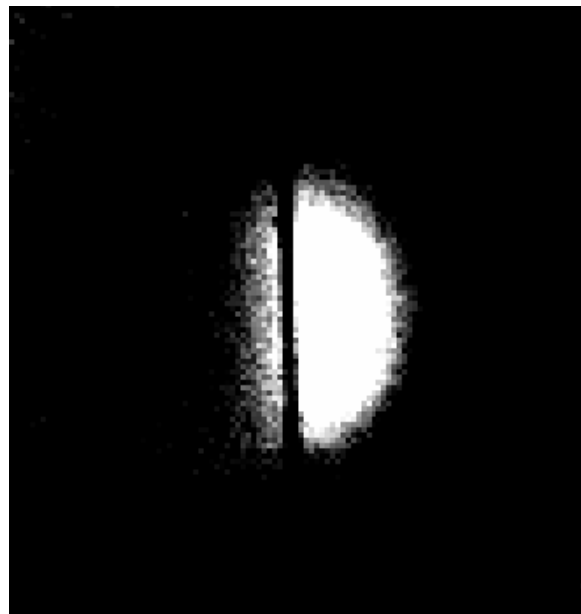


Figure 3.24: The guider image of an image data of sep29, the image shows both the slit and the planet, the image is blurry due to atmospheric seeing.

Convolving the Hapke reflectance model with different seeing values and finding a proper match with the guider image is done with IRAF, the task **images.imfilter.gauss** is first used to convolve the theoretical Hapke image with a gaussian kernel specified

by the parameter **sigma**.

The Gaussian Kernel is defined mathematically as follows:

$$G = N \times \exp(-0.5 \times (r/\text{sigma})^2) \quad (3.2)$$

$N$  is the normalization factor and  $r$  is the pixel position. The **sigma** ( $\sigma$ ) defined by the task **gauss** is related to the FWHM of the seeing by:

$$\text{FWHM} = 2\sigma\sqrt{2\ln 2} \approx 2.35\sigma \quad (3.3)$$

The  $\sigma$  parameter is expressed in *pixels*, once multiplied by 2.35 (Eq.3.3), the seeing is then obtained in *pixels*, and to convert it to *arcseconds*, we multiply it with the plate scale of the non-convolved Hapke reflectance image (0.1"/pixel).

I wrote a code that convolves the Hapke reflectance model with gaussians of different widths and take from each blurred image several thin cuts at different regions from the surface to be compared with similar cuts taken from the guider image. The cuts are taken at the equator, northern and southern regions of the planet as shown in plot a) of Figure 3.25, the plots of the cuts are overplotted to find the best fit and therefore the seeing. (Figures 3.26, 3.27 and 3.28).

Here I will present this method for one data image from the first data set (Sep29), first I trim the guider image to obtain a clear image of the slit and planet as shown in plot b) of figure 3.25, then the code will trim from each of the convolved Hapke and the guider image three cuts in the equator, northern and southern regions, these cuts are block-averaged along lines using the task **blkavg** to obtain 1D profiles, these one dimensional profiles are first normalized and then written into textfiles using the task **wspectext**, the textfile contains pixel values with their corresponding ADU counts, I use other codes written with Python in order to convert the pixels into arcseconds, since the Hapke and the guider images have two different resolutions and both profiles have to be plotted against arcseconds for accurate comparison. After converting pixels

to arcseconds, another code is used to overplot the new textfiles and visually find the best fit (best sigma), and therefore the seeing. (Figures 3.26, 3.27 and 3.28).

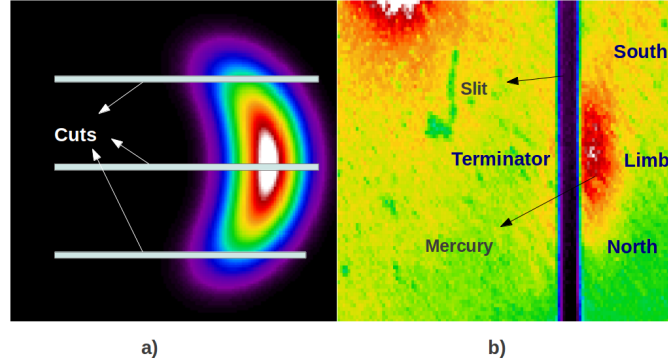


Figure 3.25: a) The blurred Hapke reflectance image and the different cuts taken at the equator, north and south of the surface, b) the trimmed guider image showing the slit on Mercury.

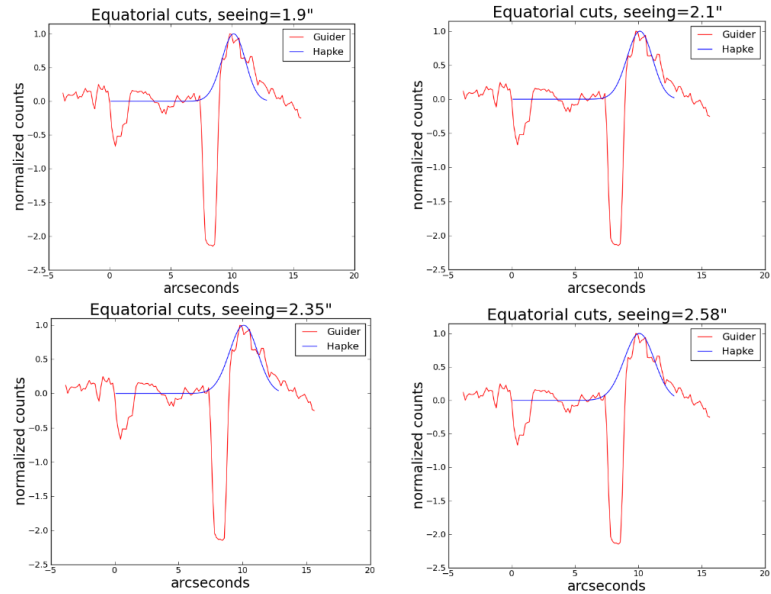


Figure 3.26: Equatorial cuts of convolved Hapke images and guider image overplotted for different seeing values.

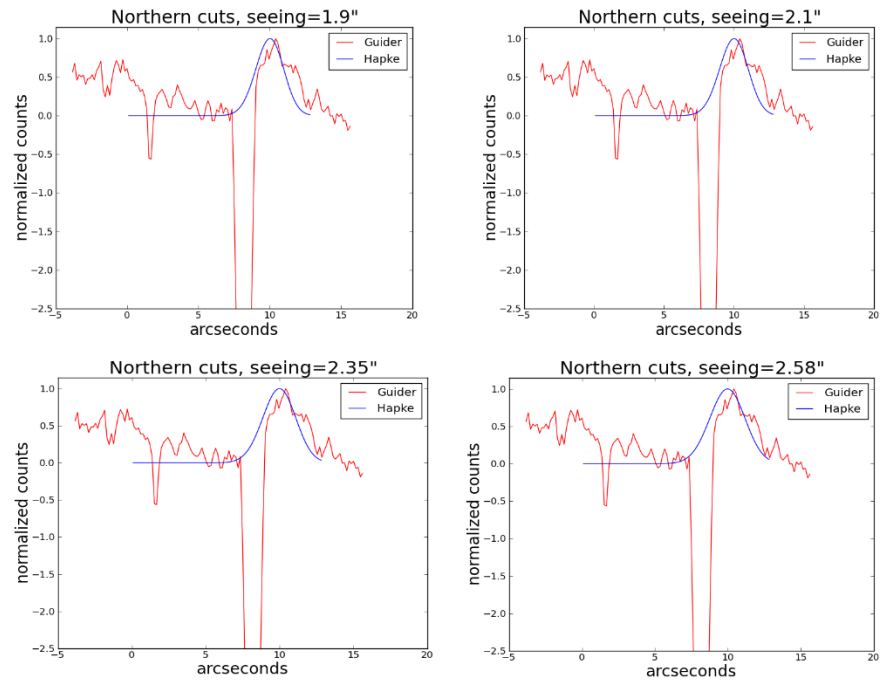


Figure 3.27: Northern cuts of convolved Hapke images and guider image overplotted for different seeing values

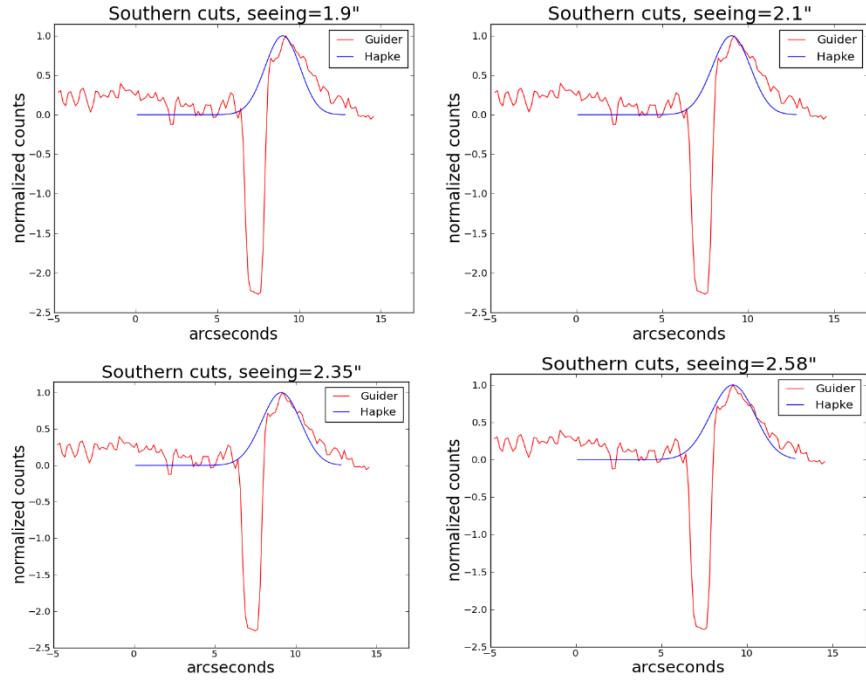


Figure 3.28: Southern cuts of convolved Hapke images and guider image overplotted for different seeing values.

By examining the plots, we make a rough estimation of the seeing value corresponding to the best fit between the cut profiles from the guider image and the ones from the convolved Hapke image. To strengthen the choice of a particular seeing value, we extract the slit profile from the blurred theoretical image and compare it with the profile of the observed continuum.

A Python code is written in order to extract from each pixel along the slit of the sky-subtracted images the corresponding continuum value, these values are written into a textfile and the corresponding pixels are converted into arcseconds using the resolution of the data ( $0.056''/\text{pixel}$ ).

One problem here is that the position of the slit on the guider image is not accurately determined because of the poor seeing, and the estimation of the slit position on the theoretical Hapke in order to extract the theoretical continuum profile is therefore tricky.

So in order to estimate the position of the slit on the surface of the planet I did the following: from the guider image, I estimate the position (in pixels) of the limb (or terminator) from the first edge of the slit. In order to know the corresponding distance in the blurred Hapke, I convert the distance into arcseconds using the plate scale of the guider image ( $0.153''/\text{pixel}$ ), and then use the plate scale of the Hapke model ( $0.1''/\text{pixel}$ ) to convert it back to pixels. Knowing the position of the limb in the Hapke image, I can calculate the position of the first cut of the slit, to know where the other cut will be, I use the plate scale of the Hapke image to convert the width of the slit ( $1.2''$ ) from arcseconds to pixels (12 pixels), and then I average the profile along these 12 pixels, this block-averaged slit profile is also written into a textfile and pixels are converted into arcseconds using the resolution of the Hapke model ( $0.1''/\text{pixel}$ ). We overplot the resultant profiles with the observed continuum extracted from pixels as shown in Figure 3.29. The results are summarized in tables 3.6 and 3.7 for all data sets.

Table 3.6. Estimation of the seeing parameters of September 29 data.

Image	$P_g$ (pixels) <sup>a</sup>	$P_g$ (") <sup>b</sup>	$P_h$ (pixels) <sup>c</sup>	Sigma	FWHM(pixels)	FWHM("
Image23	16	2.4	24	11	25.5	2.6
Image24	16	2.4	24	10	23.5	2.4
Image25	21	3.3	33	11	25.8	2.6
Image29	22	3.3	34	11	25.8	2.6

<sup>a</sup>The limb-slit(terminator-slit) distance from the guider image in pixels.

<sup>b</sup> The limb-slit(terminator-slit) distance from the guider image in arcseconds.

<sup>c</sup>limb-slit(terminator-slit) in the blurred Hapke in pixels.

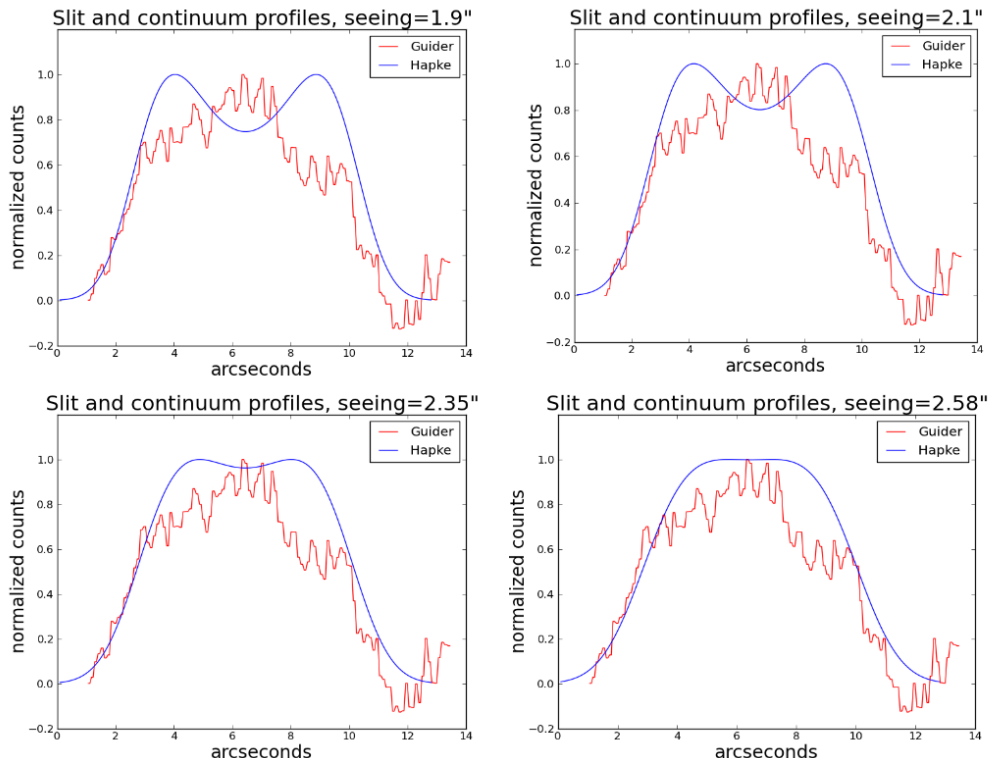


Figure 3.29: The observed continuum profiles and the theoretical slit profiles overplotted for different seeing values (normalized counts vs arcseconds).

Table 3.7. Estimation of the seeing parameters for September 30 data.

Image	Sigma	FWHM(pixels)	FWHM(”)
Image11	7.0	16.4	1.6
Image12	7.0	16.4	1.6
Image13	8.5	20.0	2.0
Image14	8.5	20.0	2.0
Image15	8.5	20.0	2.0
Image28	8.5	20.0	2.0
Image29	8.5	20.0	2.0

### 3.6.2 Calibration in Rayleigh

In this section, I will be describing how to calculate for each image its corresponding calibration factor (or **calfactor**) which depends on the instrument and gives the counts in kiloRayleighs corresponding to 1 count:  $[calfac] = kR \text{ count}^{-1}$ . For each image, after finding the proper seeing value and the corresponding slit profile, I record the maximum reflectance value  $Ref_{max}$  read from the latter in order to use it in the calibration equations.

For the calibration, as we said before, the planet itself will be used as a standard candle, for that we need to know the brightness of the planet in the region of the sodium D2 line at wavelength 5890 Å°. What we have is the brightness at 1 AU , we use equation 3.4 to find the brightness at the heliocentric distance at the time of the observation (table 3.2):

$$F_{mercury} = F \times \frac{(1AU)^2}{R^2} \quad (3.4)$$

Where  $R$  is the orbital distance of Mercury in AU and  $F = 5.556 \times 10^4$  photons  $\text{cm}^{-2}\text{s}^{-1}\text{A}^{-1}$  the solar flux in the continuum near the D2 line at 1 AU.

The reflectance from the surface computed from the blurred Hapke model is divided by  $\pi$  to obtain the bidirectional reflectance  $\mu$ .

To obtain the calibration factor **calfac**, the bidirectional reflectance is multiplied by the solar flux at Mercury (eq.3.4) at the time of the observation, and by the pixel dispersion  $D = 1.46 \text{ mA}^\circ/\text{pixel}$ , and finally divided by the maximum counts per pixel  $C$  in the observed continuum near the D2 emission line, the calibration factor can therefore be expressed as (Killen et al. 1999):

$$\text{calfac} = 4\pi \frac{\mu FD}{R^2} \times \frac{1}{C} \quad (3.5)$$

The integrated sodium emission intensities are then multiplied by the calibration factor, eq.3.5 to obtain them in kR:

$$I(\text{Na})_{kR} = \text{calfac} I(\text{Na})_{\text{ADU}} \quad (3.6)$$

The calibration factors and the different parameters used in equation 3.5 for each image of data September 29 and September 30 are listed in tables 3.8 and 3.9. Images 30 and 31 of Sepember 29 and images of September 28 data did not have guider images so the seeing could not be estimated for those.

Table 3.8. Calibration factors for the data of September 29, 2009.

Image	C(ADU)	R (AU)	$Ref_{max}$	$\mu$	calfac
Image23	94.5	0.3	0.008	0.03	0.2
Image24	79.0	0.3	0.007	0.002	0.3
Image25	79.0	0.3	0.005	0.02	0.2
Image29	96.0	0.3	0.004	0.001	0.1

Table 3.9. Calibration factors for the data of September 30, 2009.

Image	C(ADU)	R (AU)	$Ref_{max}$	$\mu$	calfac
Image11	12.8	0.3	0.002	0.0007	0.6
Image12	14.7	0.3	0.002	0.0007	0.5
Image13	19.5	0.3	0.002	0.0007	0.4
Image14	17.9	0.3	0.002	0.0007	0.4
Image15	18.2	0.3	0.003	0.001	0.6
Image28	11.8	0.3	0.01	0.003	3.6
Image29	8.6	0.3	0.01	0.003	4.2

# CHAPTER 4

## Scripting

### 4.1 Motivation

All the data reduction procedures that I explained earlier are done with IRAF, and as I have many observation sets with a large number of data images on which I have to perform the same set of data manipulations. I figured it is more efficient if I write the data reduction commands into a CL script and apply them directly to the data.

Moreover, after obtaining flatfielded, sky subtracted Mercury images, I have to extract the sodium lines in different positions along the slit in order to measure their integrated line fluxes and form color maps of sodium emission that will allow us to study the variability of Sodium emission with position and time.

Because of the Sun-Mercury relative velocity, the sodium Fraunhofer absorption line in sunlight reflected from Mercury were Doppler-shifted by a certain amount from the sodium emission line, see Figure 3.22. What I want to do, is to subtract this line profile (the sodium Fraunhofer absorption line) from the spectrum of each Mercury image, in order to finally obtain the emission from the planet only (the sodium emission line).

Usually, the Fraunhofer line is fit with a voigt profile and subtracted from the original spectra, and with IRAF, this procedure is a little tricky and has to be done interactively. But for our data I cannot apply this method because of the following reasons:

- I have 3 data sets, and in each one I have an average of 6 Mercury images, and from each image I have to extract around 300 pixel spectra, so extracting the emission line has to be done *non-interactively* with the use of a script.
- The Na emission line and the solar Fraunhofer absorption line are variable in intensity and shape throughout the slit, so fitting a voigt profile interactively will take a lot of time and effort.

For these reasons, I came up with a new routine to subtract the absorption line and extract the sodium emission line using the IRAF scripting language, the following sections explain in details my method.

## 4.2 IRAF scripting

As I said earlier, IRAF scripts are used to repeatedly perform a set of manipulations on any number of images, or to control the execution of any related set of tasks (Seaman 1989). There are three ways to produce an IRAF script.

First, the simplest way to produce an IRAF script is by the use of the task **mkscript** in the **system** package that allows us to create a script without using an editor and without knowing about syntax, and it contains any number of commands to be executed sequentially. Using this task is useful if we are interested in performing the same task on several data with only minor changes to the task parameters. After typing **mkscript** on the xterm window, we are asked for the name of the new script we want to create, it then enters **eparam** for the task where we edit all the *known* paramters for this task. After exiting the parameter editor, **mkscript** formats the command and places it in the script file after giving us the chance to verify that the command is correct. The script is submitted for execution with the following command:

```
> cl < scriptname.cl &
```

This mode of scripting in IRAF is called **Command mode** which is the default mode and is convenient for interactive use because it minimizes the need for commands delimiters, quoted characters strings and the special handling of file names like in the **Program mode**.

The second way to create scripts is with the use of a CL script. A CL script is a file containing the commands we wish to execute, both **command** and **program** modes are used in this type of script.

#### 4.2.1 The basic reductions

The first CL script that I applied to the data is called `reduction.cl` (Appendix B), this script executes the following tasks by order:

1. Registration of lines and columns of the images.
2. Trimming the useful data from the CCD chip.
3. Create the Master Zero frame.
4. Subtract the Master Zero from Mercury images.
5. Subtract the Master Zero from the Flat images.
6. Remove cosmic Rays from Mercury images.
7. Remove cosmic rays from the Flat images.
8. Create the Master Flat frame.
9. Normalize the Master Flat.
10. Flatfield the Mercury images.
11. Trim the sky part from Mercury images.

12. Form sky templates for Mercury images.
13. Subtract the sky from the Mercury images.

### 4.2.2 Extraction of Sodium lines

#### SCOPY

The process of sodium extraction was done using a number of scripts written in both IRAF and Python programing languages.

After I flatfield the data, and correct them for the non-uniform illumination of the slit, and sky-subtract them as I described before, I use the task **blkavg** to block-average every two pixels, and then I use the task **scopy** in order to extract the one dimensional spectral profile from the averaged pixels, specifying the direction of the dispersion axis by setting the parameter *DISPAXIS* in the image header to "2" (along the vertical dimension), and the *format* parameter of the task to "onedspec". The task **scopy** does the same job as the task **apall** for extracting the spectrum of point sources, these commands are written in a second CL script called **blkavg.cl**.

After extracting the spectrum from each pixel (which will be looking like Figure 3.22), I do the following:

1. Fit the sodium emission line blended with the Fraunhofer absorption line.
2. Subtract the fit from the initial spectrum to be left with the Fraunhofer absorption line.
3. Subtract this Fraunhofer absorption line from the initial spectra to obtain only the fitted sodium emission line.

#### S P L O T

In order to fit the sodium line properly we need to do it using the task **lomgslit.onedspec.splot** which is a powerful interactive facility used to display and analyse spectra. By typing:

```
>splot spectra.fits
```

A graph window will show up and an interactive cursor loop is entered. The cursor loop takes single keystroke commands, a summary of these commands can be displayed with the '?' key. The key that I have to use in order to fit the sodium line profile is 'k'. The latter key marks two continuum points and fit a single Gaussian line profile. These two points are specified by simply putting the cursor on the desired locations and hitting 'k' at every position. The center, continuum at the center, core intensity, integrated flux, equivalent width, sigma and FWHM are printed on the graph window and saved in a log file.

After fitting the sodium line profile with the key 'k', I remark the two positions but this time I use the key '-' in order to subtract the fitted sodium emission line. After that I use the key 'f' in order to subtract this resultant Fraunhofer line from the original spectra. The key 'f' is usually used to enter arithmetic function mode, it allows arithmetic functions to be applied to the spectrum, I then use -in function mode- the keystroke '-' in order to subtract another spectrum, the window will prompt me for the name of the other spectrum that I want to subtract from the Fraunhofer absorption line profile, I enter the name of the initial spectrum and hit 'Enter', of course the resultant emission line will be directed downward (because we subtracted the initial spectrum from the Fraunhofer absorption line), so I use -still in function mode- the keystroke 'm' in order to multiply the final spectrum by  $-1$  and obtain the sodium emission line, as a last step, I have to save the resultant sodium emission line, for that I use the keystroke 'i' and write the name of the new saved spectra.

Figure 4.1 illustrates the process of extraction for a spectrum where the solar reflection was weak (away from the surface of the planet), and Figure 4.2 for a spectrum where it was significant (close to the surface). Of course applying all these steps will take a long time if I want to do it interactively for all the spectra I have, so I thought it's easier to do it non-interactively using a *cursor file* in which I can submit all the above interactive cursor commands to the task **splot** in my CL script and obtain the

desired results.

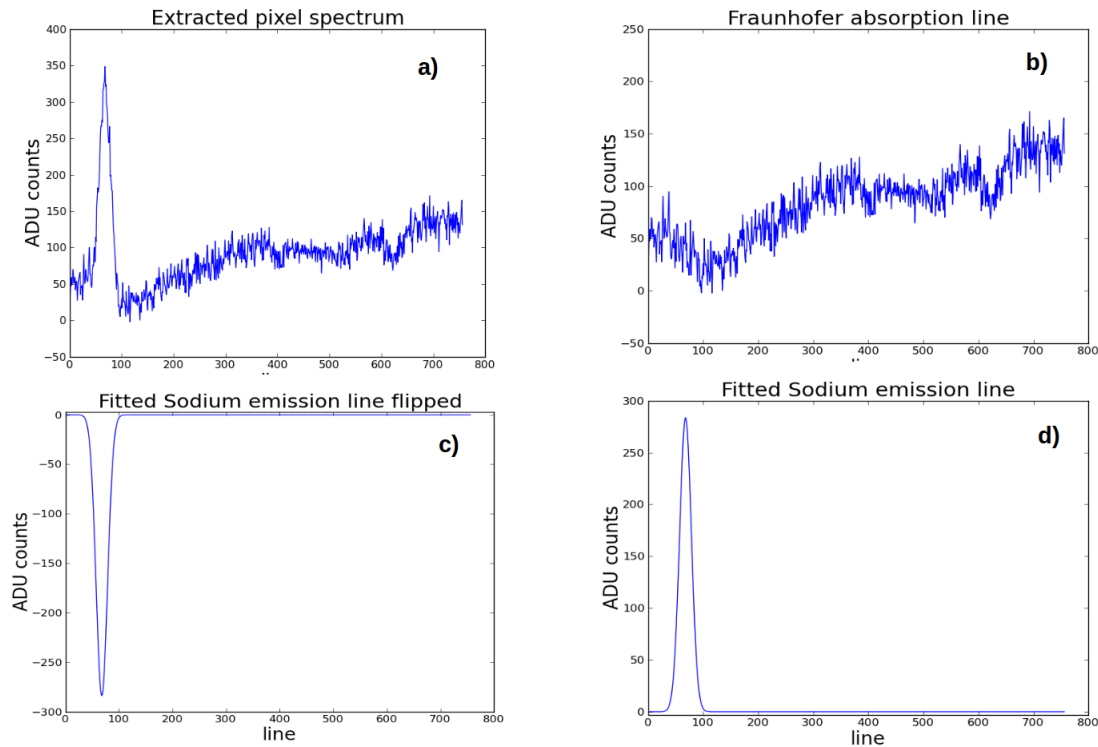


Figure 4.1: The main steps for Sodium line extraction: a)The initial extracted spectrum from a pixel along the slit, b)The reflected Fraunhofer line after fitting and subtracting the sodium line, c)the initial spectrum (a) subtracted from the Fraunhofer line (b), d)the flipped sodium emission line (c) multiplied by -1.

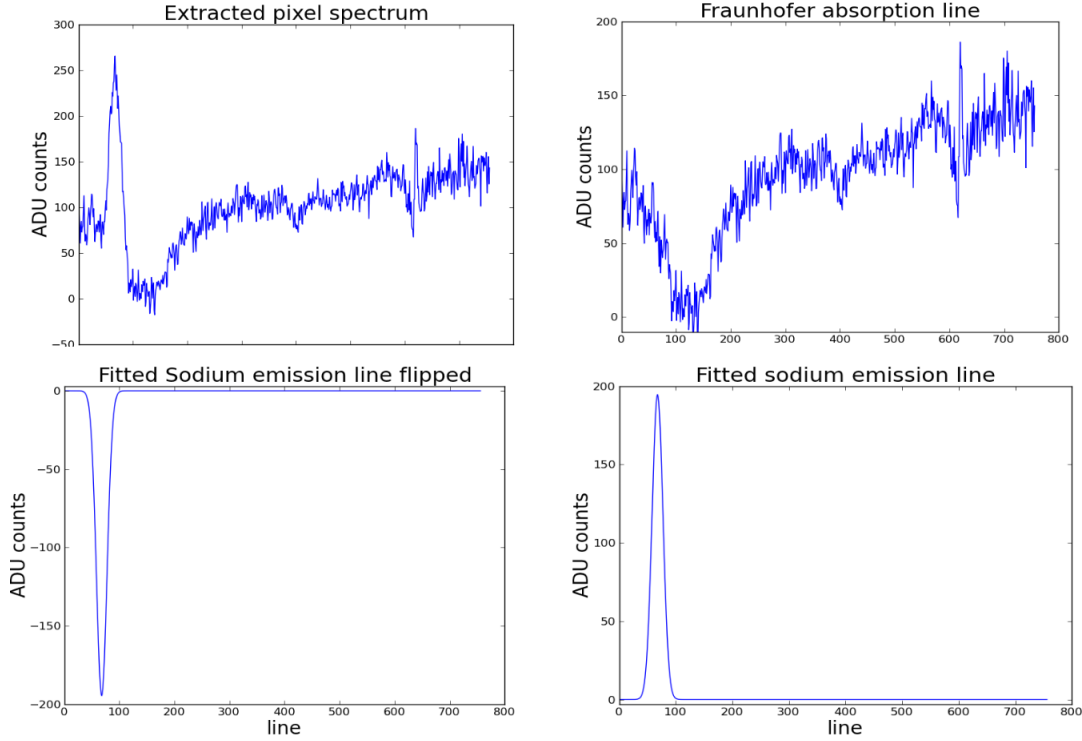


Figure 4.2: The main steps for Sodium line extraction: a)The initial extracted spectrum from a pixel along the slit, b)The reflected Fraunhofer line after fitting and subtracting the sodium line, c)the initial spectrum (a) subtracted from the Fraunhofer line (b), d)the flipped sodium emission line (c) multiplied by -1.

## Cursor Files

A cursor file is normal text file where every line is a cursor command of the following form:

*x* *y* *1* *command*

Where *x* and *y* are the cursor positions (the pixel and count values) in world coordinates, and *command* is the cursor command to be executed ('k' or 'f' or 'm' or '-'). So in short, my cursor file will look something like 4.1.

Where  $x_1, y_1$  are the position of the first marked point, and  $x_2, y_2$  the position of the second one, as shown in Figure 4.3.

Table 4.1: The sodium line extraction cursor file

$x_1$	$y_1$	1	k	(1)
$x_2$	$y_2$	1	k	(2)
$x_1$	$y_1$	1	-	(3)
$x_2$	$y_2$	1	-	(4)
0	0	1	c	(5)
0	0	1	f	(6)
0	0	1	-	(7)
0	0	1	m	(8)
0	0	1	q	(9)
0	0	1	i	(10)
0	0	1	q	(11)

Lines (1) and (2) mark the two positions of the sodium line and fit it with a Gaussian profile.

Lines (3) and (4) mark the same two positions to subtract the fit.

Line (5) redraw the resultant spectrum (the Fraunhofer absorption line).

Line (6) enters the function mode.

Line (7) subtracts the second spectrum (the initial one).

Line (8) multiplies the flipped sodium emission line by  $-1$ .

Line (9) quit the function mode.

Line (10) save the new spectrum (the sodium emission line).

Line (11) quit the graph window.

The names of the second subtracted spectrum and the new spectrum are passed to the task **splot** inside the cl script using the CL scripting syntaxe. The hardest part in generating the cursor files is the best estimation for the cursor positions  $(x_1, y_1)$  and  $(x_2, y_2)$  used to fit the sodium emission that is blended within the Franuhofer absorption line, the choice of these two positions has to be done in a way to minimize the loss of any flux information from the sodium emission line.

$x_1$  and  $x_2$  are chosen by interactively checking some spectra for the best fit, then entered in my code as constants for all pixel spectra along the slit, as for  $y_1$  and  $y_2$ ,

I had to use the package **PyFITS**<sup>1</sup> in Python in order to make my script read the count values corresponding to the two positions  $x_1$  and  $x_2$ , and since the spectrum usually shows a lot of spikes, the script calculates an average of count values at each position  $x_1$  and  $x_2$  and return them as  $y_1$  and  $y_2$ . In addition, in some spectra this averaged count has to be lowered by some pixels for the best fit of the sodium line, see Figure 4.3 for a better illustration.

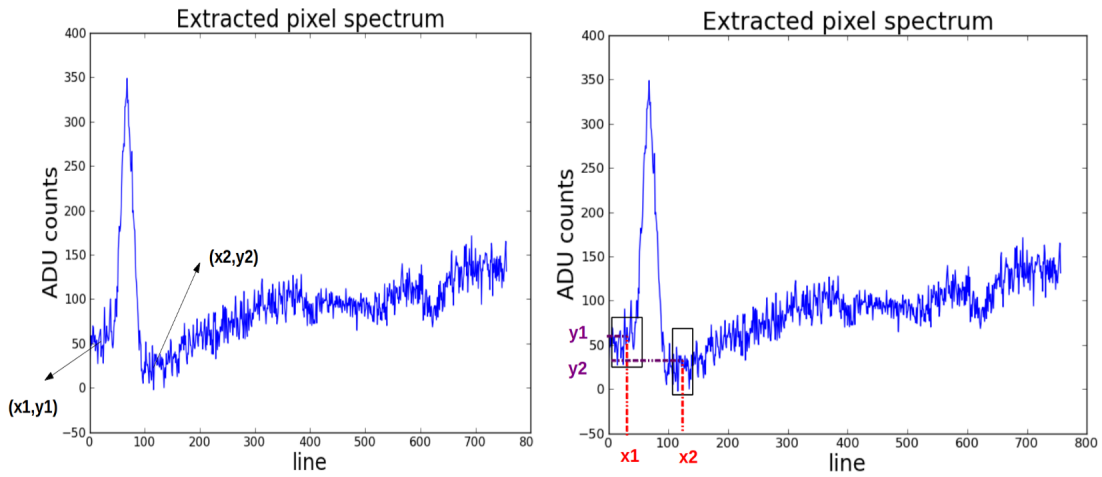


Figure 4.3: The coordinates of the two cursor points delimeters of the fitted sodium emission line,  $x_1$  and  $x_2$  are fixed for all pixel spectra, and  $y_1$  and  $y_2$  are calculated by the script averaging the counts corresponding to all the  $x$ 's around  $x_1$  and  $x_2$  (the regions indicated by the boxes).

### 4.2.3 SCRIPTS

The steps described before are executed by running the following scripts (by order), first we begin by the raw data and apply the following script:

#### 1. `reduction.cl`:

This CL script applies the basic data reduction procedures as explained in

---

<sup>1</sup>[http://www.stsci.edu/institute/software\\_hardware/pyfits/](http://www.stsci.edu/institute/software_hardware/pyfits/)

section 4.2.1, and covered in section 3.3.2.

After obtaining the sky-subtracted images (the output of `reduction.cl`), we perform the corrections on the flatfielded images to account for the non-uniform illumination of the slit as explained in section 3.4, and then subtract the new corrected sky to obtain the new corrected sky-subtracted images. After that, the next IRAF script is applied to these corrected images in order extract their sodium emission lines.

#### 2. `blkavg.cl`:

This CL script reads each sky-subtracted image, and use `blkavg` to average the spectra of two consecutive pixels, covering only the region along the slit where the sodium emission is present, this region may differ from image to image, but it's possible to enter in the script the delimiters of this region as input parameters. And then use `scopy` to extract a 1D spectra from the averaged pixels.

#### 3. `sodium_cursor.py`:

This python script is written to generate a cursor file in the form of 4.1 for each 1D spectrum (output of `blkavg.cl`) . For each spectrum, it reads the count values  $y_1$  and  $y_2$  as explained in section 4.2.2 at  $x_1$  and  $x_2$ , and write the results for each spectrum into a corresponding textfile which will be the *cursor file* used in the next script, the input parameters for this script are: the number of extracted spectra,  $x_1$  and  $x_2$ .

#### 4. `splot.cl`:

After generating the cursor files for each spectrum, this IRAF script is run on all the extracted spectra in order to submit the cursor commands of the cursor files to the task `splot`. The plots corresponding to the execution of the cursor commands in the cursor files are saved in a *metacode file* using the standard

redirection symbol `>` followed by the token `G`, these plots are displayed by IRAF using the task `gkimosaic`, looking like Figures 4.1 and 4.2.

#### 5. `flux_cursor.py`:

After the extraction of all sodium lines at each pixel, I have to read their integrated fluxes (in ADU units) using `splot` again, and in order to do that, I have to generate again a cursor file for each line containing this time commands to read the integrated line fluxes, the output cursor file will have this form:

$x_1$	$y_1$	1	k
$x_2$	$y_2$	1	k
0	0	1	q

This python script reads the new count values  $y_1$  and  $y_2$  at the positions  $x_1$  and  $x_2$  of the extracted sodium lines, and write the results into textfiles that will be used in the next script as the *cursor files*.

#### 6. `flux.cl`:

After generating the cursor files from the previous script, the cursor commands of these cursor files are submitted to the task `splot`, the latter will fit the extracted sodium lines and read their integrated line fluxes and then save the values into a log file for each spectrum.

#### 7. `colormap_1.py`:

Each log file, output of `flux.cl` corresponds to one extracted spectrum and contains all the parameters returned by `splot` after using the key '`k`' to fit the sodium line: The center, continuum at the center, core intensity, integrated flux, equivalent width, sigma and FWHM. This python code will read each textfile, and then read the lines in order to extract the forth parameter 'integrated flux', the values extracted from all the textfiles are saved in a new list '`data.lis`',

#### 8. `colormap_2.py`:

This code consists of several parts, the first part will read '`data.lis`' and generate

a new list 'newdata' which consists of replicated data values, since each value in 'data.lis' corresponds to the average count of each two pixels. The second part will generate a third list 'final.lis' that has the dimension of the slit and attributing to the rest of the pixels a count of 0 (because there is no sodium emission there), the last part will read the final list and make a colored map of sodium emission (Chapter 5) after multiplying the ADU counts for each image by its corresponding calibration factor to obtain intensities in kR.

#### 9. continuum.py:

This python code is written in order to extract the continuum (solar reflection) counts from the extracted spectra along the slit. The code reads with **pyfits** the spectra along the slit, and takes from each the average counts of the first 10 data points (the continuum part) as shown in Figure 4.4, the values are written into a textfile to be calibrated and plotted (Chapter 5).

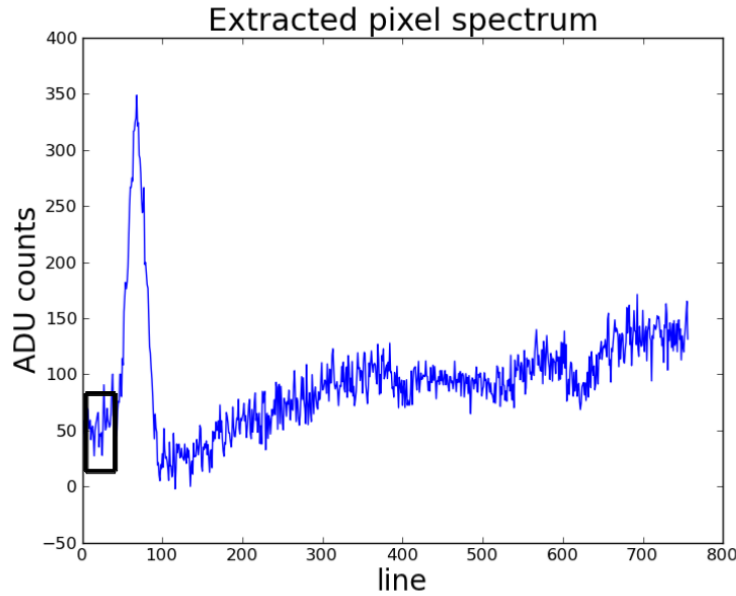


Figure 4.4: The region in the box is what the code will average to extract the continuum value.

# CHAPTER 5

## Results and Analysis

### 5.1 Sodium Emission Maps

After extracting the sodium emission lines and calibrating their fluxes, I wrote a Python code that generates colored maps of sodium emission along the slit in order to illustrate the apparent variability seen over the different regions of the planet during the days of observations.

The output of the code looks like Figure 5.1, where the sodium emission along the slit (in pixels) is shown, the length and width of the slit are the input of this code, so they can be modified accordingly.

Sodium Intensity map, SEPTEMBER 29, UT 15:41

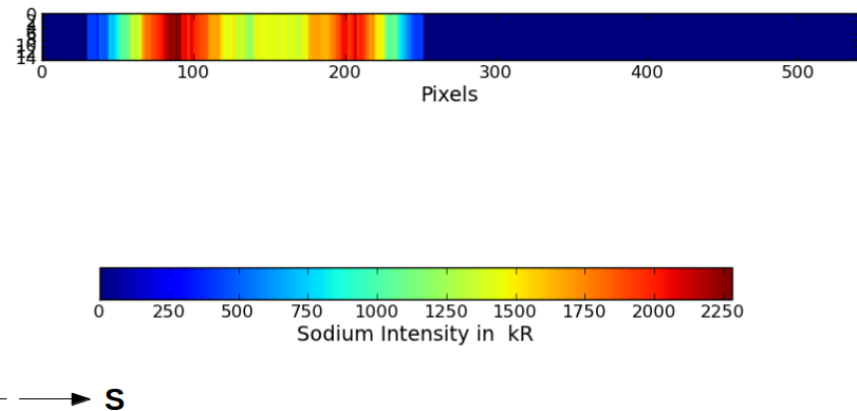


Figure 5.1: Sodium emission colored map showing the distribution of exospheric sodium intensities in kR along the slit(pixels). The slit is oriented along the North-South direction and positioned on the terminator.

The next step is to overplot these maps on the surface of the planet generated by the Hapke model, the diameter of the planet ( $8.6''$ ) according to the model corresponds to 86 pixels, so the resolution of the Hapke generated surface is  $0.1''/\text{pixel}$ , in order to plot the slit map (Figure 5.1) on the surface, the length and width of the slit should be modified accordingly, respecting the resolution of the Hapke model. These numbers are entered as input to my plotting code, and figures showing the slit overlaid on the surface are generated for the different images in our observation sets:

### Sodium Emission Maps, SEPTEMBER 29, 2009

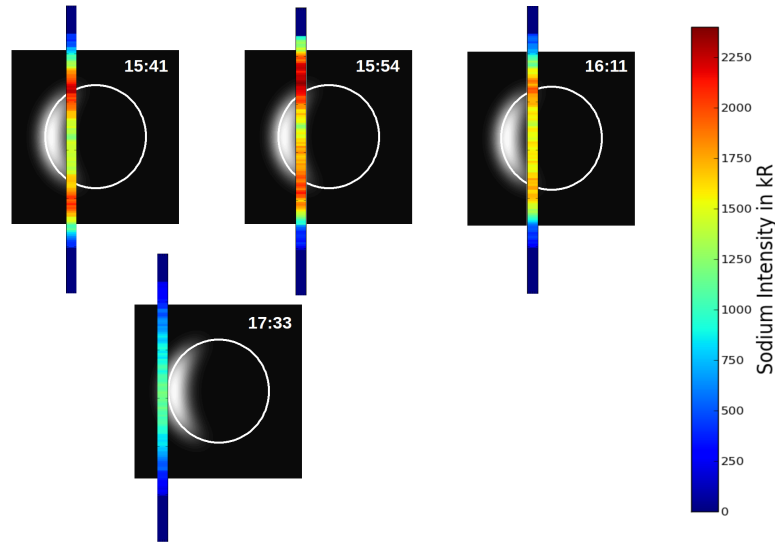


Figure 5.2: Sodium Emission Maps, September 29, 2009, the slit  $30'' \times 1.2''$  was used.

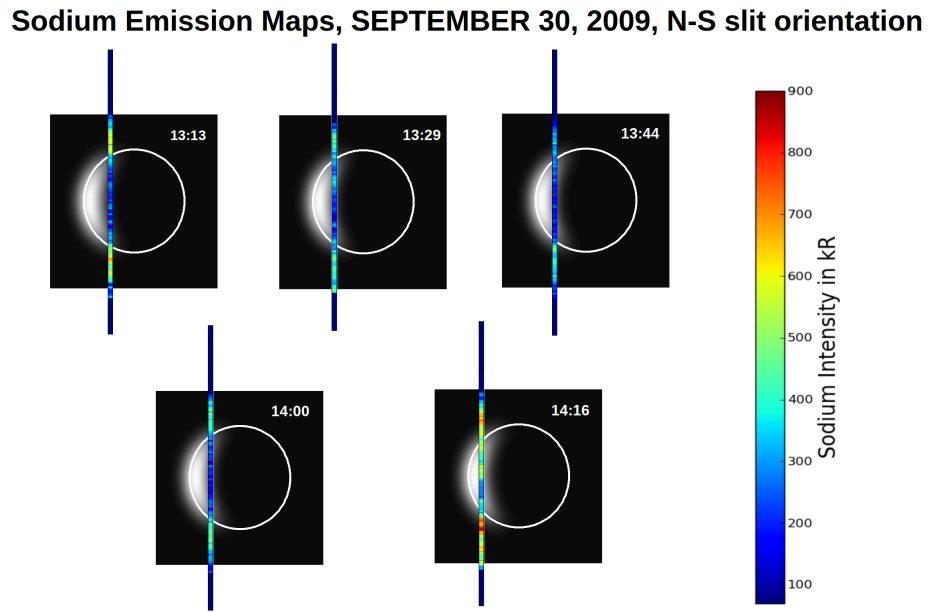


Figure 5.3: Sodium Emission Maps, September 30, 2009 (North-South slit orientation), the slit  $30'' \times 0.2''$  was used.

**Sodium Emission Maps, SEPTEMBER 30, 2009**  
**T-L slit orientation**

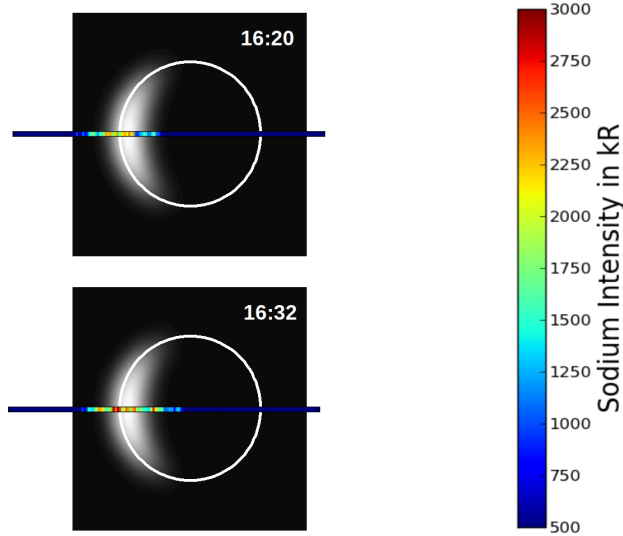


Figure 5.4: Sodium Emission Maps, September 30, 2009 (terminator-limb slit orientation), the slit  $30'' \times 0.2''$  was used.

## 5.2 Asymmetries in Emission intensities

To better visualize the distribution of sodium across the planet, I wrote a code that generates plots of the exospheric sodium emission (in kR) against arcseconds. The plots show the distributions and spatiotemporal variation of sodium intensities across the planet for different orientations of the slit, as well as the distribution of the solar reflection intensity extracted from the spectra (see the code `continuum.py` in section 4.2.3).

The first step in plotting and analysing our results is to find a center for each data image in order to define the northern, southern, eastern and western hemispheres. This point was determined from the surface reflection profile, locating the pixel with maximum (or minimum) signal, this point will then correspond to the center of the

image ( $0''$ ), the exospheric sodium emission are then plotted from the center of the image, using the data's plate scale ( $0.056''/\text{pixel}$ ), and converting pixels into arcseconds. The results for September 29 data (Figures 5.5 and 5.6), and for September 30 data (Figures 5.7 to 5.9) are plotted. For noisy signals (surface reflection and some noisy sodium emission profiles) I used the *Savitzk-Golay* filter in order to smooth the plots, this is achieved by fitting successive sub-sets of adjacent data points with a low-degree polynomial by the method of linear least squares.

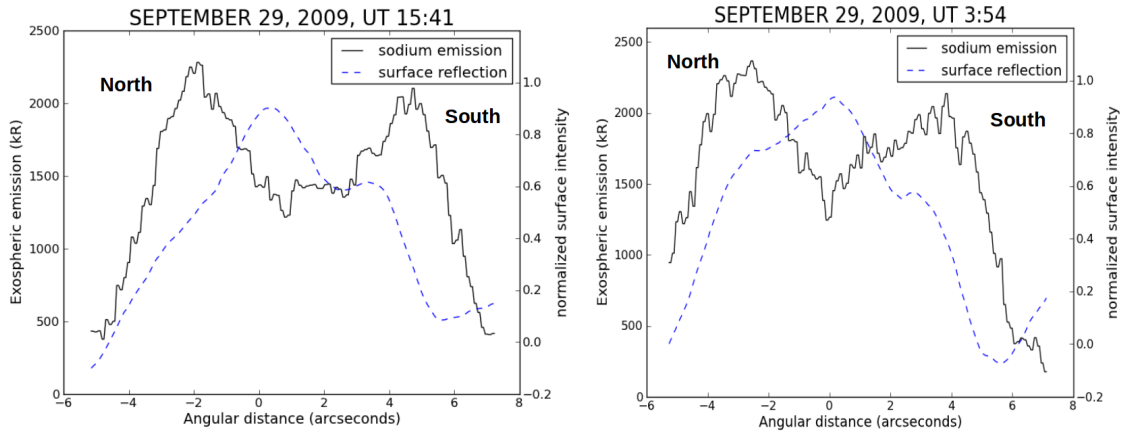


Figure 5.5: A north-south profile of sodium emission on Mercury on September 29, the slit was positioned on the Terminator. The figures show the emission intensity for sodium D2 emission plus the normalized intensity of sunlight reflected from the surface.

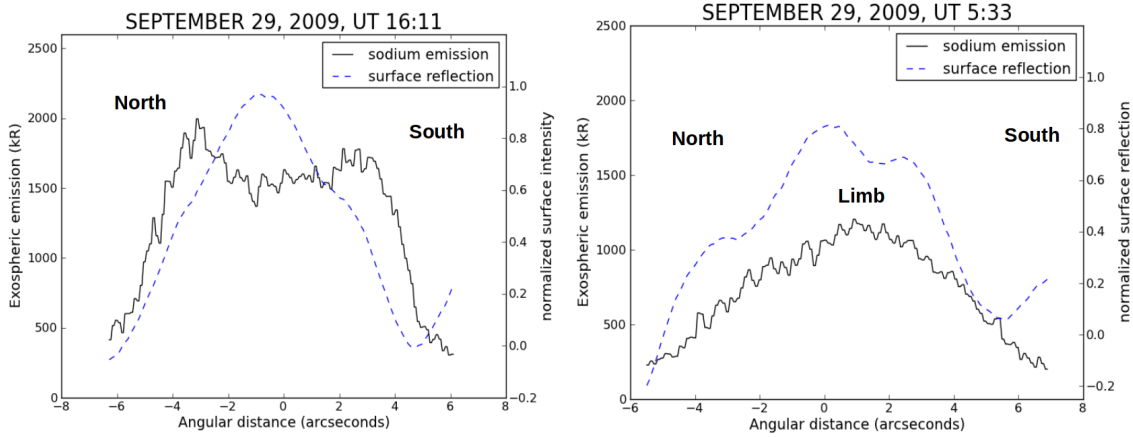


Figure 5.6: A north-south profile of sodium emission on Mercury on September 29, the slit was positioned on the Terminator(left panel) and on the limb(right panel). The figures show the emission intensity for sodium D2 emission plus the normalized intensity of sunlight reflected from the surface.

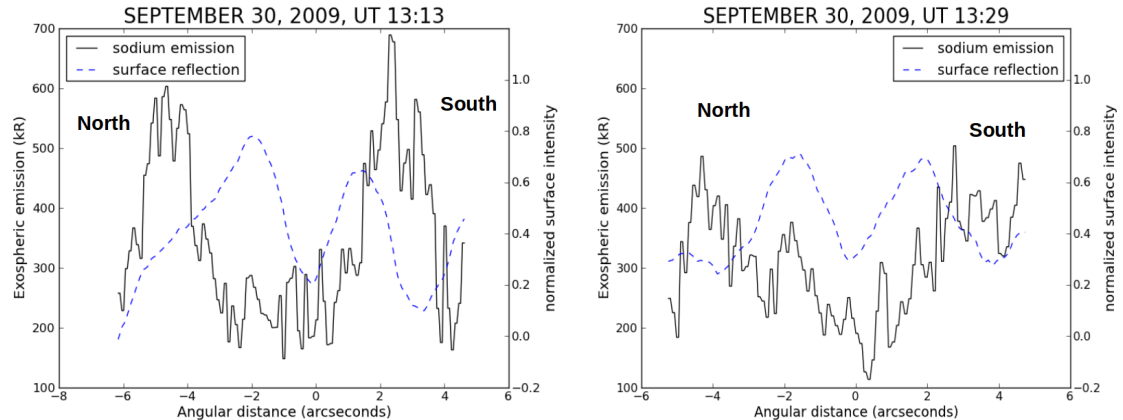


Figure 5.7: A north-south profile of sodium emission on Mercury on September 30, the slit was positioned on the Terminator. The figures show the emission intensity for sodium D2 emission plus the normalized intensity of sunlight reflected from the surface.

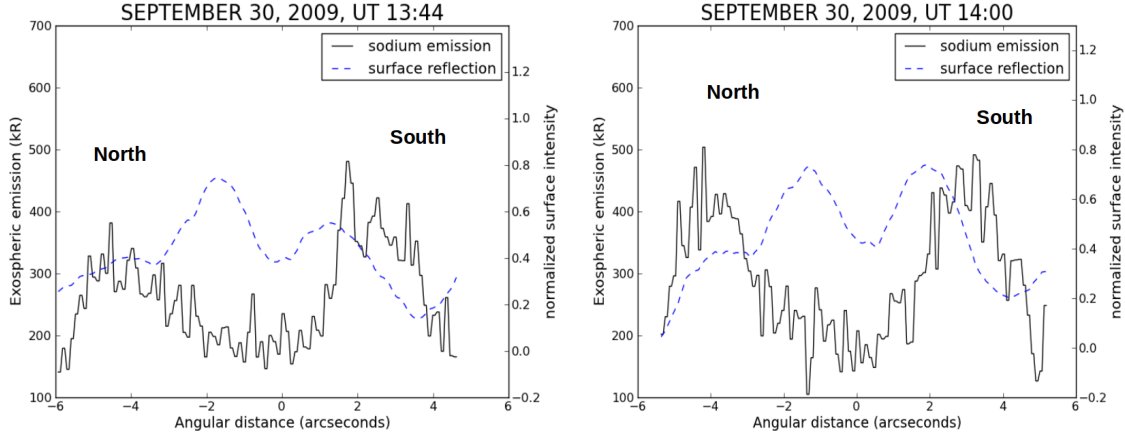


Figure 5.8: A north-south profile of sodium emission on Mercury on September 30, the slit was positioned on the Terminator. The figures show the emission intensity for sodium D2 emission plus the normalized intensity of sunlight reflected from the surface.

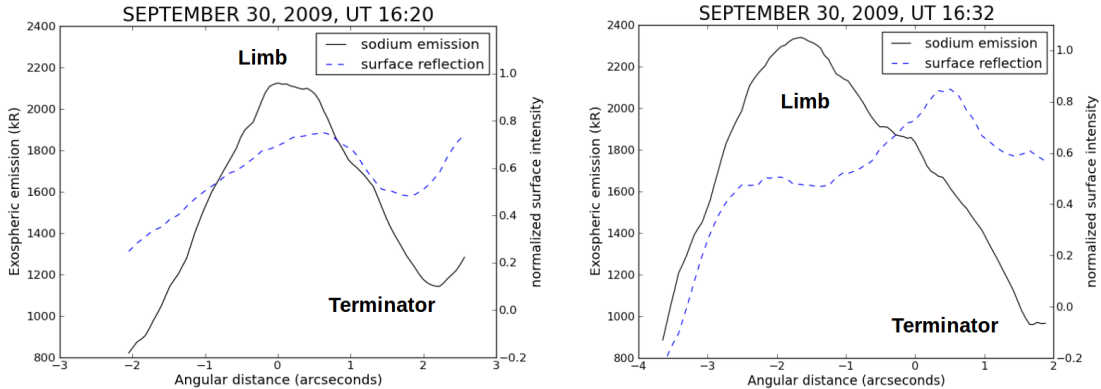


Figure 5.9: A terminator-limb profile of sodium emission on Mercury on September 30, the slit was positioned along the equator. The figures show the emission intensity for sodium D2 emission plus the normalized intensity of sunlight reflected from the surface.

### 5.3 Discussion

We compare our results with results described in Potter et al. (2006), where they measured the north-south and east-west distribution of sodium across the planet during 1985-1987 using a slit spectrograph. After applying the appropriate corrections to their data, they have generated profiles for sodium distribution to show the north-south and terminator-limb asymmetries. Figure 5.10 illustrates their results where intensities are plotted against angular distance from the center of the planet, the dashed line represent the continuum and the solid lines are the D1 and D2 sodium emissions. In the two upper panels the scan was performed along the north-south direction, we can see an enhancement in the northern hemisphere in fig.b), while in fig.a) the emission is equal in both northern and southern hemispheres, implying a symmetric sodium distribution. The scan in the lower panels was performed along the terminator-limb line, fig.c) reports a clear increase in sodium intensity approaching the limb, while in fig.d) there is a decrease of 30% from limb to terminator.

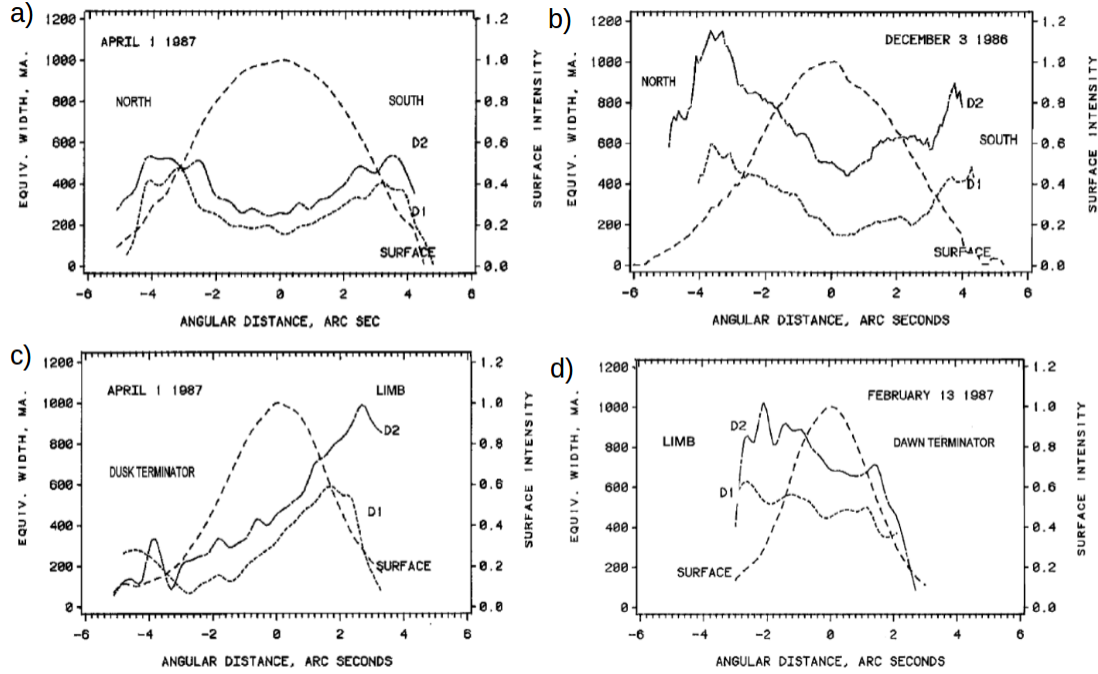


Figure 5.10: Profiles of exospheric sodium emission (solid lines) and surface reflection (dashed line) across the planet, Potter et al. (2006).

Examining our exospheric sodium profiles and maps, we can similarly notice the presence of such excess in sodium emission at high northern and southern altitudes. In addition, the data of September 29 shows an enhancement in Na D2 intensity in the northern hemisphere of the planet, the sodium profiles of figures 5.5 and 5.6, and the sodium emission maps (figure 5.2) show clearly the presence of such enhancement when the slit was along the north-south direction.

On the other hand, the data of September 30 also shows a sodium excess at high altitudes, and an enhancement, but this time in the southern hemisphere as can be shown in the sodium emission maps and profiles where the slit was along the north-south direction (figures 5.3, 5.7 and 5.8).

The appearance of excess sodium at high southern and northern altitudes is common in several works (Potter & Morgan 1990; Sprague 1992), this could be explained by the effect of sputtering by solar wind particles (see section 2.2). Since the surface of Mercury is at certain times open to the solar wind, the solar wind plasma particles can penetrate the surface through the cusp regions and sputter by momentum exchange the sodium atoms, leading to the excess of sodium emission seen at high latitude regions, the size and location of this excess depend on the strength and orientation of the Interplanetary Magnetic Field (IMF) when the  $B_x$  component is present. This effect was modeled by (Sarantos et al. 2001), showing that for a negative  $B_x$ , solar ions have velocity component parallel to Mercury's open magnetic field configuration in the northern hemisphere but antiparallel in the southern hemisphere which lead to an excess in the northern regions of the planet, and vice versa. As a result, the asymmetries seen for the sodium distribution might be due to asymmetric precipitation of solar wind particles.

A proper modelling of Mercury's interconnected open magnetosphere is needed to be compared with our results and qualitatively interpret the sodium emission seen in our data.

In the same paper, they extracted the intensities of sodium emission from their Na D2 exosphere observations during the period of 1997-2003 for different true anomaly angles, in the northern and southern hemispheres, and derived the north-to-south ratio as an indicator of the north-south asymmetry of sodium distribution, in addition to the terminator-to-limb ratio that indicated the degree of asymmetry of sodium emission in the limb and terminator. If the sodium distribution was perfectly symmetric, the emission intensity would show approximately equal maxima near both the north and south polar regions, and the north-south ratio would be equal to unity, for images with excess sodium emission in the southern hemisphere, the north-south ratio value would be less than unity, and for excess sodium in the northern hemisphere, the ratio would be greater than unity. For the terminator-limb ratio, images with

excess sodium emission on the limb, the ratio would be less than unity, and for excess emission on the terminator, the ratio would be greater than unity.

Figures 5.11 and 5.12 show their north-south and terminator-limb ratios respectively plotted as a function of true anomaly angle.

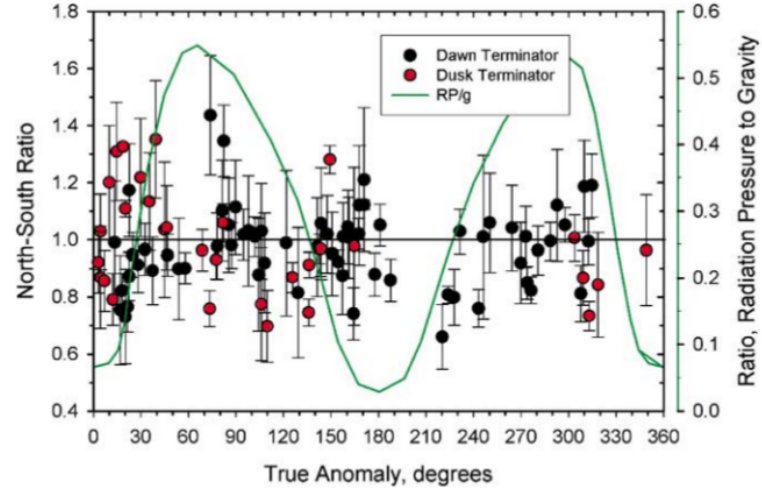


Figure 5.11: North-to-South ratios (left ordinates) against true anomaly angles. The green line is the solar radiation pressure, (Potter et al. 2006).

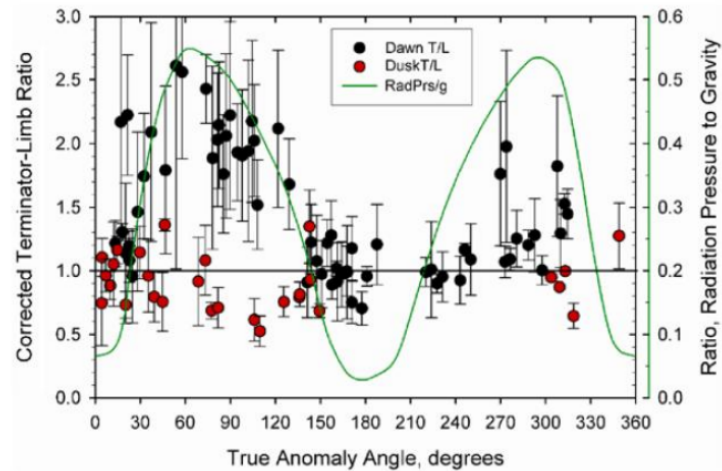


Figure 5.12: Terminator-to-Limb ratios (left ordinates) against true anomaly angles. The green line is the solar radiation pressure, (Potter et al. 2006).

The variations seen in the terminator-limb ratio was explained by (Potter et al. 2006) to be due to the effect of solar radiation acceleration, they are seen in figure 5.12 to be larger at  $TAA < 180^\circ$  (sodium is highly concentrated at the terminator) since the solar radiation acceleration has a bigger effect in this range , "blowing" more sodium atoms towards the terminator and increasing the T/L ratio, the latter decreases at  $TAA > 180^\circ$  as a result of the decrease in solar radiation acceleration.

Similarly, after assigning the center of each slit image of our data, the code generating the sodium distribution profiles averages the sodium intensities on either side of the center of the image, and the results are used to calculate the north-south or terminator-limb ratios. Table 5.1 shows the N/S and T/L ratios of data images from September 29 & 30, 2009 with the corresponding true anomaly angles, and figure 5.13 represents the variation of these ratios with true anomaly angle.

Table 5.1. N/S and T/L ratios for data of September 29 &amp; 30 2009.

Sep 29 data	TAA (degrees)	N/S	Sep 30 data	TAA (degrees)	N/S(T/L)
Image 23	326.5	1.1		331.9	0.9
	326.5	1.3		331.9	0.9
	326.6	1.1		332	0.8
	327.9	0.9		332.1	0.9
				332.2	1.01
				332.7	0.90(T/L)
				332.8	0.8(T/L)

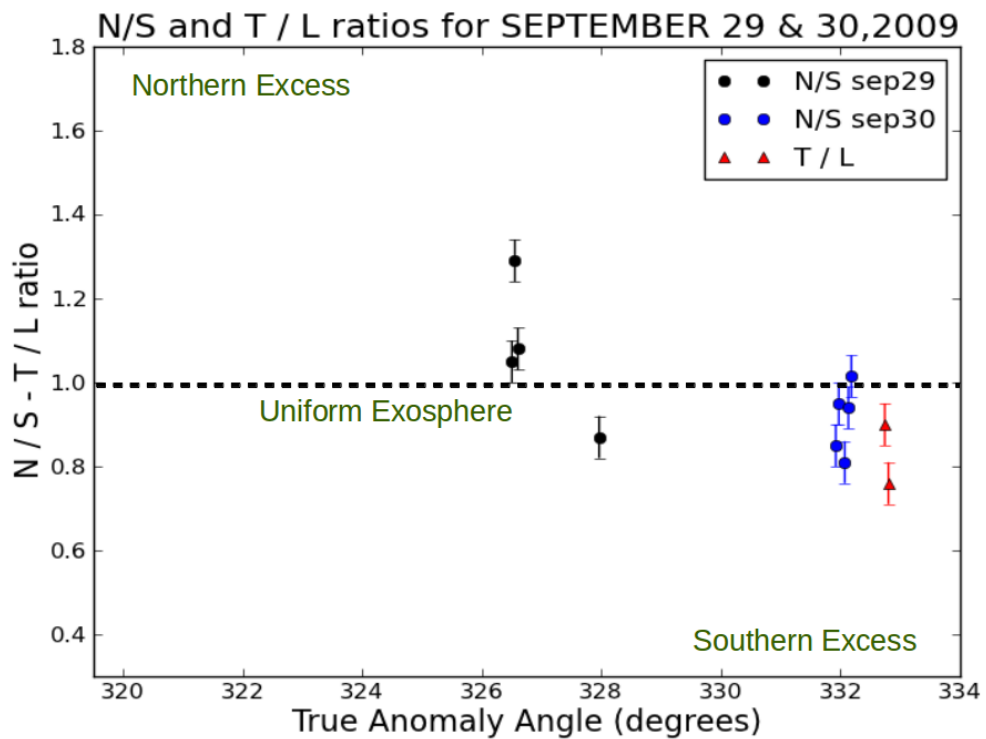


Figure 5.13: Variation of the north-to-south ratios for data of September 29 (black circles) and September 30(blue circles), and terminator-to-limb ratios (red triangles) with true anomaly angle. The dashed line corresponds to a uniform exosphere where the value of the ratio should be unity.

## N/S ratios

We can see clearly from the data points corresponding to N-S ratios, the distribution of excess sodium between north and south hemispheres does not show any correlation with true anomaly angle and therefore the solar radiation acceleration. Our results match Potter's as seen in figure 5.11.

## T/L ratios

These ratios are less than unity as shown in figure 5.13, which makes sense since Mercury was at  $\text{TAA} > 180^\circ$  and solar radiation pressure was minimum, leading to higher concentrations of Na on the limb of the planet.

## 5.4 From ground-based to space observations

In this section, we will present the space observations collected with MESSENGER probe, in order to compare with our ground-based observations.

### 5.4.1 MESSENGER observations

One main objective of the MESSENGER probe is to explore the nature of Mercury's exosphere. The Mercury Atmospheric and Surface Composition Spectrometer (MASCS) is one of the eight highly sensitive instruments on MESSENGER which helps in measuring the abundance of atmospheric gases around Mercury and detects minerals in its surface materials.

The Ultraviolet and Visible Spectrometer (UVVS) channel of MASCS instrument is designed specifically to observe atomic emission from neutral atoms like sodium, among other species.

MESSENGER has so far managed to make three flybys of Mercury, making spectroscopic studies of species in its exosphere and mapping their distribution over the

planet. MESSENGER's third flyby M3 on 29 September 2009 allowed UVVS/MASCS to map the tail region that extends anti-sunward from the planet. In addition to scanning the altitude distribution of different species including Na above Mercury's north and south poles, which had not been possible during the earlier flybys (M1 and M2) because of spacecraft-pointing constraints.

Sodium showed high enhancement in high latitude regions during both M1 and M2 flybys (figure 5.14), which is consistent with a scenario in which energetic sodium atoms are ejected from the surface by ion-sputtering at high latitudes (McClintock et.al 2009).

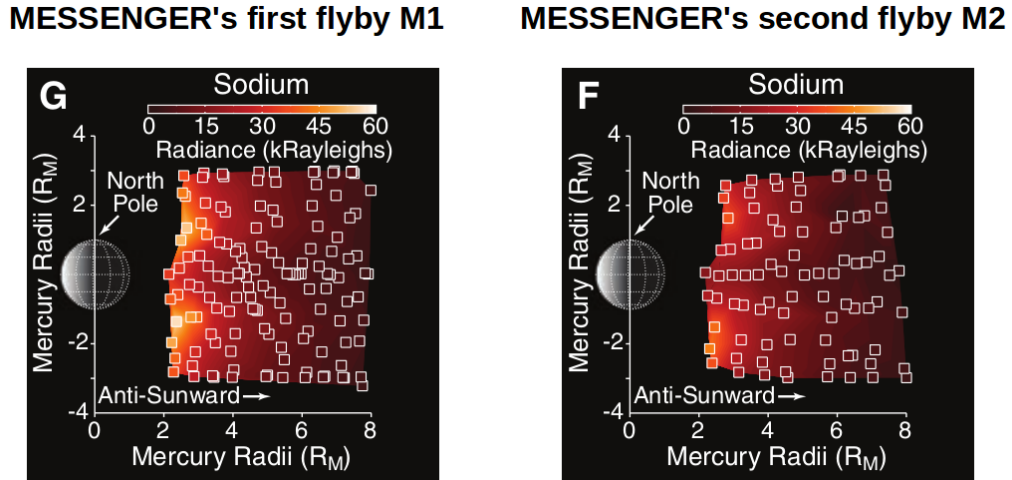


Figure 5.14: Sodium tail emission during M1 and M2. Sodium is peaking at high latitudes during both flybys, but it is relatively bright in the northern hemisphere during M1, while it's uniformly distributed during M2.

Moreover, during the first flyby M1 (14 January 2008), observations by the UVVS revealed a north-south asymmetry (25% brighter in the north) (McClintock et.al 2008), while sodium emission strengths were nearly equal to the north and south during M2, the reason for such variations is expected to be due to the solar wind activity, this is consistent with MESSENGER's magnetospheric observations, which suggests that solar wind plasma was directed toward higher northern latitudes during

M1 but more uniformly distributed during M2 (Salvin et al. 2008).

During the third flyby M3, observations of volatile Na showed also relatively high abundances over the north and south poles but with no significant north-south asymmetry. Exponential fits were made for MESSENGER data of sodium distribution above the poles (figure 5.15), yielding *e*-folding distances (which represent the altitude change required for exponentially varying intensities to drop by a factor of *e*) of 202 km (north) and 205 km (south) for altitudes less than 800 km, and 514 km (north) and 468 km (south) for altitudes greater than 900 km. These two components are consistent with a mix of low energy processes (such as photon simulated desorption), and high energy processes (such as ion-sputtering and meteoroid impact vaporization), (Vervack et al. 2010).

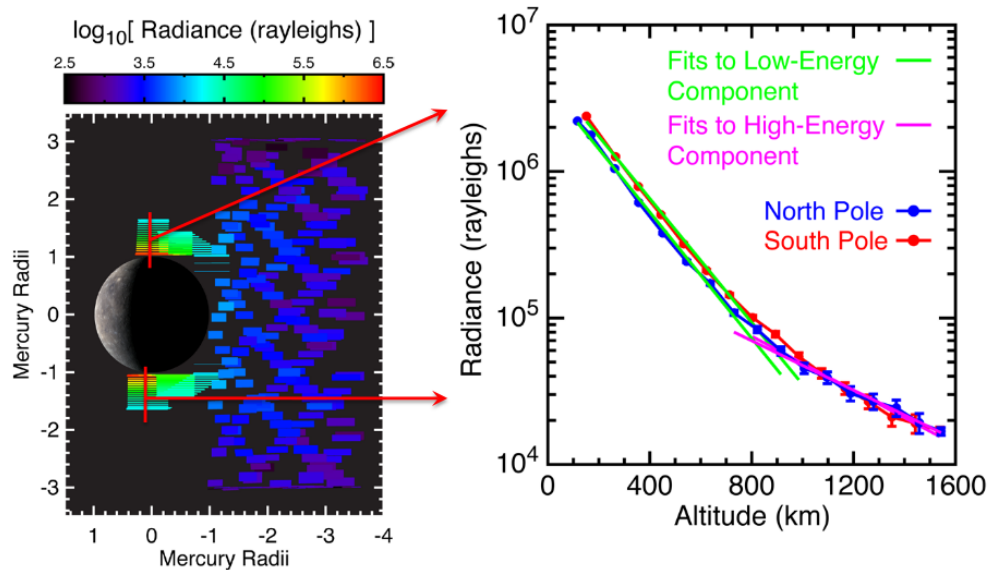


Figure 5.15: Sodium emission observed in the polar, nightside, and tail regions of Mercury during MESSENGER's third flyby(left), and Na emission profiles over Mercury's north and south poles(right).

### 5.4.2 MESSENGER & ground-based observations

As a new approach, we tried to plot the altitude distribution of sodium emission of our ground-based data, and compare them with the profiles measured by MESSENGER. For each image of the September 29 data where the slit was along the north-south direction, we plotted the Na intensities (kR) as a function of km, beginning from the northern and southern surface of the planet (0 km) (see fig. 5.16), after converting arcseconds into kilometers (the angular diameter of the planet 8.6" corresponds to the physical diameter of 4880 km). Figures 5.17 and A.2 show the latitude profiles above the northern and southern hemispheres from both MESSENGER and our longslit observations.

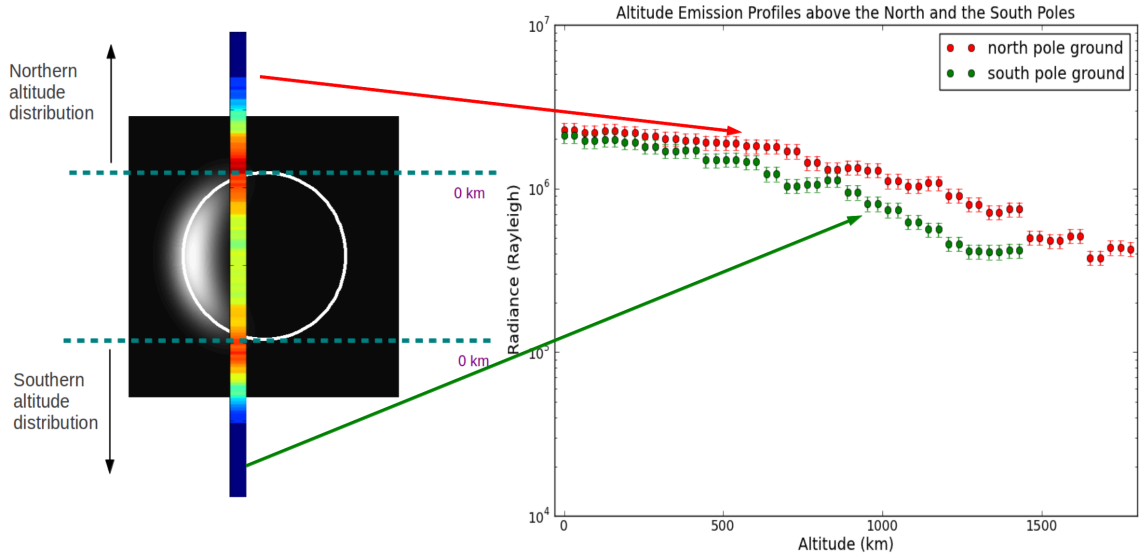


Figure 5.16: Plotting the Na southern and northern altitude profiles of our ground-based data, the north and south surfaces of the planet correspond to 0 km, the slit intensities are plotted from this point to map the southern and northern regions.

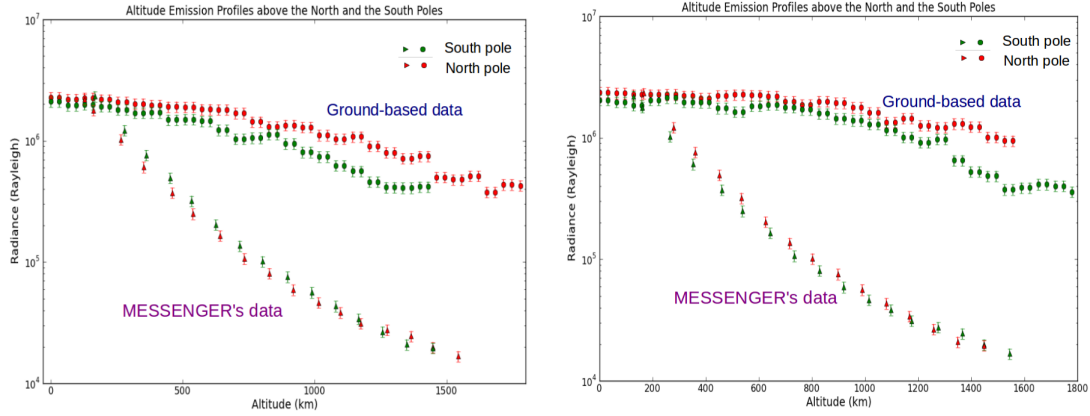


Figure 5.17: Sodium Emission profiles over Mercury's north and south poles of both MESSENGER and ground-based observations of the first and second exposures of September 29 data.

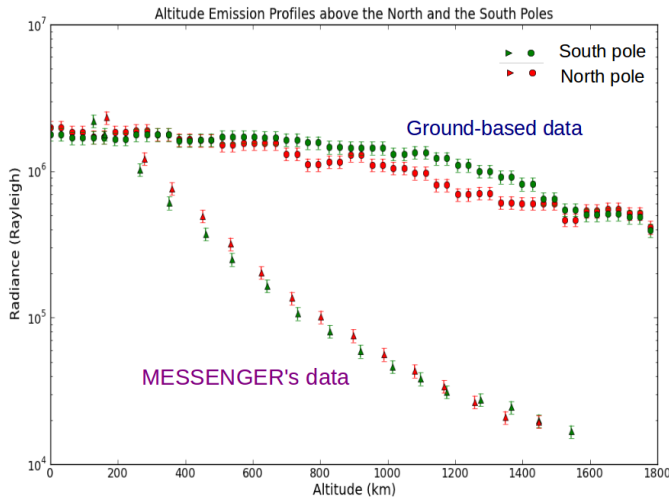


Figure 5.18: Sodium Emission profiles over Mercury's north and south poles of both MESSENGER and ground-based observations of the third exposure of September 29 data.

## Discussion

Our ground-based observations and space data collected by MESSENGER show a clear difference in the Na altitude profiles above the southern and northern poles. The space data are falling exponentially with altitude, but it's not the case for our ground-based observations. Different factors account for such discrepancy:

- Both observations do not result from the same observation geometry; our data were collected using a long slit and covering in this way the whole surface of the planet, while the UVVS obtained altitude scans **above** Mercury's north and south poles, and its line of sight was an arc perpendicular to the Sun-Mercury line (see fig. 5.19), so it's not a one-to-one comparison.

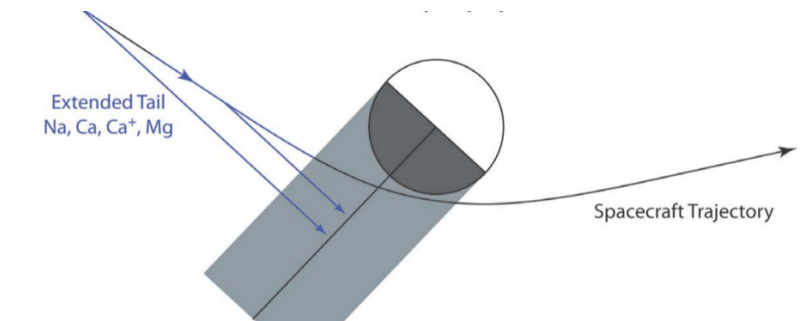


Figure 5.19: The geometry of MESSENGER's observations.

- Space observations will differ from ground-based observations, and especially when targeting an object like Mercury, the seeing due to the daylight observation could be causing the excess sodium intensities and their profile trends over the north and south poles. The next step that has to be done is to develop a model for the exosphere following a theoretical Chamberlain model of an exponentially falling exosphere, and convolve it with a seeing component to see to which degree the seeing is affecting our ground-based observations.
- Both observations were not simultaneous; there is a 2 to 4 hours difference between the two observation sets, so the exosphere's morphology might have

varied. However, it is unlikely that these differences in the profiles between space and ground-based data are due to spatiotemporal variations in the exosphere's morphology. The fact that the ground-based data always show similar profiles indicate that this might be an intrinsic feature of earth-based effects, possibly atmospheric seeing.

# CHAPTER 6

## Conclusions

For a complete understanding of Mercury's exosphere, we need to develop models for the distribution of sodium resulting from the different physical source ad loss processes described respectively in sections 2.2 and 2.3. And since the transport dynamics and spatial distributions of sodium are dependent on different parameters, a comprehensive simulation is needed to understand the variability seen for this exosphere. Modelling Mercury's sodium exosphere is based on tracking the motions of sodium atoms ejected from Mercury's surface by the different source processes, and whose trajectories are controlled by the gravity of the planet and radiation acceleration, taking into account several conditions: position of Mercury with respect to the Sun, the variation of solar radiation pressure, the photoionization lifetime of sodium atoms, the solar wind density, the meteoroid flux intensity, the surface temperature, as well as the interaction of the solar wind and the interplanetary magnetic field with the magnetic field of the planet.

And since the atmosphere is collisionless, sodium atoms produced by thermal desorption, solar wind ions sputtering and micrometeoroid vaporization can each be tracked separately. Column densities of exospheric Na are calculated, and the morphology of Na exosphere is generated over a specific timespan and under different conditions. The generated model is then compared to our observations to derive the mechanisms

and the conditions under which the exosphere of the planet was shaped during our observations, explaining the origin of the variations detected in the different regions of the planet.

The work of Mouawad et al. (2011) is an example of how modelling simultaneous ground-based and space data can better constraint the ones responsible for the observed Na exosphere. In their work, they have collected ground-based observations of Mercury's Na dayside exosphere during the first MESSENGER flyby of Mercury (M1), the data were then modeled along with the MASCS data from M1 which mapped the tail region of the planet. The models were then able to place a strong constraint on the photon-stimulated desorption (PSD) and impact vaporization process in shaping the observed exosphere.

## Future work

Additional work is needed to be done with our ground-based observations:

- The intensities  $I$  of Na emission in kilo-Rayleigh should be converted to column densities  $N$  expressed in  $atoms/cm^2$ , both quantities are linearly related through what's called the  $g$ -factor:

$$I(kR) = \frac{4\pi}{10^9} g N(atoms/cm^2) \quad (6.1)$$

The  $g$ -factor is the number of photons resonantly scattered per second by atom. This value depends on the quantum mechanical nature of the atom, and on

additional factors like the position of Mercury in its orbit and the amount of light available for the atoms to be scattered (Killen et al. 2009):

$$g(\lambda) = \frac{\pi\gamma F_{cont}}{R^2} \times \frac{\lambda^2}{c} \times \frac{\pi e^2}{mc} \times f \quad (6.2)$$

Where  $F_{cont}$  is the solar continuum near the D2 lines,  $R$  is the distance from the Sun to Mercury in AU,  $\lambda$  is the central wavelength after accounting for any Doppler shifting effects,  $e$  is the charge of an electron,  $m$  is the mass of an electron,  $f$  is the oscillator strength,  $\gamma$  is the fraction of the solar continuum "seen" by the atom, which depends on the TAA.

- Do the spectral analysis of the extracted Na lines along the slit to derive their doppler shifts and study their radial velocity distributions. Also the temperatures can be derived from the spectral lines to constrain source and loss processes.
- Do proper modelling of ground-based and space observations as stated above.

# Bibliography

- Anderson E., Seaman R., An Introductory User's Guide to IRAF Scripts, 1989.
- Bida T.A., Killen R.M. , Morgan T.H., *Nature* 404, 159-161, 2000.
- Broadfoot, A.L., Kumar, S., Belton, M.J.S., McElroy, M.B., Mercury's atmosphere from Mariner 10: Preliminary results. *Science* 185, 166-169, 1974.
- Broadfoot, A.L., Shemansky, D.E., Kumar, S., Mariner 10 - Mercury's atmosphere. *Geophys. Res. Lett.* 3, 57-580, 1976.
- Brown, R. A., and Y. L. Yung, Io, its atmosphere and optical emissions, in IAU Colloq. 30: Jupiter: Studies of the Interior Atmosphere, Magnetosphere and Satellites, pp. 1102-1145, 1976.
- Cassidy, T. A., and R. E. Johnson, Monte Carlo model of sputtering and other ejection processes within a regolith, *Icarus*, 176(2), 499-507, 2005.
- Chamberlain, J. W. & Hunten, D. M., Theory of planetary atmospheres. An introduction to their physics and chemistry., ed. Chamberlain, J. W. & Hunten, D. M., 1987.
- Domingue D. L., Koehn P. L., Killen R. M. , Sprague A. L. ,Sarantos M. , Cheng A. F. ,Bradley E. T. , and McClintock W. E., Mercury's Atmosphere: A Surface Bounded Exosphere. *Space Sci. Reviews*, 131:161-186, August 2007.
- Hapke B., Theory of reflectance and emittance spectroscopy, ed. B. Hapke, 1993.
- Hapke B., Bidirectional reflectance spectroscopy. 6. Effects of porosity, *Icarus*, 195, 918-926, 2008.
- Johnson, R. E., Leblanc, F., Yakshinskiy, B. V., & Madey, T. E. 2002, *Icarus*, 156, 136, 2002.

Imke de Pater and Jack J. Lissauer, Planetary Sciences, ch.4, Planetary Atmospheres, P.65, 2001.

Killen, R.M., Potter, A.E., Fitzsimmons, A., Morgan, T.H., Sodium D2 line profiles: Clues to the temperature structure of Mercury's exosphere. *Planet. Space Sci.* 47, 1449-1458, 1999.

Killen, R.M et al., *Space Sci. Rev.* 132, 433, 2007.

Killen, R.M., Shemansky, D., Mouawad, N., Expected emission from Mercury's exospheric species, and their ultraviolet-visible signatures. *Astrophys. J. Suppl. Ser.* 181, 351-359, 2009.

Lammer, H., P. Wurz, M. R. Patel, R. Killen, C. Kolb, S. Massetti, S. Orsini, and A. Milillo, The variability of Mercury's exosphere by particle and radiation induced surface release processes, *Icarus*, 166(2), 238-247, 2003.

Leblanc, F. & Johnson, R. E., *Icarus*, 164, 261, 2003.

Leblanc, F. et al., Mercury's exosphere origins and relations to its magnetosphere and surface. *Planet. Space Sci.* 55, 1069-1092, 2007.

Leblanc, F., Doressoundiram, A., Schneider, N., Mangano, V., Lopez Ariste, A., Lemen, C., Gelly, B., Barbieri, C., Cremonese, G., High latitude peaks in Mercury's sodium exosphere: Spectral signature using THEMIS solar telescope. *Geophys. Res. Lett.* 35, 18204, 2008.

Lewis, John S. Physics and Chemistry of the Solar System (2nd ed.). Academic Press. p. 463, 2004.

McClintock, W.E., Bradely, E.T., Vervack, R.J., Killen, R.M., Sprague, A.L., Izenberg, N.R., Solomon, S.C., Mercury's exosphere Observations during MESEENGER's first Mercury flyby. *Science* 321, 92-94, 2008.

- McClintock, William E.; Vervack Jr., Ronald J.; Bradley, E. Todd et al. "MESSENGER Observations of Mercury's Exosphere: Detection of Magnesium and Distribution of Constituents". *Science* 324 (5927): 610-613, 2009.
- Munsell Kirk-editor, NASA: Solar System Exploration: Missions to Mercury, November 06, 2006.
- Mouawad, N., M.H. Burger, R.M. Killen, A. E. Potter, W. E. McClintock, R.J. Vervack Jr., E. T. Bradley, M. Benner, S. Naidu, *Icarus*, 211, 21-36, 2011.
- Ness, N. F., K. W. Behannon, R. P. Lepping, Y. C. Whang, and K. H. Schatten (1974), Magnetic-Field Observations near Mercury - Preliminary Results from Mariner-10, *Science*, 185(4146), 151-160, 1974.
- Potter, A.E., Morgan, T.H., Discovery of sodium in the atmosphere of Mercury. *Science* 229, 651-653, 1985.
- Potter, A.E., Morgan,T.H., *Icarus* 67, 336-340, 1986.
- Potter, A.E., Morgan, T.H., Evidence for magnetospheric effects on the sodium atmosphere of Mercury *Science* 248, 835-838, 1990.
- Potter, A. E., Killen, R. M., & Morgan, T. H., Meteoritics and Planetary Science, 37, 1165, 2002.
- Potter, A. E., Killen, R. M., & Sarantos, Spatial distribution of Sodium on Mercury M., *Icarus*, 181, 1, 2006.
- Potter, A. E., Killen, R. M., *Icarus* 194, 1, 2008.
- Richard W. Pogge, Extended Object Spectrophotometry, ASP Conference Series, Vol. 23, 1992.

- Sarantos, M., Reiff, P.H., Hill, T.W., Killen, R.M., Urquhart, A.L. A Bx-interconnected magnetosphere model for Mercury. *Planet. Space Sci.* 49, 1629-1635, 2001.
- Schmidt, C.A., Wilson, J.K., Baumgardner, J., Mendillo, M., Orbital effects on Mercury's escaping sodium exosphere. *Icarus* 207, 9-16, 2010.
- Slavin J. A. et al., *Science* **321**, 85, 2008.
- Smyth, W. H. & Marconi, M. L., *ApJ*, 441, 839, 1995.
- Smyth, W.H., Marconi, M.L., Theoretical overview and modeling of the sodium and potassium atmospheres of Mercury. *Astrophys. J.* 441, 839-864, 1995a.
- Solomon, S. C., et al., The MESSENGER mission to Mercury: Scientific objectives and implementation. *Planetary and Space Science*, 49, Issues 14 and 15, 1445-1465, 2001.
- Sprague, A.L., Mercury's atmospheric sodium bright spots and potassium variation: A possible cause. *J. Geophys. Res.* 97, 18257-18264, 2001.
- Sprague, A.L., Kozlowski, R.W.H., Hunten, D.M., Schneider, N.M., Domingue, D.L., Wells, W.K., Schmitt, W., Fink, U., Distribution and abundance of sodium in Mercury's atmosphere, 1985-1988. *Icarus* 129, 506-527, 1997.
- V. Mangano, C. Barbiera, G. Cremonesoe, F. Leblanc, Observation and Modeling of Mercury's exosphere, *Mem. S.A.It. Suppl.* Vol. 11, 95, 2007.
- Vervack, R.J., McClintock, W.E., Killen, R.M., Sprague, A.L., Anderson, B.J., Burger, M.H., Bradely, E.T., Mouawad, N., Solomon, S.C., Izenberg, N.R., Mercury's Complex Exosphere: Results from MESSENGER's Third Flyby. *Science* 329, 672, 2010.

- Wiens, R.C., Burnett, D.S., Calaway, W.F., Hansen, C.S., Lykkem, K.R., Pellin, M.L., Sputtering products of sodium sulfate: implications for Io's surface and for sodium bearing molecules in the Io torus. *Icarus* 128, 386-397, 1997.
- Yakshinskiy, B. V. & Madey, T. E., Surface Science, 451, 160, 2000.
- Yakshinskiy, B. V. & Madey, T. E., Nature, 400, 642, 1999.
- Zurbuchen, Thomas H.; Raines, Jim M.; Gloeckler, George et al, MESSENGER Observations of the Composition of Mercury's Ionized Exosphere and Plasma Environment. *Science* 321 (5885): 90-92, 2008.

## APPENDIX A

### Array correction

Examining the spatial profiles of the flatfiled mercury images, the sky part to the right of the spectrum should be flat, since the light from the sky should be distributed uniformly along the slit, but it's not the case in our images.

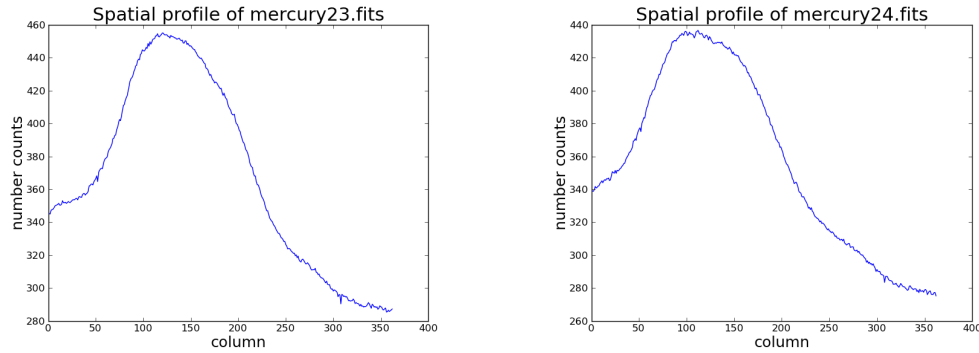


Figure A.1: Spatial profiles of images 23 and 24.

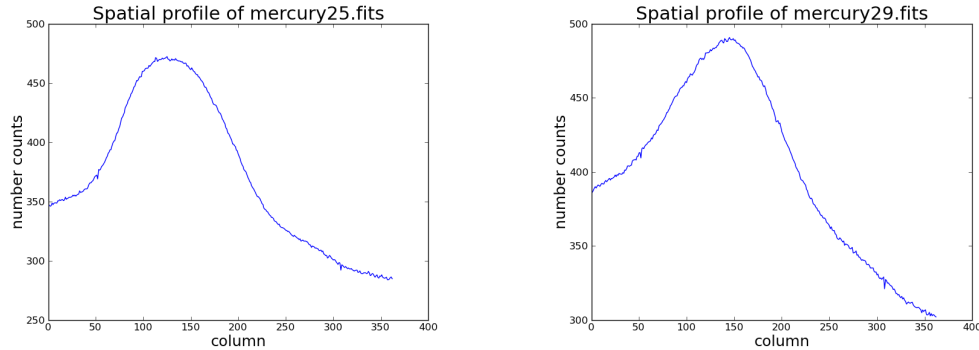


Figure A.2: Spatial profiles of images 25 and 29.

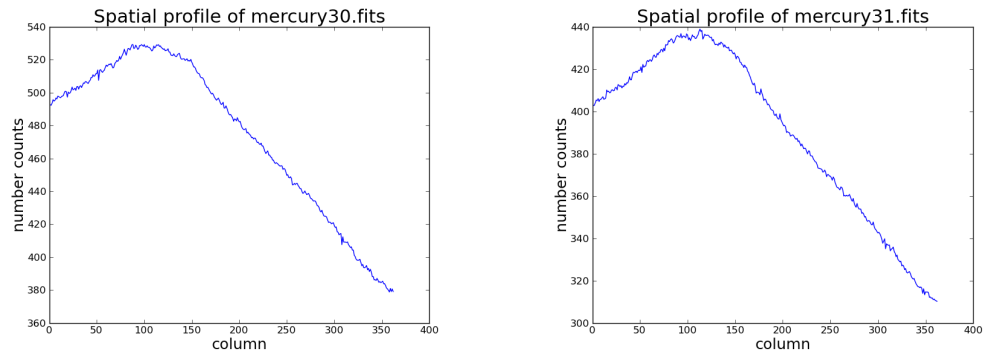


Figure A.3: Spatial profiles of images 30 and 31.

So a correction has to be done to these images in order to flatten the sky, and make it at even counts at both sides of the slit.

Usually the Flatfield corrects for such non-uniform illumination, but it appears that it's not doing a good job with our data so we have to artificially correct for it. What I did is create an array, the flatfielded images will be divided by this array to obtain a flattened sky at the right side of the image, and that is at the same intensity as the sky from the left side of the image. And since the sky level is different from an image to another, each image will have its own correction, and therefore its own array.

I will explain the procedures for one image, the same applies to all the others: We begin first by extracting the spatial profile of the sky part from the right end of the image which has a dimension of  $62 \times 756$ , this is what we obtain:

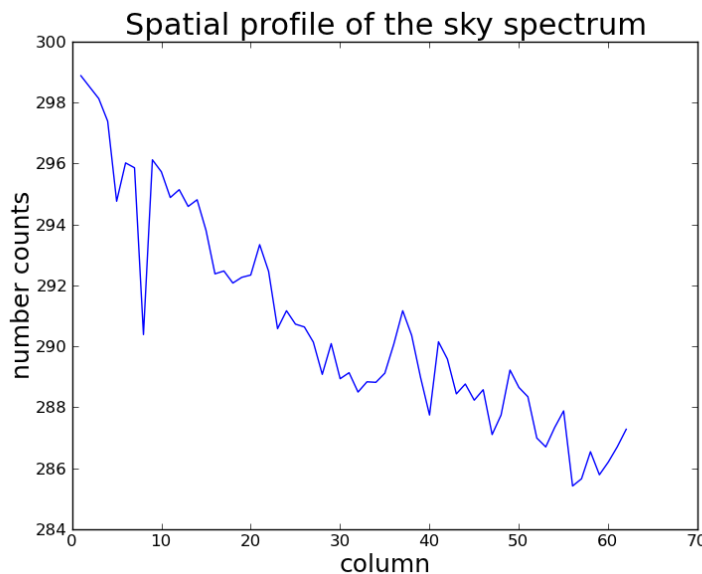


Figure A.4: The gradient in the sky spectrum.

As can be seen, this sky profile shows a gradient that has to be removed; the sky should be flat having the same number counts along the 62 pixels, but which number count should it be leveled to? For this, we have to examine the spatial profile of the corresponding flatfielded image (Figure A.1-left panel), the sky at the left side of the image has an intensity of approximately 350 counts, so the counts along the 62 pixels shown in Figure A.4 should all have a value of 350 counts, we fit the spatial profile of the sky part using the task **sfit** with a *chebychev* function of order 2 , we then use python to read these fitted values and divide them by 350 to obtain the values that should be included in the last 62 pixels of the correction array.

But the rest of the spatial profile has to be altered correspondingly, meaning that an interpolation has to be done from a certain pixel in the spatial profile to the

new flattened sky part. To know this position, we have to examine the normalized Flatfield (since we are fixing the Flatfielding), to see where the slope in its spatial profile begins:

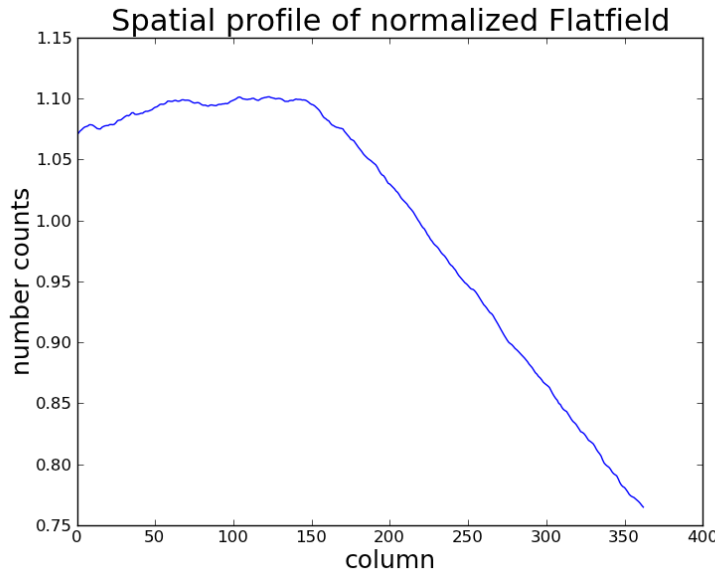


Figure A.5: The spatial profile of the normalized Flatfield.

Examining the spatial profile of the normalized Flatfield, the slope begins at pixel 146.

Using python, we make an array of dimension 362, and made in the following way:

- From pixel 1 to 146, the spatial profile of the mercury image has not to be changed, and therefore the corresponding values are 1.
- From pixel 300 to 362 where the sky region is, the values are those corresponding to the fit divided by 350.

- From pixel 146 (where the slope of the normalized Flatfield begins) to pixel 361 (before the sky region), an spline interpolation is done using the task **proto.interp** in IRAF.

Once this array is generated, we use the task **rrespectext** to convert the textfile containing the array values to an IRAF image, and we divide the flatfielded mercury image with this array, and this is the new spatial profile of the mercury image:

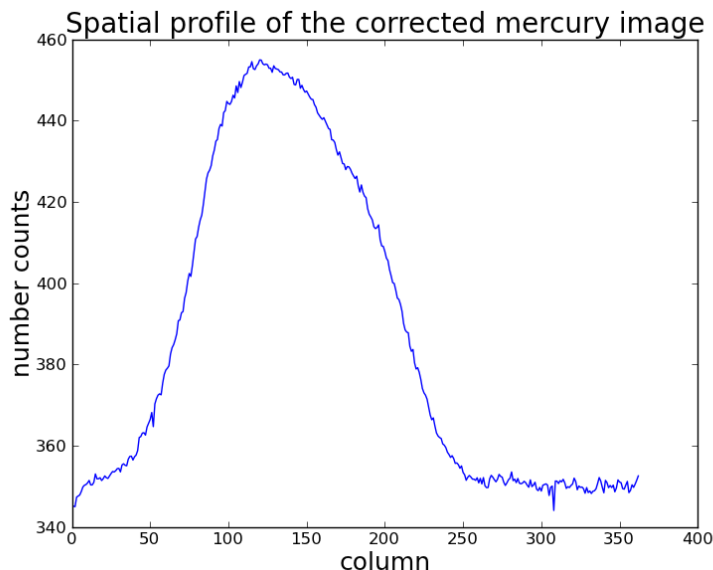


Figure A.6: The spatial profile of mercury23 after correction, the sky is flat and at the same intensity as the left sky.

The same correction procedures apply to the other images, but with difference in the intensity that the sky should be leveled to, here are the spatial profiles of all the images of the data of September 29 before and after the correction:

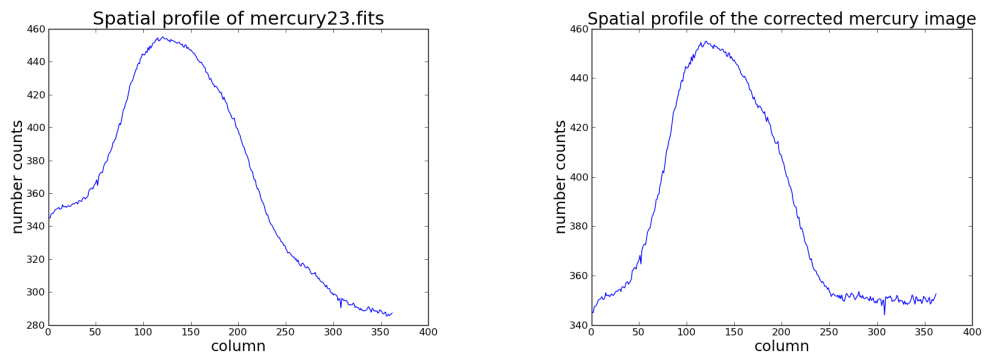


Figure A.7: Image 23 spatial profile before and after correction

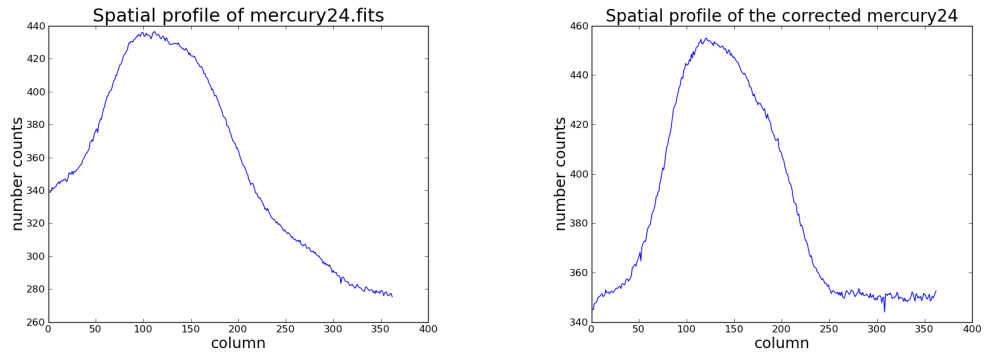


Figure A.8: Image 24 spatial profile before and after correction

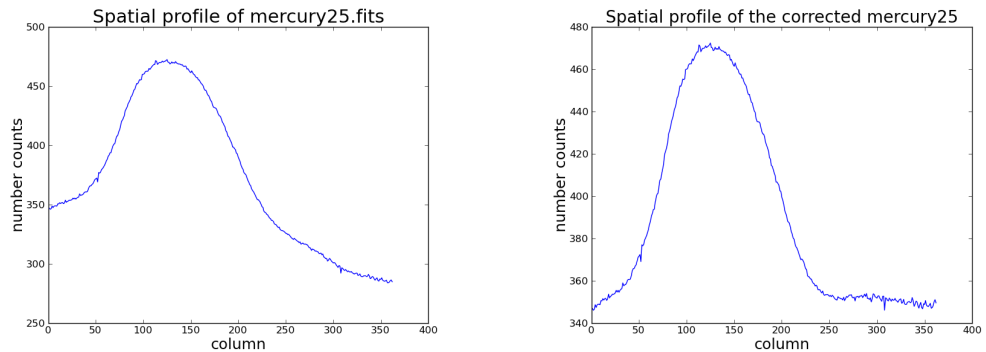


Figure A.9: Image 25 spatial profile before and after correction

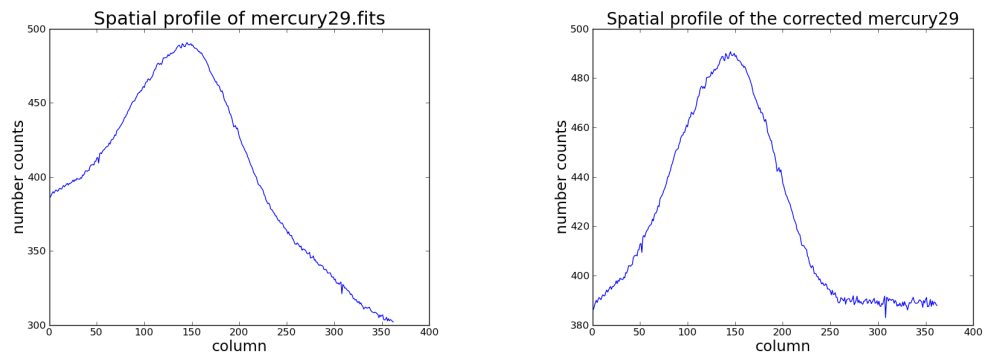


Figure A.10: Image 29 spatial profile before and after correction

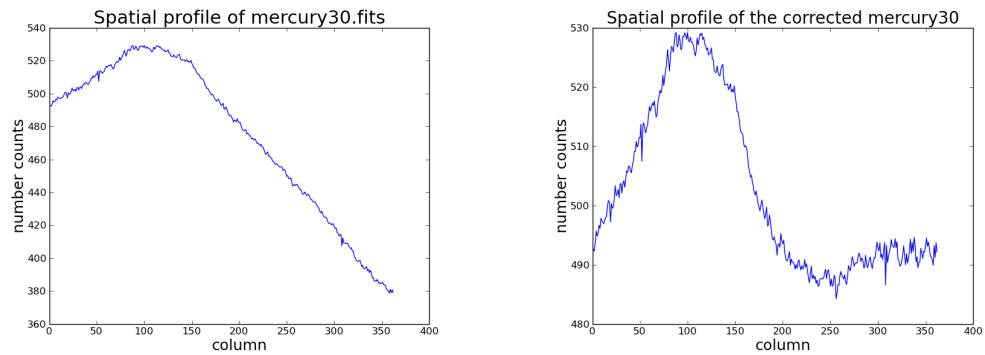


Figure A.11: Image 30 spatial profile before and after correction

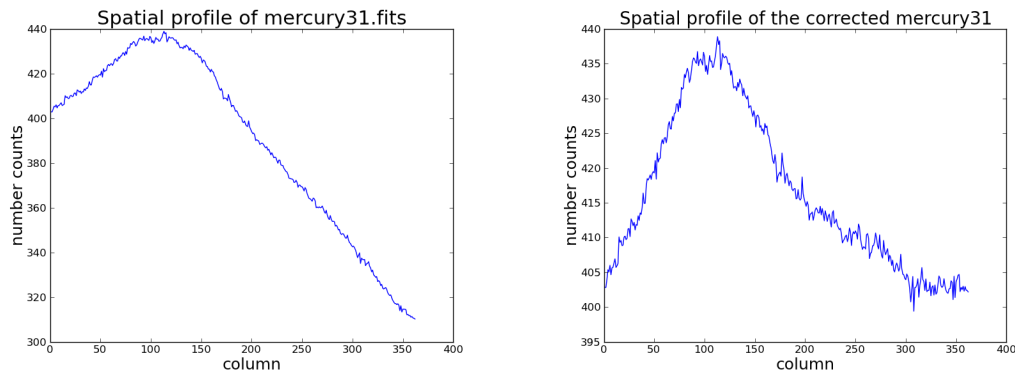


Figure A.12: Image 31 spatial profile before and after correction

## APPENDIX B

### CL scripts

I am presenting in this appendix one of the CL scripts I wrote, `reduction.cl`, to gain an idea of the syntaxe of Iraf CL language.

#### B.1 reduction.cl

This is the first code applied to the raw data in order to make the standard corrections for longslit data images.

---

```
## DECLARING THE LISTS AND VARIABLES

string *list1

string *list2

string *list3

string *list4

string *list5

string *list6

string *list7

string *list8

string *list9

string *list10

string *list11
```

```
string *list12

string *list13

string s4, s5, s6, s7, s8, s9, s10, s11, s12, s13, s14, s15, s16, s17,
      s18, s19, s20, s21, s22, s23, s24, s25, s26, s27

## LOADING THE PACKAGES

noao

imred

ccdred

onedspec

twodspec

longslit

stsdas

## LIST OF DATA IMAGES

sections ("sep*.fits", > "data.lis")

## COORDINATE TRANSFORMATION FOR COLUMN REGISTRATION

geomap ("input1", "data1", 1, 1056, 1, 1024, transforms="", results="",
        fitgeometry="general", function="polynomial", xxorder=2, xyorder=2,
        xxterms="half", yxorder=2, yyorder=2, yxterms="half", maxiter=0,
        reject=3., calctype="real", verbose=yes, interactive=yes,
        graphics="stdgraph", cursor="")

## COORDINATE TRANSFORMATION FOR LINE REGISTRATION
```

```

geomap ("input2", "data2", 1, 1056, 1, 1024, transforms="", results="",
        fitgeometry="general", function="polynomial", xxorder=2, xyorder=2,
        xxterms="half", yxorder=2, yyorder=2, yxterms="half", maxiter=0,
        reject=3., calctype="real", verbose=yes, interactive=yes,
        graphics="stdgraph", cursor="")

## APPLYING COLUMN REGISTRATION

list1 = "data.lis"

while (fscanf(list1,s2) !=EOF){

s3 = "c"//s2

geotran (s2,s3, "data1","input1", geometry="geometric", xin=INDEF,
         yin=INDEF,xshift=INDEF, yshift=INDEF, xout=INDEF, yout=INDEF,
         xmag=INDEF, ymag=INDEF,xrotation=INDEF, yrotation=INDEF, xmin=INDEF,
         xmax=INDEF, ymin=INDEF,ymax=INDEF, xscale=1.,yscale=1., ncols=INDEF,
         nlines=INDEF, xsample=1.,ysample=1., interpolant="linear",
         boundary="nearest",fluxconserve=yes, nxblock=512,
         nyblock=512,verbose=yes)

sections(s3, >> "colregdata.lis")

}

## APPLYING LINE REGISTRATION

list2 = "colregdata.lis"

while (fscanf(list2,s4) !=EOF){

s5 = "r"//substr(s4,2,10)//".fits"

```

```

geotran (s4,s5, "data2","input2", geometry="geometric", xin=INDEF,
yin=INDEF,xshift=INDEF, yshift=INDEF, xout=INDEF, yout=INDEF,
xmag=INDEF, ymag=INDEF,xrotation=INDEF, yrotation=INDEF, xmin=INDEF,
xmax=INDEF, ymin=INDEF,ymax=INDEF, xscale=1.,yscale=1., ncols=INDEF,
nlines=INDEF, xsample=1.,ysample=1., interpolant="linear",
boundary="nearest",fluxconserve=yes, nxblock=512, nyblock=512,
verbose=yes)

sections(s5, >> "regdata.lis")

}

## TRIMMING THE DATA IMAGES

list = "regdata.lis"

while (fscanf(list, s1) !=EOF){

imcopy(s1//"[346:707,96:851]",s1,verbose=yes)

}

## MASTER ZERO

zerocombine ("@zero.lis", output="Zero.fits", combine="average",
reject="avsigclip", ccdtype=" ", process=no,delete=no, clobber=no,
scale="none", statsec="", nlow=0, nhigh=1, nkeep=1,mclip=yes,
lsigma=3., hsigma=3., rdnoise="0.", gain="1.", snoise="0.",
pclip=-0.5, blank=0.)

## SUBTRACTING MASTER ZERO FROM MERCURY IMAGES

list4 = "mercury.lis"

```

```

while (fscanf(list4,s9) !=EOF){

    s10 = "mercnozero"//substr(s9,9,10)//".fits"

    imarith (s9, "-", "Zero.fits",s10, title="", divzero=0., hparams="",
              pixtype="", calctype="",verbose=no, noact=no)

    sections (s10, >> "mercurynozero.lis")

}

## SUBTRACTING MASTER ZERO FROM THE FLATS

list5 = "flat.lis"

while (fscanf(list5,s11) !=EOF){

    s12 = "flatnozero"//substr(s11,9,10)//".fits"

    imarith (s11,"-", "Zero.fits", s12, title="", divzero=0., hparams="",
              pixtype="", calctype="",
              verbose=no, noact=no)

    sections (s12, >> "flatnozero.lis")

}

## COSMIC RAY REMOVAL FOR MERCURY IMAGES

list3 = "mercurynozero.lis"

while (fscanf(list3,s6) !=EOF){

    s7= "mercurycr"//substr(s6,11,12)//".fits"

    s8= "mask"//substr(s6,11,12)//".fits"

    lacos_spec (s6, s7, s8, gain=2., readn=6., xorder=9, yorder=3,
                sigclip=4.5, sigfrac=0.5, objlim=1., niter=4, verbose=yes)
}

```

```

sections (s7, >> "mercurycr.lis")

}

## COSMIC RAY REMOVAL FOR FLAT IMAGES

list12 ="flatnozero.lis"

while (fscanf(list12,s24) !=EOF){

s25= "flatcr"//substr(s24,11,12)//".fits"

s26= "mask"//substr(s24,11,12)//".fits"

lacos_spec (s24, s25, s26, gain=2., readn=6., xorder=9, yorder=3,
            sigclip=4.5, sigfrac=0.5, objlim=1., niter=4, verbose=yes)

sections (s25, >> "flatcr.lis")

}

## MASTER FLAT

flatcombine ("@flatcr.lis", output="Flat.fits", combine="median",
            reject="avsigclip", ccdtype=" ", process=no,
            subsets=yes, delete=no, clobber=no, scale="exposure", statsec="", nlow=1,
            nhigh=1, nkeep=1, mclip=yes, lsigma=3., hsigma=3., rdnoise="0.",
            gain="1.", snoise="0.", pclip=-0.5, blank=1.)

##NORMALIZATION OF THE MASTER FLAT

imstat ("Flat.fits", fields="mean", lower=INDEF, upper=INDEF, nclip=0,
        lsigma=3., usigma=3., binwidth=0.1, format=no, cache=no, > "mean.dat")

```

```

imarith ("Flat.fits", "/", "@mean.dat", "Flatnorm.fits", title="",
        divzero=0., hparams="", pixtype="", calctype="",
        verbose=yes, noact=no)

## FLAT-FIELDING THE IMAGES

list6 = "mercurycr.lis"

while (fscanf(list6,s13) !=EOF){

    s14 = "mercury"//substr(s13,10,11)//".fits"

    imarith (s13,"/", "Flatnorm.fits", s14, title="", divzero=0., hparams="",
              pixtype="", calctype="", verbose=no, noact=no)

    sections (s14, >> "finalmercury.lis")

}

## TRIMMING THE SKY PART

list7 = "finalmercury.lis"

while (fscanf(list7, s15) !=EOF) {

    s16 = "sky"//substr(s15,8,9)//".fits"

    imcopy(s15//"[301:362,*]", s16, verbose=yes)

    sections (s16, option="fullname", >> "skylist.lis")

}

## SKY TEMPLATES

list8 = "skylist.lis"

while (fscanf(list8, s17) !=EOF) {

    s18 = "skyavg"//substr(s17,4,5)//".fits"

```

```
s24 = "skyrep">//substr(s17,4,5)//".fits"

blkavg (s17,s18, 62, 1, 1, 1, 1, 1, 1)
blkrep (s18,s24, 362, 1, 1, 1, 1, 1, 1)

sections (s24, option="fullname", >> "SKYlist.lis")

}

## SKY SUBTRACTION

list10 = "finalmercury.lis"

list11 = "SKYlist.lis"

while (fscanf (list10, s21) !=EOF && fscanf(list11, s22) !=EOF ) {

s23 = "mercurynosky">//substr(s21,8,9)//".fits"

imarith (s21,"-", s22, s23, verbose=yes)

sections (s23, option="fullname", >> "mercurynosky.lis")

}
```

---